Université du Québec
Institut National de la Recherche Scientifique
Centre Éneregie, Matériaux et Telécommunications

# INVESTIGATION OF PULSATILE RETINAL DEFORMATION AS NEW BIOMECHANICAL DESCRIPTOR OF THE HUMAN OCULAR DYNAMICS FOR GLAUCOMA PROGNOSIS

Par

**Maribel Hidalgo-Aguirre, M.Sc.**

Thèse présentée pour l'obtention du grade de
*Philosophae Doctor*, PhD.
en Sciences de l'Énergie et des Matériaux

Jury d'évaluation

| | |
|---|---|
| Président du jury et examinateur interne | Tiago H. Falk, PhD.<br>INRS-ÉMT |
| Examinatrice externe | Farida Cheriet, PhD.<br>Polytechnique Montréal |
| Examinateur externe | Younes Agoumi, MD.<br>Centre Hospitalier de l'U. de M. |
| Directeur de recherche | Santiago Costantino, PhD.<br>Université de Montréal |
| Co-directeur de recherche | Mark R. Lesk, MD, M.Sc.<br>Université de Montréal |
| Co-directeur de recherche | Tsuneyuki Ozaki, PhD<br>INRS-ÉMT |

*A mi roca fuerte, mi faro en la oscuridad.*
*Gracias por estar . . .*

# Acknowledgments

This is the culmination of a long and painful chapter of my life with its good share of happiness and rewards, a journey that has left me important lessons, good new friends, picnics in sunny days, dear old friends, walks in snowy nights, nursing trips, melancholic twilight hours, stormy days, wonderful memories and lots of scientific knowledge. During such years so many people have helped me to grow not only as scientist but also as a person and here is my tribute to them.

First of all I need to express my gratitude to my former supervisor, Dr. E. Martí, for encouraging me to pursue the PhD abroad and expand my horizons, for believing in me, for his support and invaluable teachings through all these years, for being the best mentor ever, for his great passion that has inspired me every day.

I have to express my gratitude to my supervisor, Dr. Santiago Costantino, for accepting me in his group, offering me a new beginning and the opportunity to expand my knowledge of physics to a new area, for his patience, advice and money; to the guys in the group for their friendship, support, constructive critics and beer fridays, for teaching me about neutrophils, lapap, clap and all the other stuff that I don't remember anymore.

My sincere thanks to Dr. Ozaki, my co-supervisor, for his kindness, help and support during moments of trouble and despair, for giving me a second chance.

I would like to thank my co-supervisor Mark R. Lesk for sharing his expertise, for the explanations and fruitful discussions, for his valuable guidance and support. Thanks to Denise Descovich for her friendship, for taking the time to answer my many questions about ophthalmology, teaching me how to read the charts and helping me to gather all the information I

needed for this research. I also have to thank Julian Gitelman and Diane Sayah for helping me with the patient handling and the standard eye exams.

I am specially thankful to Gargi and Sze-Phing, for welcoming me at INRS and offering me their friendship and support since the first day and also during difficult times. To my friends at INRS: Yavuz, Gaston and Sami, Ivan, Belete, Shun, Marta, Maria and Bruno, Hassan, Esen, Manoj, thank you for the good memories, for the picnics, excursions and parties, for sharing your culture and friendship. I also have to thank the other friends I made in Montreal, Paola, Lucy, Erika, Angélica, Patrisia C., Joannie, Patricia M. and Javier, for all the good moments we spend together, for opening me their houses and their hearts, for all the laughter, the traveling, the parties, the beers and coffees.

I am very grateful to my besties in México, Argelia, Cristina, Job, Dulce, Tania and Milton, for all their good vibes and wishes, for listening, for their unconditional support, their friendship, advise and love, for being by my side all the way trough this journey, sometimes difficult sometimes joyful. I love you guys!

I specially need to express my gratitude to my parents, Carmen and José Manuel, for teaching me the importance of helping others and the value of hard work, for always encouraging my curiosity and my hunger for knowledge, for their support since the very beginning of this adventure that started in 2002 when I felt the calling, for understand or perhaps just accept my great passion for physics, for letting me spread my wings even when they knew it would take me far away from home.

Finally, I am very grateful to the Consejo Nacional de Ciencia y Tecnología de México (CONACyT) for the scholarship granted for the realization of this PhD, without it, this dream would not be possible. I also want to acknowledge support for this research from the Natural Sciences and Engineering Research Council of Canada, the Canadian Institutes of Health Research, Fonds de Recherche en Ophtalmologie de l'Uniersité de Montréal, the Glaucoma Research Society of Canada and the Pfizer Canada Unrestricted Grant.

# Abstract

Glaucoma is the second leading cause of blindness worldwide. The facts that glaucoma does not present any symptoms until major visual loss has occurred and that the primary causes of this neuropathy remain unknown make it challenging for both, diagnosis and treatment. While elevated intraocular pressure (IOP) remains the primary risk factor, other parameters such as low ocular perfusion pressure, ocular blood flow and the elasticity of the sclera and lamina cribrosa have been identified in the last years as additional factors potentially influencing the risk, prevalence and progression of the glaucomatous neuropathy.

Theoretically, an individual's susceptibility to IOP is in part determined by the eye geometry and tissue anatomy, therefore, it seems natural to consider biomechanics as framework for explaining how IOP-related stress and strain influence the physiology and pathophysiology of the connective, neural and vascular tissue, causing the changes on the structural and functional integrity of the optic nerve observed in glaucoma. The key challenge is then to understand how ocular biomechanics, in combination with the aforementioned risk factors, are transduced into tissue damage.

It has been demonstrated that glaucoma is directly related with blood flow deficiencies in the retinal and choroidal circulation. The choroid has the highest blood flow per gram tissue of any organ in the human body and this flow is 80 % pulsatile. This pulsatility has been hypothesized to drive the retina forward while expanding the sclera, leading to a pulsatile deformation of the axons traveling from the retina and through the lamina cribrosa to the brain. If we consider that the mechanical properties of the tissues are also altered during the progression of the disease, then is very likely that such deformation may change.

Within this framework, the present work is centered on the study and characterization of the peripapillary retinal tissue deformation due to choroidal vascular pulsatility and its possible implication in axonal damage and loss of the retinal nerve fiber layer in glaucoma. The general strategy designed to perform such investigation is to use video rate optical coherence tomography images of the optic nerve head combined with fully automated image analysis algorithms specially developed to measure and determine retinal deformation. A cross-sectional study was then carried out at the ophthalmology clinic of the Maisonneuve-Rosemont Hospital to evaluate peripapillary retinal deformation on patients that cover the most representative part of the glaucoma spectrum.

The obtained results show that healthy eyes have significantly larger deformation of the peripapillary retina compared with the glaucoma spectrum. The measured deformation correlates differently with the principal risk factors of the glaucomatous neuropathy depending on diagnosis. Reduced retinal displacement proved to be related to glaucoma progression predictors showing that the biomechanical properties of the eye are altered even when there is no evident changes in the optic nerve head structure.

Due to the versatility of the segmentation algorithm, it was possible to carry out a preliminary study to investigate retinal deformation around the macula using images previously acquired from a different clinic study. In this case, perifoveal retinal deformation in healthy eyes resulted to be significantly larger than in early glaucoma. Furthermore, ocular rigidity as well as changes in ocular volume were correlated with perifoveal retinal displacement in healthy eyes, which confirms that the observed deformation is driven by choroidal pulsatility.

All these results suggest that the amount of retinal deformation should be further investigated since it could be potentially used as a new biomechanical descriptor of the eye for early diagnosis and assessment of glaucoma progression.

**Keywords**: Optic Nerve Head; Glaucoma; Image Processing; Optical Coherence Tomography; Ocular Biomechanics; Ocular Dynamics; Retinal Deformation.

# Highlights

- Software was developed to segment the inner limiting membrane (ILM) in low quality OCT images of the optic nerve head of both, normal and diseased eyes. The accuracy of the ILM delineation is comparable to that of the specialists.
- An analysis algorithm was developed in order to measure the deformation of the peripapillary retina using the ILM profiles segmented from a series of OCT images acquired at video rate.
- Using such method we showed that there is inner retinal deformation (in time) and that retinal deformation measurements are highly reproducible (ICC 0.86).
- Four groups of patients at different stages of open-angle glaucoma were studied with the purpose to investigate the role of retinal deformation in the glaucomatous damage.
- Neuro-Peripapillary (N-PP) retinal deformation was larger in healthy eyes compared to glaucomatous diseased eyes in the inferotemporal region.
- N-PP deformation was correlated with central corneal thickness, ocular pulse amplitude and diastolic perfusion pressure in more than one study group.
- Eyes with a larger vertical cup to disc ratio, thinner peripapillary retinal nerve fiber layer, and larger visual field mean defect, three indicators of glaucoma severity, showed smaller N-PP deformation.

- ◇ Multiple regression analysis showed that the variables that better predicted the magnitude of the inferotemporal N-PP deformation in eyes with early glaucoma are the intraocular pressure (IOP) and the systolic perfusion pressure (SPP). The model suggests that an increase in IOP as well as low SPP, two major risk factors in glaucoma, contribute to reducing the deformation.

- ◇ Due to the versatility of the segmentation and analysis algorithms developed, it was possible to investigate deformation in the macular region, finding larger perifoveal deformation in healthy eyes compared with early glaucoma eyes.

- ◇ More elastic healthy eyes showed larger perifoveal deformation, which confirms that the amount of deformation experienced by the retinal ganglion cells depends on the biomechanical properties of the tissue.

- ◇ The obtained results suggest that the observed retinal deformation might be beneficial to axonal tissue, and its diminishment, part of the glaucoma pathophysiology.

- ◇ Retinal deformation has the potential to be used as new biomechanical descriptor of the eye.

# Contents

# List of Figures

# List of Tables

# Chapter 1

# Introduction

Glaucoma is a very complex disease characterized by the loss of the peripheral vision. It is the second leading cause of blindness worldwide, affecting more than 400,000 Canadians, with 20,000 more estimated to become blind by this disease by 2031 [1]. Furthermore, approximately 50% of the people that are affected by the disease have not being diagnosed.

Thanks to advances in imaging technologies, physicians have come to rely on such imaging devices to differentiate healthy patients from those with glaucoma depending on characteristic changes visible at the optic nerve head associated with typical glaucomatous patterns of visual loss. Imaging of the optic nerve head (ONH) has shown that the volume of the optic cup increases with intraocular pressure (IOP), and that these changes can sometimes be partially reversed by reducing IOP [2]. However, as glaucoma does not present any symptoms until major visual loss has occurred, it becomes challenging for both, diagnosis and treatment. Moreover, to predict how fast the disease will progress is still an impossible task, nullifying the possibility to distinguish rapidly degenerating glaucoma patients from those with a more benign course and thus, limiting the options or strength of treatment.

Among these new technologies, optical coherence tomography (OCT) is a powerful noninvasive imaging technique that has become a standard clinical and research tool in ophthalmology, providing a direct and accurate visualization of the retina and its layered structure [3]. This information helps to detect and monitor a variety of retinal diseases such as age-related macular degeneration, diabetic retinopathy, and retinal detachments. OCT shows particular promise in detecting glaucoma, where an accurate characterization of the changes at the optic nerve head as well as the peripapillary retinal nerve fiber layer is of central importance for the management of the disease.

Using this technique it has been recently demonstrated that tissue around the ONH is deformed during cardiac pulsations [4], and that such movement is different in healthy and glaucoma patients [5]. However, since the vast majority of research projects based on OCT rely on static images made up of several averaged frames, these findings underline the relevance of comprehensive dynamic studies for which the development of novel imaging strategies is required.

An essential part of OCT data processing is segmentation, and one of its most challenging problems is the design of a system that works properly in clinical applications, i.e., the development of robust methods capable of dealing with pathological cases, where the structure of the retina can change drastically. Several methods have been proposed to segment the vitreal-retinal boundary on macular OCT images [6]-[8]; however, those models cannot simply be applied to the ONH region owing to the significant anatomical differences. Nerve head geometries vary considerably across patient population, and appearance variation is also introduced by the angle of the scan. This could be the reason why, to date, very little has been reported on the automatic analysis of 2-D ONH images.

Nowadays, volumeric scanning centered at the ONH is becoming more common, however, the segmentation method employed in this cases is based on a three-

dimensional graph search approach that makes use of regional consecutive B-scans, and the algorithm is trained on the planimetry from color stereo photos to determine the rim and cup regions that can be then colocalized on the fundus image, and finally translated to the OCT scan [9],[10]. More recently, a study performed with a software developed for retinal analysis of Straus OCT macular images with computer-aided grading methodology, OCTRIMA [11]-[13], has included the measurement of the cup to disc ratio as complementary information extracted from the central image of a volumetric scan [14]. Notwithstanding such advances, currently there are no commercial OCT devices that allow image sequences of volumetric scans acquired and saved at the velocity needed to perform dynamic studies.

Although 2-D ONH segmentation is part of the analysis software of commercial OCT devices, such type of software is not fit to be integrated in analysis pipelines; their source code is not available and they are not compatible across the different OCT companies and products. It also has to be considered that the study of dynamic processes requires the segmentation of large sets of low quality images, a non trivial task that has not been accomplished before. Consequently, systematic measurements of ONH tissue dynamics cannot be carried out with commercial software tools, which are mostly aimed at clinical settings, nor with the segmentation methods available to the research community, emphasizing the need of new image analysis methods that would help understand retinal diseases such as glaucoma.

## 1.1 Thesis Structure

This doctoral thesis is organized as follows: Chapter 2 reviews the anatomy and physiology of the human eye along with the process of vision. The definition of the visual field (VF) and its measurement using standard automated static perimetry, the gold standard for VF testing, are also included. Such measurement is crucial in the management of ocular diseases such as Glaucoma, a retinal pathology explained in Section 2.3 and, in which, this doctoral research is centered. The chapter finalizes with an overview of ocular biomechanics and its implication in the development of glaucoma, underlining the importance of dynamic studies to characterize the mechanical response of ocular tissues like the optic nerve.

To investigate the biomechanics of the ocular fundus noninvasively, optical coherence tomography was the imaging technique selected due to its high resolution, accuracy and image acquisition velocity. Chapter 3 offers a description of the technique, its theoretical framework, basic principles and main characteristics. This chapter also contains a depiction of our home-made double scanning OCT prototype, a device designed to scan simultaneously the retina and the cornea, and developed in an attempt to determine ocular rigidity.

The hypothesis of this doctoral thesis that proposes retinal deformation as a cause of glaucoma is introduced in Chapter 4, along with the research objectives. Then, the modality of the clinical study performed in order to characterize retinal deformation, the description of the four groups of patients tested, as well as the ethical considerations, are presented. The full methodology followed during the ophthalmic examination, the equipment used and the parameters under investigation, including the OCT imaging protocol, are also detailed in this chapter.

Chapter 5 explains, step by step, the fully automated image analysis algorithm, specially developed to measure retinal deformation from video rate OCT images of

the optic nerve. Tests of the accuracy of the segmentation and the reproducibility of the analysis method, are shown too. Once validated, the method was used to characterize the neuro-peripapillary retinal deformation in three groups at different stages of the glaucomatous neuropathy and a healthy group. The results obtained, not only comparing the deformation among groups but also investigating the relationship between the proposed deformation and the other ocular, vascular and demographic parameters included in the analysis, are shown and discussed in Chapter 6. Taking advantage of the versatility of the image analysis algorithm, a preliminary study to investigate retinal deformation around the macula in healthy subjects and glaucoma patients was also performed, including ocular rigidity values as an extra parameter in the analysis. This clinical study and the obtained results are contained in Chapter 7.

The conclusions derived from this doctoral research, on retinal deformation as a new biomechanical descriptor of the ocular dynamics, are presented in Chapter 8. Appendix A enlists the published articles and conference presentations related to the present work. Finally, Appendixes B and C contain the french versions of the abstract and a synthesis of the thesis, respectively.

# Chapter 2

# Physiology and Pathophysiology of the Human Eye

Before entering in a more detailed description of glaucoma or how to measure ocular tissue dynamics it is necessary to understand the anatomy of the eye and the process of vision [15]-[18].

## 2.1 Anatomy of the Eye

The optical structure of the eye is among the most sophisticated of the specialized non-neural sensory endings. More than half of the sensory receptors in the human body are located in the eyes, and a large part of the cerebral cortex is devoted to processing visual information.

The adult eyeball measures about $2.5cm$ in diameter. Of its total surface area, only the anterior one-sixth is exposed, the rest is recessed and protected by the orbit.

Anatomically, the wall of the eyeball consists of three layers: fibrous tunic, vascular tunic and retina (Fig. 2.1).

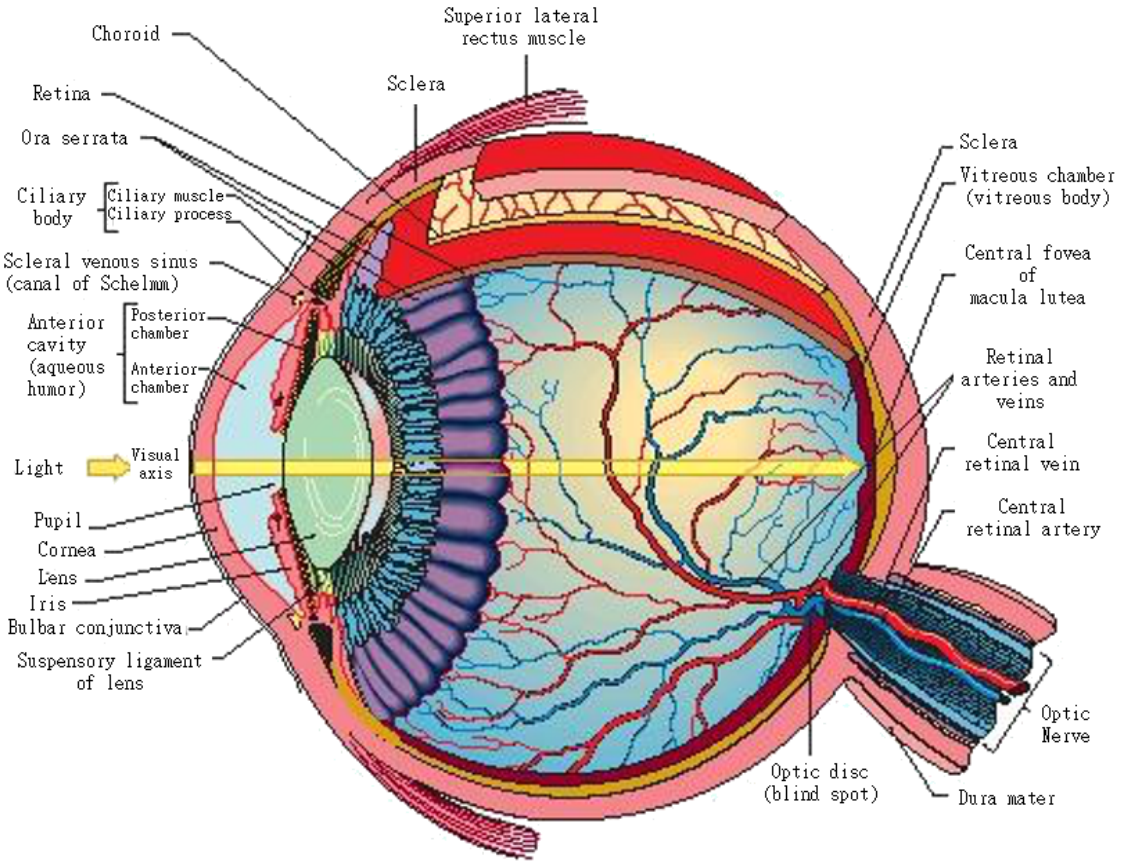


**Figure 2.1 – Transversal section of the human eye. (http://www.edoctoronline.com/medical-atlas)**

### 2.1.1 Fibrous Tunic

It is the superficial layer of the eyeball and consists of the anterior cornea and posterior sclera. The **cornea** is a thin transporting epithelialized structure that is devoid of blood vessels and has a cell structure that is specialized to maintain its high transparency. Its curved surface, with a radius of curvature of $7.8mm$ in a typical human cornea, helps focus light onto the retina. Their middle coat consists of collagen

fibers and fibroblasts. The inner coat consists of descemet's membrane and the corneal endothelium. The cornea has an index of refraction $n_c \approx 1.376$. The **sclera** is a layer of dense connective tissue made up mostly of collagen fibers and fibroblasts. It is a tough flexible shell that gives shape to the eyeball and serves as a site of attachment for the extrinsic eye muscles. At the junction of the sclera and cornea is an opening known as the scleral venous sinus or **canal of Schlemm**.

### 2.1.2 Vascular Tunic

The vascular tunic or uvea is the middle layer of the eyeball. It is composed of three parts: choroid, ciliary body and iris. The **choroid** is a highly vascularized layer that lines most of the internal surface of the sclera. Its numerous blood vessels provide nutrients to the posterior surface of the retina. It is richly pigmented with melanin that absorbs stray light rays, which prevents reflection and scattering of light within the eyeball.

In the anterior portion of the vascular tunic, the choroid becomes the **ciliary body**, that consists of ciliary processes and ciliary muscle. The ciliary processes are protrusions or folds on the internal surface of the ciliary body. They contain blood capillaries that secrete aqueous humor. Extending from the ciliary processes we find the **zonular fibers**, suspensory ligaments that attach to the lens. The fibers consist of thin, hollow fibrils that resemble elastic connective tissue fibers. The ciliary muscle is a circular band of smooth muscle. Contraction or relaxation of the ciliary muscle changes tightness of the zonular fibers, which alters the shape of the lens, adapting it for near or far vision.

Immersed in the aqueous humor is a diaphragm known as the **iris**, which is the colored structure visible through the window of the cornea. The iris, shaped like a flattened donut, is suspended between the cornea and the lens and is attached at its

outer margin to the ciliary processes. It consists of melanocytes and circular and radial smooth muscle fibers. The principal function of the iris is to regulate the amount of light entering the eyeball through the **pupil**, the hole in the center of the iris. Autonomic reflexes regulate the pupil diameter in response to light levels. When bright light stimulates the eye, parasympathetic fibers of the oculomotor nerve stimulate the circular muscles or sphincter pupillae of the iris to contract causing a decrease in the size of the pupil. In dim light, sympathetic neurons stimulate the radial muscles or dilator pupillae of the iris to contract, causing an increase in the pupil's size (Fig. 2.2). The iris can expand or contract the pupil over a range from about $2mm$ in bright light to roughly $8mm$ in darkness. In addition to this function, it is also linked to the focusing response and will contract to increase image sharpness when doing close work.

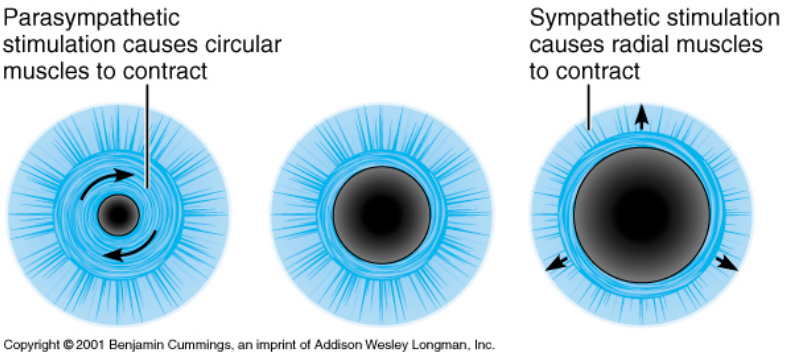


**Figure 2.2 – Anterior view of the pupil illustrating the response of the circular and radial muscles of the iris to autonomic nervous system stimulation.**

### 2.1.3 Retina

The third and inner layer of the eyeball, the **retina**, lines the posterior three-quarters of the eye and covers much of the inner surface of the choroid. The retina is the beginning of the visual pathway; it is, histologically and embriologically, a part of the central nervous system. Not only does it transduce light into neural signals, but it also does some remarkably complex processing of visual information before passing it

onto other regions of the brain. The surface of the retina is the only place in the body where blood vessels can be viewed directly and examined for pathological changes.

The retina, which is $\approx 200\mu m$ thick, consists of a pigmented layer and a neural layer. The **pigmented layer** is a sheet of melanin-containing epithelial cells located between the choroid and the neural part of the retina. The melanin in the pigmented layer, as in the choroid, helps to absorb stray light rays. The **neural layer** of the retina is a multilayered outgrowth of the brain that processes visual data extensively before sending nerve impulses into axons that form the optic nerve. The distinct layers of retinal neurons, the photoreceptor layer, the bipolar cell layer and the ganglion cell layer, are separated by two zones, the outer and inner synaptic layers, where synaptic contacts are made. Light passes through the ganglion and bipolar cell layers and both synaptic layers before it reaches the photoreceptor layer (Fig. 2.3).

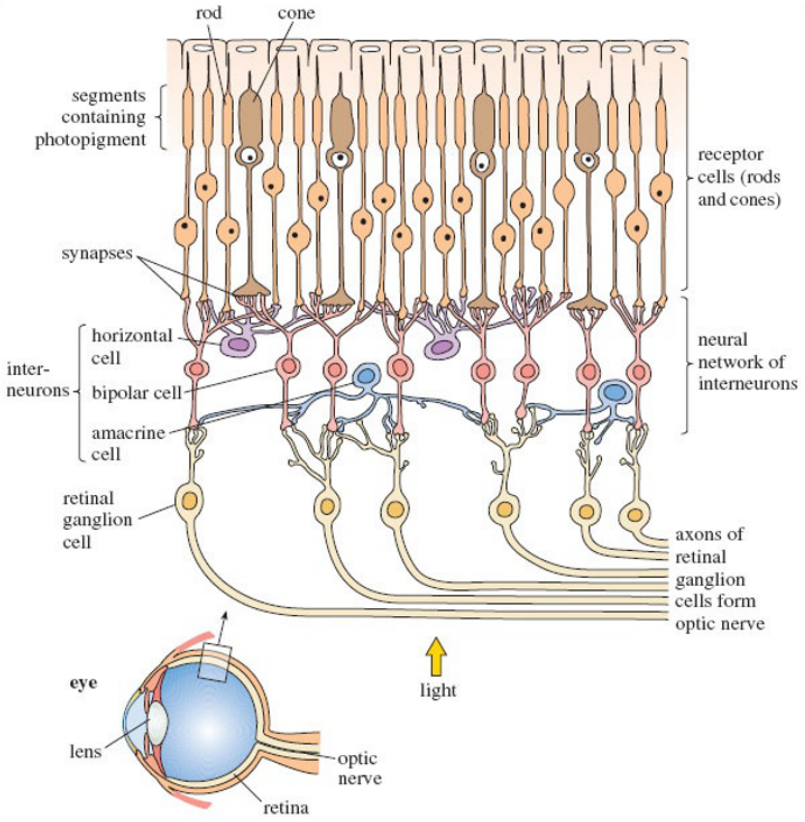


**Figure 2.3 – Microscopic structure of the retina.(https://ib−bioplans.wikispaces.com)**

**Photoreceptors** are specialized cells that begin the process by which light rays are ultimately converted to nerve impulses. The human eye contains two kinds of photoreceptor cells: rods and cones. Each retina has about 6 million cones and 120 million rods intermingled nonuniformly over most of the retina. The human retina has only one type of rod of about $2\mu m$ in diameter, which is responsible for the monochromatic dark-adapted vision, and three sub-types of cones: blue, green and red, each of about $6\mu m$ in diameter. Each kind of cone expresses a photopigment with a different absorption spectrum which peaks fall at about 420, 534 and $564nm$, corresponding to the violet, yellow-green and yellow-red regions of the spectrum (Fig. 2.4). Cones are responsible for the color-sensitive vision experienced in brighter environments.

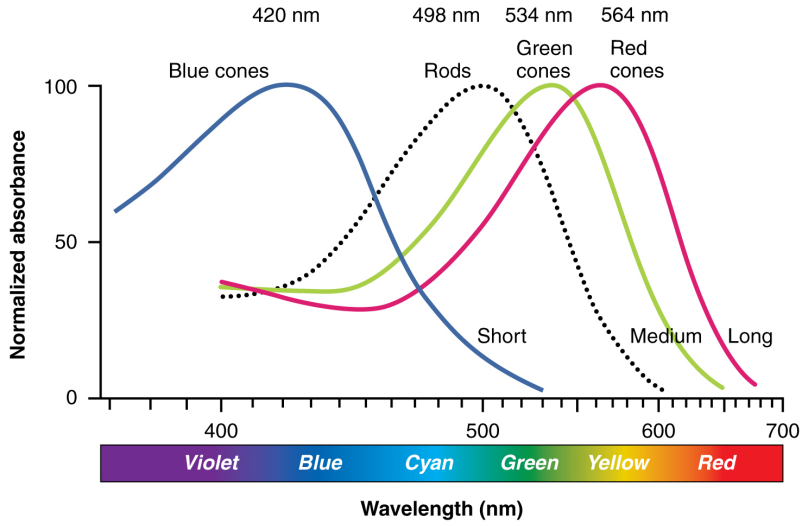


**Figure 2.4 – Color peak sensitivity and absorbance spectra of the photopigments of cones and rods. (http://cnx.org/contents/YPmMIA42@1/Vision)**

From photoreceptors, information flows through the outer synaptic layer to bipolar cells and then through the inner synaptic layer to ganglion cells in a mainly radial direction. The **bipolar cell layer** has two other interneurons called horizontal cells and amacrine cells. These cells form laterally directed neural circuits that modify the signals being transmited along the pathway from photoreceptors to ganglion cells. The **ganglion cell layer** generates the sole output of the retina, its axons extend

posteriorly to the **optic disc** and pass through a three dimensional meshwork covered by astrocytes, capillaries and connective tissue known as the **lamina cribrosa** exiting the eyeball via the **optic nerve** to the thalamus. The optic disc is also called the blind spot because it contains no rods or cones. Bundled together with the optic nerve are the central retinal artery, a branch of the ophthalmic artery, and the central retinal vein (Fig. 2.5). Branches of the central retinal artery fan out to nourish the anterior surface of the retina and the central retinal vein drains blood from the retina through the optic disc.

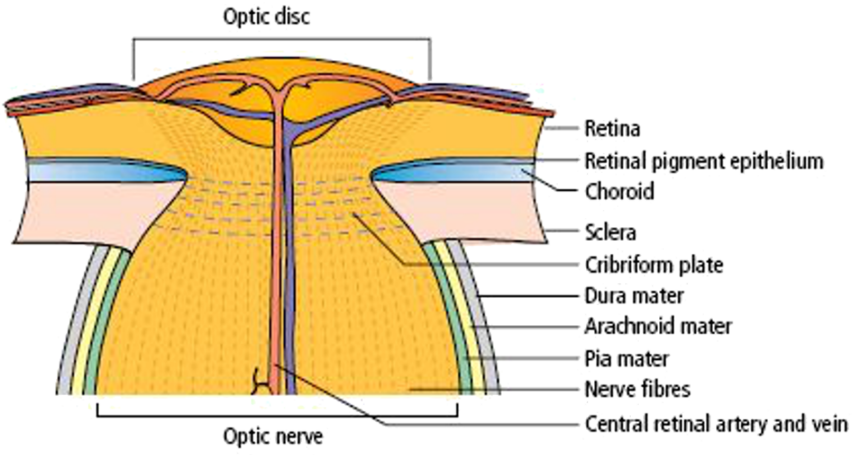


**Figure 2.5 – Structure of the optic nerve. (http://wiley-vch.e-bookshelf.de/)**

In the exact center of the posterior portion of the retina is a small depression from 2.5 to $3mm$ in diameter known as the yellow spot or **macula lutea**. It is composed of more than twice as many cones as rods. At the center of the macula there is a rod-free region of about $300\mu m$ in diameter called the **fovea centralis**. Here the cones are thinner, with diameters of 3 to $1.5\mu m$, and more densely packed than anywhere else in the retina. Several adaptations of the fovea allow it to mediate the highest visual acuity in the retina. The layers of bipolar and ganglion cells do not cover the cones here, they are displaced laterally to the side of the fovea to minimize light scattering on the way to the receptors. In addition, within the fovea the ratio of photoreceptors to ganglion cells falls dramatically. Most of foveal receptors synapse on only one

bipolar cell, which in turn synapses on only one ganglion cell. Therefore, as each ganglion cell is devoted to a very small portion of the visual field, the central vision has high resolution. At the periphery, the ratio of receptors to ganglion cells is high thus, each ganglion cell has a large receptive field which reduces the spacial resolution but increases its sensitivity, being the areas specialized in movement detection and responsible to locate objects in the visual field.

The actual perception of a scene is constructed by the eye-brain system in a continuous analysis of the time-varying retinal image.

### 2.1.4 Lens

Behind the pupil and the iris is the **lens**. It has both, the size and shape of a small bean ($9mm$ in diameter and $4mm$ thick) and is a complex layered fibrous mass surrounded by an elastic membrane (Fig. 2.6a), producing a nonhomogeneous refractive index that is larger in the center than in the periphery. The lens is an onion-like structure formed of roughly 22,000 closely packed columnar cells arranged in concentric shells and enclosed by a thin, tough, transparent capsule composed of epithelial cells (Fig. 2.6b). The cells of the lens have a high concentration of proteins called $\alpha$-crystallins, which help increase its density and enhance its focusing power. The index of refraction of the lens ranges from about 1.406 at the inner core to approximately 1.386 at the less dense cortex, representing a gradient-index system. It is held in position by encircling zonular fibers which attach to ciliary processes. It provides the needed fine-focusing mechanism through changes in its shape.

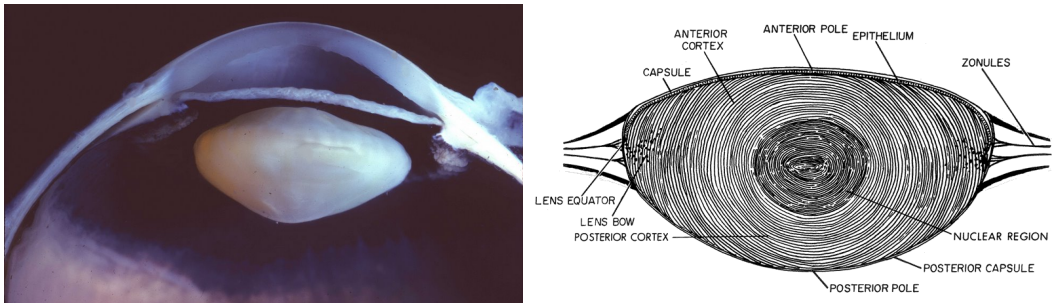


(a) (b)

**Figure 2.6 – Lens: a) Lateral view; b) Diagram of its internal structure. (http://www.missionforvision.org; http://www.oculist.net/).**

### 2.1.5 Interior of the Eyeball

The lens divides the interior of the eyeball into two cavities: the anterior cavity and the vitreous chamber. The **anterior cavity**, the space anterior to the lens, consists of two chambers. The **anterior chamber** lies between the cornea and the iris. The **posterior chamber** lies behind the iris and in front of the zonular fibers and lens. Both chambers are filled with **aqueous humor**, a protein-free ultrafiltrate of blood plasma ($n_{ah} \approx 1.336$). It nourishes the lens and cornea and keeps the anterior chamber slightly pressurized, which helps maintain the eye's shape.

Aqueous humor continually filters out of blood capillaries in the ciliary processes and enters the posterior chamber. It then flows forward between the iris and the lens, through the pupil, and into the anterior chamber. From the anterior chamber, aqueous humor drains through the trabecular meshwork into the scleral venous sinus and then into the blood (Fig. 2.7). Normally, aqueous humor is completely replaced about every 90 min.

The **vitreous chamber**, which is the larger posterior cavity of the eyeball, lies between the lens and the retina and it is filled with a transparent gelatinous substance known as the **vitreous humor** ($n_{vh} = 1.337$) that holds the retina flush against the choroid, giving the retina an even surface for the reception of clear images. It occupies

about four-fifths of the eyeball, it is formed during embryonic life and consists of mostly water plus collagen fibers and hyaluronic acid. Unlike the aqueous humor, the vitreous humor does not undergo constant replacement. It contains microscopic particles of cellular debris floating freely as well as phagocytic cells to remove them, keeping this part of the eye clear for unobstructed vision.

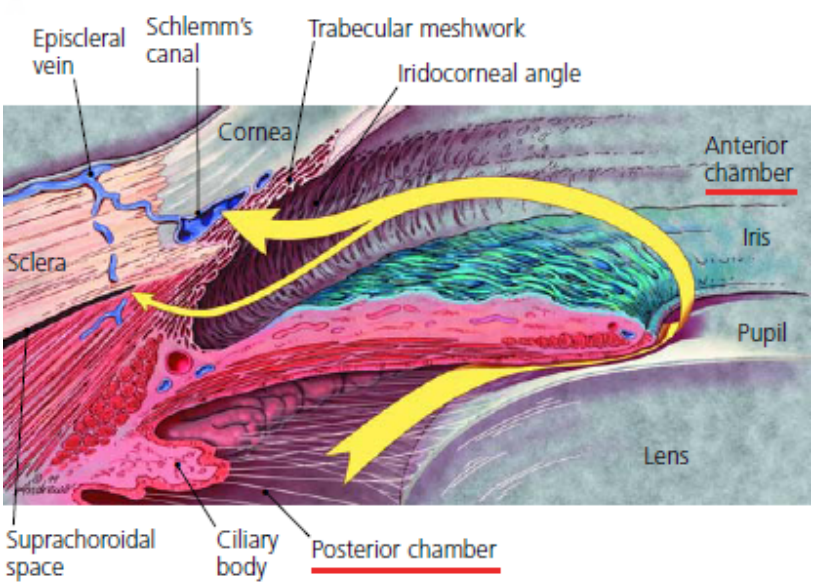


**Figure 2.7 – The iris separates the anterior and posterior chambers of the eye. Yellow arrows indicate the aqueous humor pathways: most aqueous flow is through the trabecular meshwork (large arrow), the rest, through the uveoscleral routes (small arrow) [19].**

The pressure in the eye or **intraocular pressure** ($\approx 21 mmHg$) is produced mainly by the aqueous humor and partially by the vitreous humor. It maintains the shape of the eyeball and prevents it from collapsing.

### 2.1.6 Focusing

As light rays enter the eye, they are refracted at the anterior and posterior surfaces of the cornea. Both surfaces of the lens further refract the light rays so they come

into exact focus on the retina. About 75% of the total refraction of light occurs at the cornea, the lens provides the remaining 25% of the focusing power.

The fine focusing or **accommodation** is a function performed by the lens. Ordinarily, the ciliary muscle is relaxed and the lens is in a fairly flat configuration because it is stretched in all directions by taut zonular fibers, increasing its radii, which in turn increases its focal length. In this configuration, the light from an object at infinity will be focused on the retina. As the object moves closer to the eye, the ciliary muscle contracts, pulling the ciliary process and the choroid forward toward the lens. This action releases tension on the lens and zonular fibers and the lens surfaces take on a smaller radii (Fig. 2.8). The **near point of vision** is the minimum distance from the eye that an object can be clearly focused with maximum accommodation. In a normal eye this distance is about $10cm$ for a young adult.

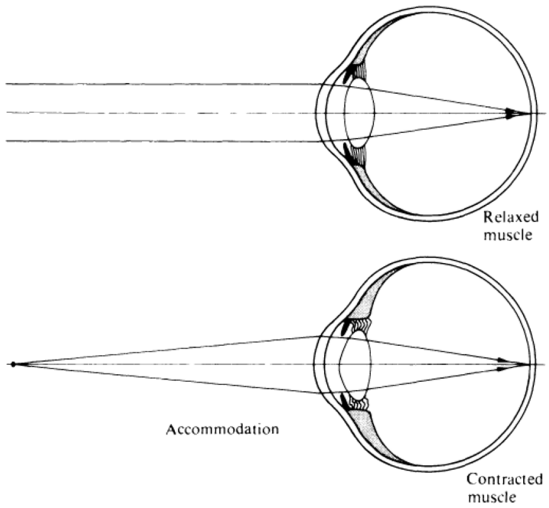


**Figure 2.8 – Accommodation: changes in the lens configuration [17].**

The circular muscle fibers of the iris also have a role in the formation of clear retinal images. The constriction of the pupil occurs simultaneously with accommodation and prevents light rays from entering the eye through the periphery of the lens. Light rays

entering at the periphery would not be brought to focus on the retina and would result in blurred vision.

Several factors are responsible for the degradation of retinal images: diffraction of light in the pupil, optical aberrations and intraocular scattering. Diffraction, which consist on the spreading of the light after passing through the pupil, blurs the images and its effect in the eye is visually significant only when the pupil diameter is less than $2mm$.

Optical aberrations are classified as chromatic and monochromatic. Chromatic aberrations arise from the dependence of refractive index on wavelength, i.e., objects of different colors are imaged onto the retina at different locations. There are two types of chromatic effects in the retinal image: longitudinal chromatic aberration, which refers to the variation of power with wavelength, and transverse chromatic aberration, corresponding to the shift of the image position in the retina for different wavelengths, usually assumed to arise from the off-axis position of the fovea and from natural pupil misalignments. Since the eye is a waterlike sphere, both types of chromatic aberration have significant presence and limit the retinal image quality of white light scenes.

The ocular media acts as a band-pass filter that reduces the range of wavelengths reaching the retina. In general, transmitted wavelengths are well matched to photoreceptor sensitivity, although some of them are too long to be detected. The cornea and the vitreous humor have transmission bandwidths that exceeded the visible spectrum but the lens absorbs light in the short wavelength (blue) part of the visible spectrum. Such blue light absorption mitigates chromatic aberration and strongly increases with age.

Monochromatic aberations in the eye depend on many factors and conditions such as pupil size, age, accommodation, retinal eccentricity and possible corneal or lenti-

cular pathologies. As in any optical system, ocular aberrations increase for large pupil diameters, for example, aberrations for an eye with a pupil diameter of approximately $5mm$ have a magnitude equivalent to less than 0.25 diopters of defocus.

Under normal conditions, aberrations do not impose a limit to vision, with defocus and astigmatism being the main sources of degradation in retinal images. Small amounts of defocus ($\pm$0.25D) or natural astigmatism ($<$ 0.5D) have relative small impact on visual acuity.

Finally, intraocular light scattering originates from localized irregularities of the refractive index within the ocular media and leads to the spread of light at large angles over the retina. It is usually described by the angular distribution of light intensity in the image plane. In general, scattered light reduces retinal image quality owing to a decrease in the contrast of the images, e.g., in scenes containing a bright light source such as those found in night driving.

## 2.2 Field of Vision

Vision is the act of perceiving a combination of particular features such as vernier displacement [1], the movement of an object, the change in luminous intensity, also known as flickering, the contrast or difference in luminous intensity from one object to another, the ability to identify colors, etc [20]. Visual acuity is the capacity to discriminate the fine details of objects.

The visual field (VF) corresponds to the topographic arrangement of photoreceptors in the eye. The peripheral limits of the VF are revealed by the locations at which the strongest test object stimuli are first visible, and are determined by the anatomic locations of relevant structures such as the orbital location of the globe, the

[1]Distance needed between two stimuli for both to be detected as separate stimuli.

configuration of the upper eyelid, the size of the nose, the position of the retinal ora serrata, etc. In general, a normal visual field extends approximately 100º temporally, 60º nasally, 60º superiorly and 70º inferiorly, as shown in Figure 2.9. A physiologic scotoma or blind spot exists at 15º temporally where the optic nerve leaves the eye. The average blind spot is 7.5º in diameter, vertically centered 1.5º below the horizontal [21]. Age exerts a diminishing effect on visual field sensitivity, starting with a small decline in the early decades of life that accelerates with advancing age, particularly from the seventh decade of life, affecting principally the periphery and superior hemifield [22].

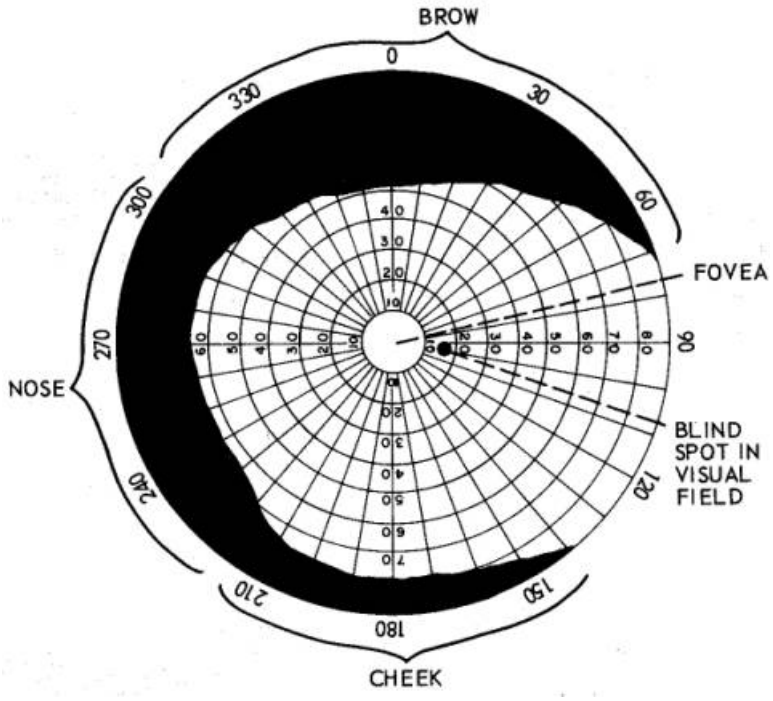


**Figure 2.9 – Parametric chart that shows the average monocular visual field for a right eye with the head and eyes motionless. The nasal field is located to the left of the chart and the temporal to the right. The blind spot is located at 15º temporally, 1.5º below the horizontal. (https://vision.arc.nasa.gov)**

Visual field tests are used to identify scotomas that depending on their size an shape provide information about the presence of a disease in the eye, optic nerve or visual structures in the brain.

### 2.2.1 VF Testing

The systematic measurement of the visual field function is called perimetry, a technique that consists in measuring the sensitivity of the visual system to stimuli presented, varying in size and intensity, at multiple locations of the VF. There are different types of perimetry that examine the sensitivity across the VF with spatial, temporal and chromatic variations, using for example, contrast sensitivity, flicker, motion and color stimuli [23]. The standard unit of measurement in the visual field is the *differential light sensitivity*, defined as the threshold of perception of a test object, relative to its background.

The current gold standard for visual field testing is automated perimetry, developed in the 1970's, which has the capability of detecting very subtle defects and the advantage of comparing the patient's sensitivity to normative data, i.e., to the mean visual threshold in normal people, in a given age group, at a given location in the visual field.

Standard automated static perimetry measures differential light sensitivity, which is vital for glaucoma diagnosis and management. Here, stationary stimuli are presented in an evenly illuminated bowl and the quantification of VF loss is performed using threshold tests to determine the weakest stimulus that can be seen at each location. Whether the stimulus is seen determines whether the next presentation shown at that location should be weaker or stronger. The pattern most frequently used tests a grid of points separated $6^{o}$ from each other, vertically and horizontally, covering the central-most region within a radius of $24^{o}$ to $30^{o}$ from the point of fixation. The size of the stimuli may also be varied, from Goldman size I, a white spot of $0.25mm^2$, up to Goldman size V corresponding to a $64mm^2$ spot. Usually, visual status is estimated by standard automated perimetry with a size III stimulus ($4mm^2$) to permit

visibility determinations at diseased areas. Larger sizes have to be used when visual acuity of the patient is below 20/200 [20],[23].

The Humphrey Visual Field Analyzer (HFA) is the device most widely used in clinical practice. Here, the stimulus is projected on an hemisphere with a $33cm$ radius; background luminance [2] is fixed at $31.5asb$, while stimulus luminance can be varied over a 5.1 log unit range, this is from 0.08 to 10,000$asb$ (50-0$dB$). Test locations unable to see a stimulus of 10,000$asb$ are assumed to be totally blind. All stimuli are presented statistically in random order using a $200ms$ exposure time [24].

The HFA uses the Swedish Interactive Threshold Algorithm (SITA) [25], a forecasting procedure based on Bayesian statistics, where models of normal and glaucomatous visual fields are constructed before the actual test, providing two prior likelihood functions for each test point. The test starts by measuring threshold values in four primary points, one in each quadrant of the field at $12.7^{o}$ from the point of fixation. Stimulus intensities are altered in staircase procedures. These four thresholds are then used to calculate starting levels, i.e., the first stimulus intensities to be used at adjacent test points. If the measured threshold at a point differs by more than 0.4 log unit from the expected value the threshold is measured again. This process is repeated in new points as the test goes on. Thus, this visual field models are repeatedly updated and modified during testing based on patient responses and also after the test, when all gathered information is available. Finally, test results are displayed presenting the threshold estimates as well as the corresponding statistical analysis, including reliability indices such as fixation losses, false positives and false negatives.

Sensitivity results across the VF are displayed in different representations as can be seen in Figure 2.10. First we have a numerical map of the threshold estimates in decibels at the locations tested ($B$), where higher numbers indicate more sensitive

[2] Luminance is a physical quantity that expresses the amount of light emitted or reflected from a surface in a particular direction. In perimetry it is measured in *apostilb* ($asb$), with $1asb = 0.3183candela/m^2$.

vision. Next to it, is the corresponding gray-scale map, where areas with depressed vision are represented with a darker tone. Comparison with the normative data base is shown in the subsequent maps. Subtraction at each location of the mean normal values from the threshold estimates of the patient are numerically displayed in the Total Deviation map ($C$). Positive values represent areas where the patient can see dimmer stimuli than the average individual of that age. Statistical significance of the total deviation at each location is shown in the probability plots, with symbols that indicate the percentile ranking of the deviation within the range of values among healthy age-matched persons.

In the Pattern Deviation plots ($D$), a correction term is applied to the total deviation values which removes a uniform alteration in VF thresholds that might result, for example, if a person has overall higher or lower visual sensation than the norm. This with the purpose of highlight areas in which field loss is more prominent. This plot is very useful to distinguish the effects of cataract from glaucomatous damage.

Global indices that summarize the information from the total deviation and pattern deviation plots are also calculated to help determine change over time ($F$). The **mean deviation (MD)** indicates the net magnitude of the abnormality of the visual field, the more affected the lower the MD value. The **pattern standard deviation or PSD** represents the homogeneity of any abnormality, i.e., is a depiction of focal defects. It is small if all locations deviate from normal by the same amount, a minimal value represents the expected variation caused simply to variability of testing. Mathematically, these two values are the weighted mean and standard deviation of all the total deviation values. The **visual field index (VFI)** is an indicator of the rate of progression and expresses the VF status as a percent of a normal age-adjusted visual field. Greater weight is given to points closer to fixation to adjust for ganglion cell density and visual function. Its values range from 100% (normal) to 0% which corresponds to perimetrically blind.

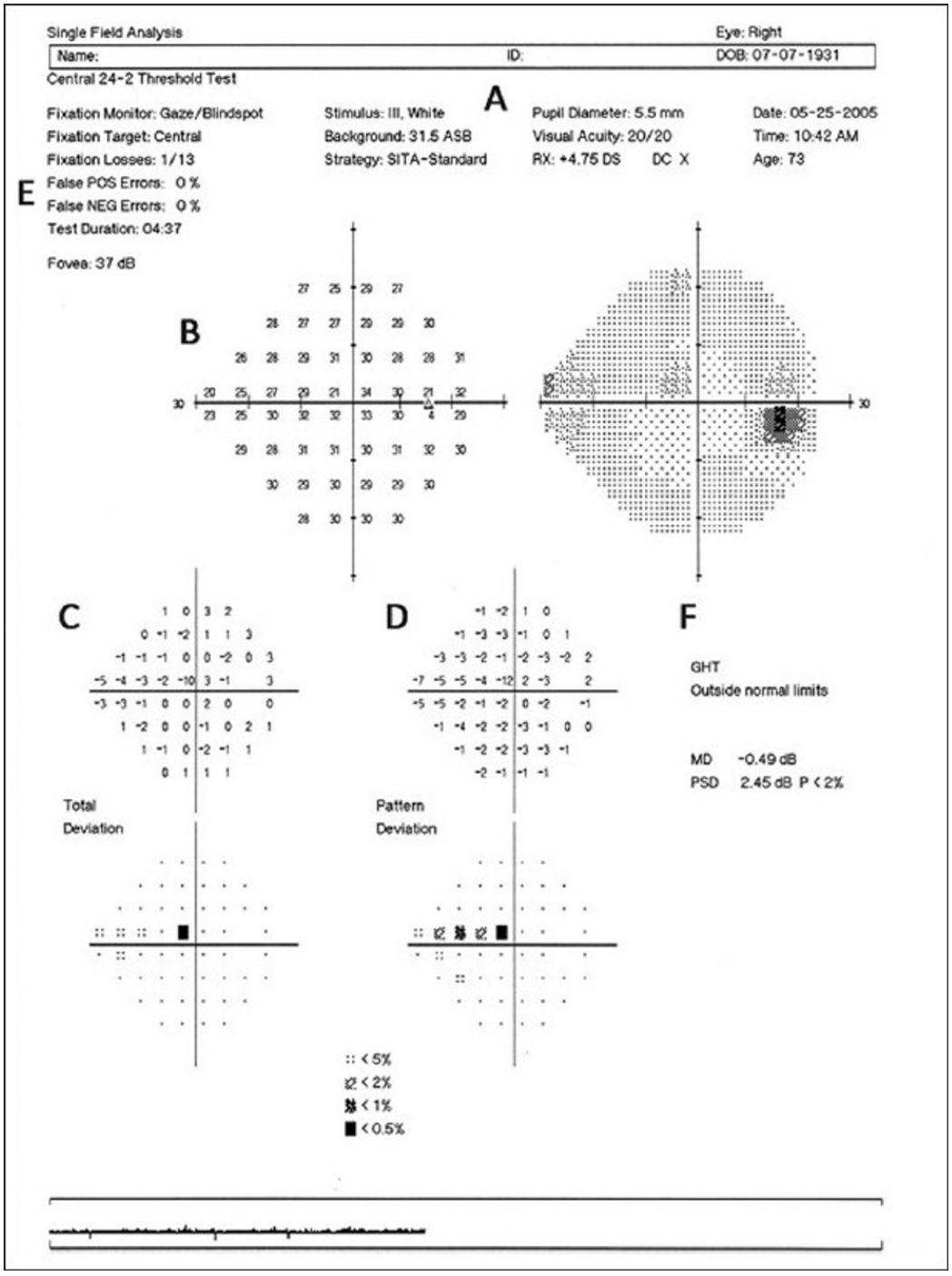


**Figure 2.10 – Print out from a HFA using 24-2 SITA standard test of a right eye. A) Patient ID, stimulus used and test algorithm. B) Numerical display of the threshold values and its corresponding gray scale map. C) Total deviation values and corresponding probability plot. D) Pattern deviation values and probability plot. E) Reliability indices. F) Glaucoma hemifield test (GHT) and global indices.[27].**

The VFI also provides an estimate of additional visual field loss for up to 5 years, considering that the same rate of progression is maintained. Since glaucoma produce localized loss in particular characteristic locations, a statistical calculation called **glaucoma hemifield test (GHT)** is included, a test that compares groups of corresponding points above and below the horizontal meridian to asses for significant differences that may be consistent with glaucoma. Depending on the presence of asymmetry across the midline, it is reported as normal, borderline or abnormal [20],[26],[27].

Interpretation of the visual field is key in ophthalmic and neurologic examinations, where a field defect reveals almost any disease process occurring in the region and also helps locating the site of lesion, e.g., VF defects produced by retinal disease are the result of damage to the retinal neurons themselves and/or the axons of the retinal ganglion cells at the level of the optic nerve head. Visual field coordinates are the opposite of retinal coordinates; therefore, a patient with injury to the ganglion cells in the temporal retina would be predicted to have a nasal visual field defect as can be seen in Fig. 2.11.

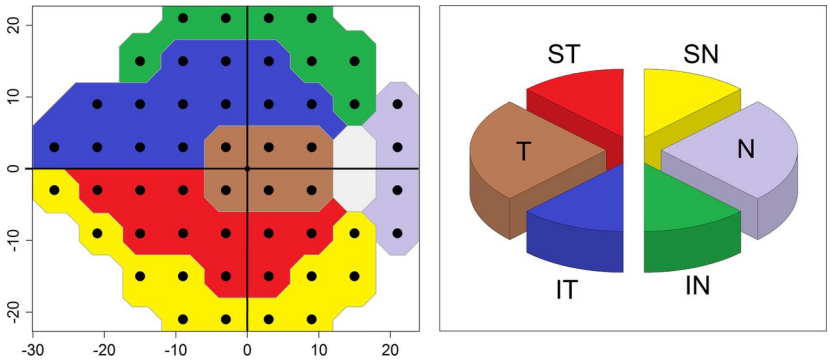


**Figure 2.11 – Structure-function map developed by Garway-Heath, et al. [28], that describes the relationship between the visual field test points in the Humphrey 24-2 test pattern (left) and the ONH anatomy (right). T - temporal region, ST - superotemporal, SN - superonasal, N - nasal, IN - inferonasal, IT - inferotemporal.**

The eye is a very complex system and each one of their components, when affected, can lead to different pathologies. Among them, retinal diseases attract special attention since their effects are directly related with irreversible vision loss and, if not treated, complete blindness. The second leading cause of visual impairment worldwide, principally among the elderly population, is Glaucoma, an asymptomatic disease in its early stages that remain challenging for early diagnosis, having a big impact in the health economics of all countries.

## 2.3 Glaucoma

Glaucoma is a multifactorial optic neuropathy consisting of an heterogeneous group of disorders that usually affects both eyes and combines an abnormal appearance of the optic disc with slowly progressive loss of visual sensitivity. In primary open-angle glaucoma (OAG), the most prevalent form of glaucoma, the angle between the cornea and the iris remains open, as in a healthy eye, but in some cases there is a slow outflow of aqueous humor through the trabecular meshwork which causes a chronic increase in IOP (Fig. 2.12).

OAG is recognized as a progressive disease characterized by the loss of the neuroretinal ganglion cells, kinking the axons that carry visual information from the retina to the brain and consequently, causing changes on the structural and functional integrity of the optic nerve head and the lamina cribrosa (LC).

In many eyes, the axons do not completely fill the optic disc, leaving a physiologic depression in its center called the cup. As nerve fibers die in glaucoma patients, the outer rim of disc tissue becomes thinner, causing the cup to enlarge. The ratio of the diameter of the cup to the diameter of the whole disc is used to assess the volume of rim tissue [29].

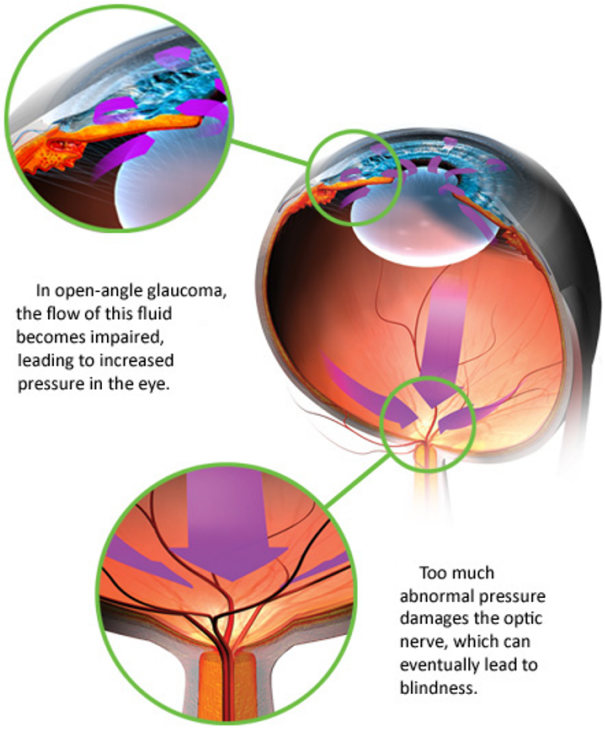


**Figure 2.12 – In most cases of open-angle glaucoma accumulation of fluid in the eye increases IOP which in turn causes damage to blood vessels and optic nerve. (modified from https://www.neomedix.net)**

The normal cup to disc ratio (C/D) is about 0.3 [30] whereas in advanced glaucoma it can reach values close to 1 [31]. Excavation of the disc results from the collapsing together of the successive connective-tissue plates of the lamina cribrosa and their rotation at the point of insertion into the sclera (Fig. 2.13).

In normal eyes, the neuroretinal rim has a characteristic shape: it is wider at the inferior disc region, followed by the superior and the nasal regions. It is more narrow in the temporal disc sector [30]. In glaucoma, this characteristic rim shape is continuously changing with the progressively decreasing rim area. The pattern of neuroretinal rim loss begins most commonly in the inferotemporal disc region and then progresses to the superotemporal, temporal horizontal, inferonasal and finally the superonasal sector. This would convert the normal rim configuration into a rim being even in width at all points, changing the shape of the optic cup from horizontally

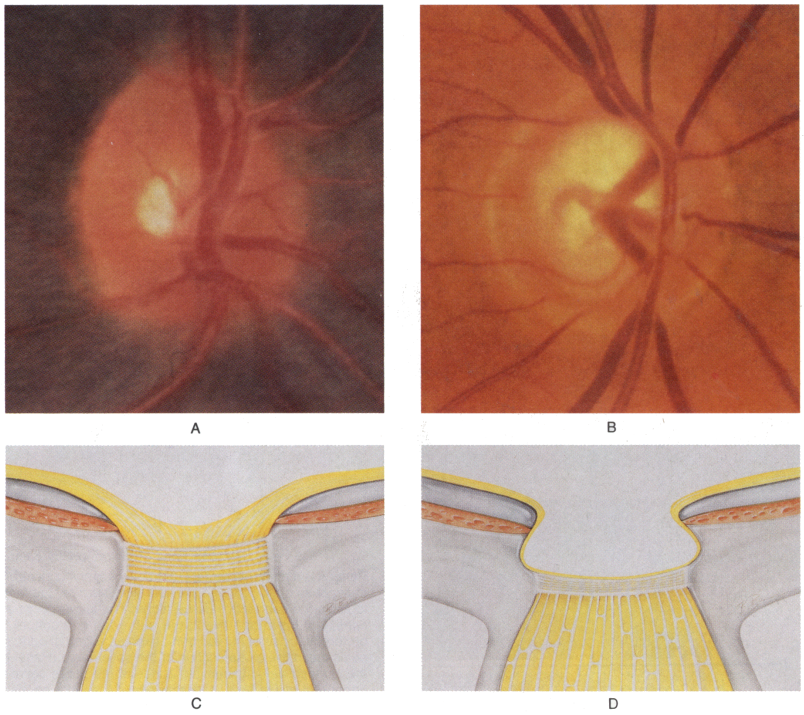


**Figure 2.13 – Normal and glaucomatous optic discs. A) Normal disc with small cup to disc ratio, indicated by the tiny pale central area. B) Glaucomatous optic disc with a large cup excavation, indicated by the sharp and undetermined edge of the cup. C) and D) are schematic diagrams of the features of normal and glaucomatous discs, respectively. The internal structure of the lamina cribrosa is compressed and rotates backward on its insertion into the sclera in patients with glaucoma. [29].**

oval form to a circular form [32]. The corresponding visual field loss starts in the nasal region and progresses as a circular scotoma to full hemifield loss and, ultimately, to total blindness (Fig. 2.14).

Despite all the progress that has been achieved in the understanding of the disease, early glaucoma diagnosis is still challenging since it does not present any symptomatology until major visual loss has occur. However, it has been possible to identify a set of specific features that increase the propensity of an individual to develop OAG. Along with elevated IOP [33], which remains as the primary risk factor, it has been found that older age, ethnicity (African, Asian or Hispanic descent) [34], [35] and family history of glaucoma [36],[37] are also well established factors of risk. Several population-based studies have associated moderate to high myopia with an increased

risk of glaucoma, independently of IOP [38]-[40]. Thin central corneal thickness (CCT) was found to be an additional risk factor among ocular hypertensive patients [41], [42]. More recently, vascular features such as lower ocular perfusion pressure (OPP) [43] and ocular blood flow [44] were pointed out as additional risk factors.

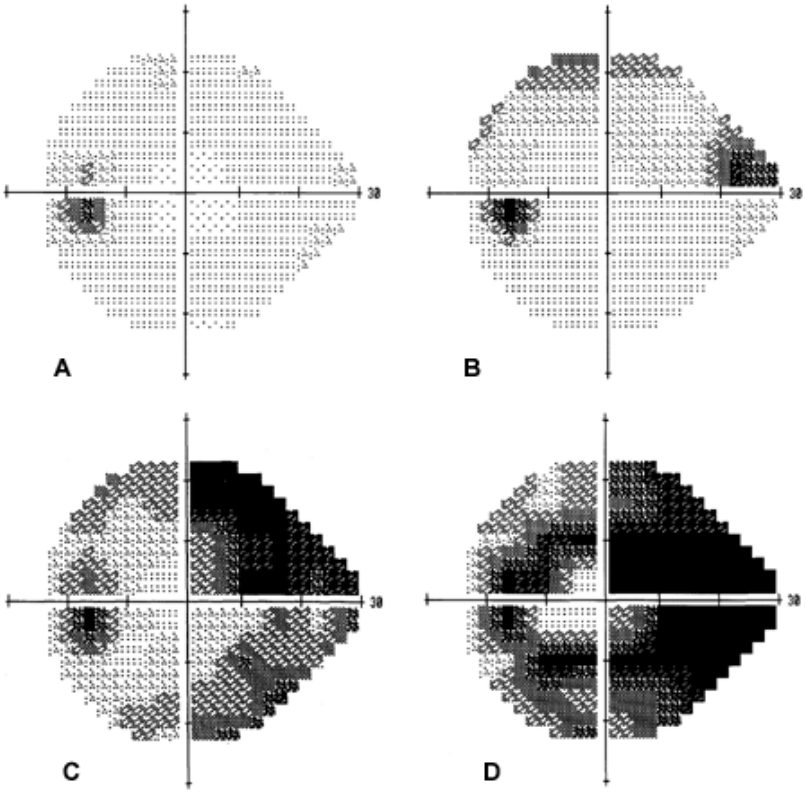


**Figure 2.14 – Standard automated perimetry results demonstrating progressive visual field loss in the left eye of a patient with uncontrolled glaucoma. A) Normal VF showing the location of the blind spot created by the optic nerve. B) The first abnormality is the loss of the VF in the superior and nasal portion. C) As damage progresses, visual field loss extends to involve both the superior and inferior portions of vision. D) In advanced stage of the disease extensive damage to the entire VF occurs, sparing the very central portion of vision [19].**

A comprehensive glaucoma exam includes five tests:

1. Measurement of intraocular pressure - Usually performed with a Goldman applanation tonometer, where IOP is determined from the pressure required to flatten the cornea. Normal IOP ranges from 12 to 21$mmHg$.

2. Gonioscopy - This exam helps to assess the status of the anterior chamber angle and to determine if the drainage canals are damaged.

3. Optic nerve head anatomy - Shape and color of the optic nerve as well as changes in the C/D are examined with ophthalmoscopy and measured using confocal scanning laser ophthalmoscopy (cSLO), a technique based on confocal microscopy used for retinal imaging, or OCT.

4. Retinal Nerve Fiber Layer (RNFL) thickness - Since thinning of the RNFL can be detected before there is visual field loss, thickness measurements around the optic nerve are crucial to diagnose and evaluate glaucoma progression. This parameter can be assessed with cSLO, scanning laser polarimetry or OCT.

5. Perimetry or Visual Field test (VF) - This test is performed to determine the location, size and shape of an eye's blind spots in order to detect damage resulting from glaucoma. After glaucoma diagnosis, VF tests must be performed one or two times a year.

All these parameters need to be tested periodically to assure an early detection and to track OAG progression. For example, alterations in the optic disc such as symmetrically enlarged C/D greater than 0.5, C/D ratio asymmetry between the two eyes of 0.2 or more, or highly asymmetric cup in one eye are physical characteristics suggestive of glaucoma that can be detected before visual field defects [19]. However there still is no method to predict the speed of progression of the disease.

The primary causes of the glaucomatous neuropathy remain unknown, however, several efforts have been made through the years trying to explain the mechanisms of the disease, resulting in two main theories: the mechanical theory and the vascular theory. In the mechanical theory the emphasis is on the damage to the optic nerve neurons as they exit through the lamina pores due to the curving or bowing of the LC by elevated IOP, which may lead to ischemia triggering cell death [45]. The vascular theory suggests that eyes with inherently poor vascular supply to the ONH are more predisposed to damage by elevated or normal IOP [46].

Differentiation between these theories has little clinical impact since currently, reduction in IOP, either pharmacologically or surgically, is still the only treatment proven to slow glaucoma progression [47],[48], which not only reduces mechanical pressures but may also increase blood flow, at least in patients with disturbed autoregulation. However, the fact that in some ethnic groups the majority of patients with open angle glaucoma have normal IOP [49], and that most subjects with elevated IOP (>21mmHg) never develop glaucomatous optic neuropathy or visual field loss [41] demonstrate that the current understanding of the disease is insufficient. As both mechanisms, mechanical and vascular, could be acting in many cases of glaucoma it is important to understand how they might work together.

## 2.4 Ocular Biomechanics in Glaucoma

Biomechanics seeks to understand the mechanics of living systems. It is the science that studies the origin and effects of the forces that act within and upon living organisms at the molecular, cellular, tissue, organ and body level. It helps to understand the normal function of an organism, to predict changes due to alterations and propose methods of artificial intervention [50] .

By definition, IOP is the normal force per unit area exerted by the intraocular fluids on the tissues that contain them. The mechanical response is a function of the individual eye's geometry, anatomy, and mechanical properties of the tissue, factors that contribute to determine the individual's susceptibility to IOP. Therefore, it is natural to consider that biomechanics plays an important role in glaucomatous neuropathy and the key challenge is then to understand how the combination of these factors is transduced into tissue damage.

The ONH is a region of special biomechanical interest because it is a discontinuity in the corneo-scleral shell, and such kind of discontinuities typically gives rise to stress/strain concentrations in mechanical systems [51]. It is subject to the mechanical action of IOP, scleral tension and cerebrospinal fluid (CSF) pressure and while the presence of such forces is physiologic, its change may be pathologic and might induce abnormal deformation of the tissues. Moreover, the LC attracts particular attention since it is a porous connective tissue that spans the scleral canal, mechanically supporting the retinal ganglion cells of the optic nerve as they pass through the scleral canal, providing a barrier to the pressure difference between the inside and outside of the globe and also being the place from where the blood flow enters the eye.

Ocular blood flow (OBF) is highly regulated in order to adapt to changing metabolic needs during changing visual function, to compensate for varying perfusion pressures and finally to keep the temperature at the back of the eye. Choroidal circulation is characterized by very high flow which accounts for 85% of the total blood flow in the eye. Arterial blood flow to the eye varies with the heart cycle and thus the volume, specially of the choroid, and the IOP are highest during systole and lowest during diastole [52]. Since significantly decreased blood flow in the juxtapapillary retina and the neuroretinal rim area has been observed in OAG patients even before there was visual field defects [53], it is possible that such reduction affects the biomechanical response of the tissue when diminishing the amplitude of the choroidal volume change.

The biomechanical paradigm suggests that the influence of IOP-related connective tissues stress (force/cross sectional area) and strain (local deformation) is central to both, the physiology and pathophysiology of the three ONH tissue types: 1) connective, i.e., load-bearing connective tissues of the peripapillary sclera, scleral canal wall, and lamina cribrosa; 2) axonal and 3) cellular, which includes astrocytes, glial cells, endothelial cells and perycites; as well as the volume flow of blood that nourishes them. Consequently, ONH connective tissues are exposed to substantial levels of IOP-related stress/strain even at normal levels of IOP.

Physiologic stress/strain induces a broad spectrum of changes in the connective tissues and blood vessels that are central to normal aging. Pathophysiologic stress/strain induces pathologic changes in cell synthesis and tissue microarchitecture that underline the two governing pathophysiologies in glaucoma, mechanical failure of the load-bearing connective tissues of the ONH and progressive damage to the adjacent axons by a variety of mechanisms [54]. For example, tissue deformation could alter the diameters of blood vessels supplying such tissue, and consequently, lead to hemodynamic alterations that could increase the susceptibility to ischemic damage.

It is believed that mechanical stress to the LC could lead to astrocyte reactivation which in turn may cause axonal degeneration and progressive and irreversible pathological changes in the ONH. Astrocyte reactivation could be a primary cellular response triggered by elevated IOP or ischemia, and/or a secondary cellular response activated by axonal degeneration [55].

Despite all the progress that has been achieved, a large fraction of what is known about the biomechanical properties of the ONH, the LC and the sclera rely on postmortem histological examination [56]-[58], invasive procedures such as cannulation [59], and more recently on static in vivo imaging techniques [60], [61]. It has been found that their biomechanical properties change with age. For example, peripapillary scleral structural stiffness increases significantly, the mechanical strain in this

region is significantly higher than that in the sclera farther away from the ONH, the temporal sectors exhibit the highest tensile strains [62]; and the mechanical compliance and resilience of the lamina cribrosa decreases [63]. It is possible that these age-related changes alone may be enough to modify the biomechanical properties of the ONH to the point that axonal damage occurs independently of IOP.

Due to the complexity of the study of the ONH and LC biomechanics in vivo, mathematical modeling has become the preferred approach to carry on such investigation. Research based on finite element computational modeling have led to two main conclusions: 1) The elasticity and thickness of the sclera may be the most important determinants of ONH stress and strain [64], and 2) IOP elevation causes the tissues of the ONH to be subject to a complex strain environment whose magnitude and distribution vary through the ONH. Furthermore, the highest magnitudes of all modes of strain (extension, compression, and shearing) occurred within the neural tissue regions and not within the lamina cribrosa [65], as previously believed.

Mathematical modeling has also been used to investigate ocular hemodynamics in glaucoma, allowing the inclusion of ocular mechanic properties such as the response of the ONH to variations in IOP, scleral tension and CSF pressure. Taking into consideration that such mechanical forces act on the retinal vasculature, it has been found that acute elevations in IOP induce an increase in the compression that the LC exerts on the central retinal artery walls and therefore a decrease in luminal diameter, blood flow and velocity in the CRA. Another model suggests that elevated IOP and reduced MAP might not contribute equally to low OPP, a major glaucoma risk factor, since retinal blood flow reductions due to IOP elevations benefit from a built-in compensatory mechanism that leverages the venous compressibility to increase the local blood pressure in the retinal vasculature. Moreover, it was shown that geometric characteristics of the LC strongly influence retinal hemodynamics, suggesting that

variations in individual susceptibilities to glaucomatous damage might result from a combination of mechanical, vascular and anatomic factors [66].

In order to have a better understanding of this biomechanical paradigm and the forces that lead to ONH and neural tissue damage it is of vital importance to have the capability to assess ocular biomechanics in vivo in a non invasive manner. It will allow to improve early glaucoma detection, the identification of rapidly progressing patients as well as to develop new and more appropriate treatment strategies.

Although there is still a long way ahead, considerable advances in noninvasive imaging technologies, such as optical coherence tomography, are now allowing researchers to start elucidating the dynamics of the eye in vivo.

# Chapter 3

# Optical Coherence Tomography

Biomedical imaging diagnostic techniques are in constant development, always in the search of devices that could provide higher resolution, fast real-time acquisition and in situ visualization to improve diagnosis and clinical management of diseases. One of such technologies is optical coherence tomography, first demonstrated in 1991 by Huang et al. [3]. OCT is a high resolution imaging technique that provides detailed information about the structure of live biological tissues in a noninvasive way, in vivo and in real time. It has become a clinical standard in ophthalmology due to the fact that no other method can perform noninvasive imaging of the eye with resolutions from 1 to 15$\mu m$, its reproducibility and accuracy. It can identify early stages of disease before physical symptoms and irreversible vision loss occurs, information that cannot be obtained with any other technique.

Several studies have been performed in order to compare the efficiency of OCT with well established methods, such as confocal scanning laser ophthalmoscopy and scanning laser polarimetry, finding for example, that the correlation between RNFL thickness and visual field sensitivity was stronger for measurements made with OCT compared with the other instruments, providing a significant structure-function asso-

ciation in glaucoma [67]. Furthermore, peripapillary RNFL thickness measured with OCT has shown the capability to differentiate between several stages of glaucomatous severity [68].

Due to all this advantages, OCT has become the preferred ophthalmic imaging modality in clinical practice as well as in medical research, not only to track the progression of ocular diseases but, thanks to the latest developments, to investigate the biomechanics of the eye as well as to perform dynamic studies such as the one presented in this work.

## 3.1 Theoretical Framework

Optical coherence tomography is an interferometric technique based on the property of the tissues to reflect light, where tissue structures are visualized due to their different optical scattering properties. In OCT, images are formed by measuring the echo delay and magnitude of backreflected or backscattered light in a cross-sectional plane of the tissue. In the following subsections the basic principles behind the OCT technique are described [69].

### 3.1.1 Michelson Interferometry

The most common interference detection method is based upon a Michelson interferometer, which configuration is illustrated in Fig 3.1. A monochromatic light source emits a beam toward a beamsplitter (BS), where the beam is split into two. One beam is reflected off the BS and then backreflected by a reference mirror. The other beam is transmitted through the BS and then backreflected by a surface. These two backreflected beams are recombined by the BS and then received by the detector.

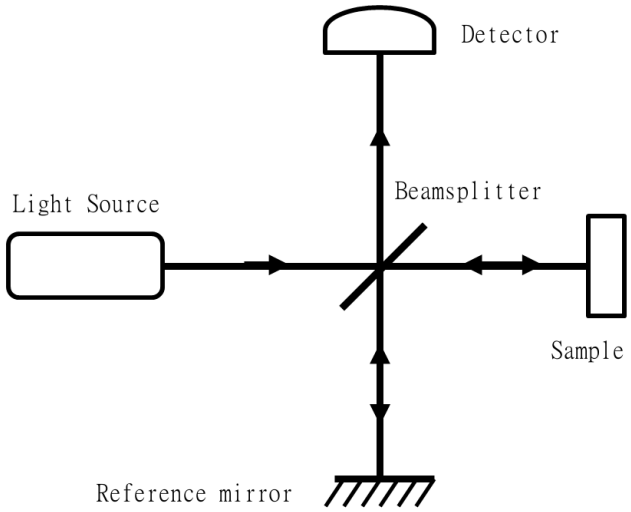


**Figure 3.1 – Diagram of a Michelson interferometer.**

If polarization is neglected, the two backreflected electric fields can be represented by

$$E_R = E_{R0} \exp(i(2k_R l_R - \omega t)), \tag{3.1}$$

$$E_S = E_{S0} \exp(i(2k_S l_S - \omega t)). \tag{3.2}$$

Here, subscripts $R$ and $S$ denote the reference and sample arms respectively. $E_{R0}$ and $E_{S0}$ are the electric field amplitudes of the two beams; $k_{R/S}$ the propagation constants; $l_{R/S}$ the two arm lengths measured from the splitting point at the beamsplitter to the backreflection surfaces and $\omega$ is the optical angular frequency. The factor 2 within the exponential arises from the round-trip light propagation in each arm. The electric field $E$ of the recombined beam is a superposition of the two monochromatic electric fields:

$$E = E_R + E_S. \tag{3.3}$$

The time-averaged light intensity detected is then

$$I(t) = \langle |E_R + E_S|^2 \rangle. \tag{3.4}$$

For monochromatic light

$$I(t) \simeq |E_R + E_S|^2. \tag{3.5}$$

Substituting Eqs. (3.1) and (3.2) into Eq.(3.5) yields

$$I = E_{R0}^2 + E_{S0}^2 + 2E_{R0}E_{S0}\cos(2k_S l_S - 2k_R l_R). \tag{3.6}$$

The cosine term on the right-hand side results from the interference between the two beams. The phase difference between the beams can be denoted as

$$\Delta\phi = 2k_S l_S - 2k_R l_R. \tag{3.7}$$

With a varying $\Delta\phi$, the interference term becomes an alternating signal that produces interference fringes, hence, the recorded $I$ is also called an interferogram.

If $k_R = k_S = k = 2\pi n/\lambda_0$, with $n$ the index of refraction and $\lambda_0$ the wavelength in vacuum, then

$$\Delta\phi = 2k(l_s - l_R) = 2\pi\frac{2n\Delta l}{\lambda_0}, \tag{3.8}$$

where $\Delta l = l_S - l_R$ is termed the arm length difference and $2n\Delta l$ the optical path length difference between the two beams. The interference signal varies with $\Delta l$ periodically. For monochromatic light, the fringes exhibit a sustained oscillation of constant amplitude.

### 3.1.2 Spectral-Domain OCT

Spectral domain OCT (SD-OCT) is a system based on spectral interferometry, i.e., Michelson interferometry using a broad-bandwidth source with the difference that the recombined beam is now dispersed by a spectrometer into its spectral components (Fig. 3.2). The corresponding spectral components interfere forming an spectral interferogram which is acquired by an optical detector array such as a charge-coupled device (CCD). The spectral interference pattern encodes in its spectral frequency content the entire depth-resolved structure of the sample at the position of the focal spot. Taking the inverse Fourier transform of the spectrum yields the backscattering reflectance from the sample versus depth or an A-scan. Transverse scanning across the sample provides 2D imaging (Fig. 3.3).

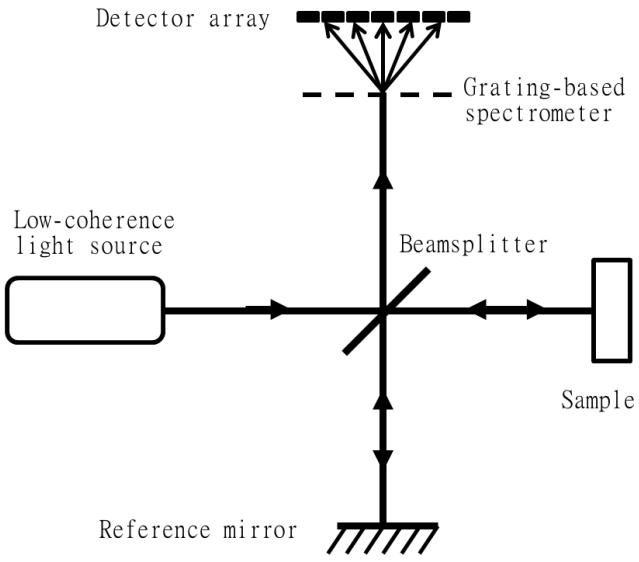


**Figure 3.2 – Schematic of an Spectral-Domain OCT system.**

In this case we have to consider multiple backscatterers at various depths on the A-scan. Thus, the sample beam consists of multiple partial waves emanating from

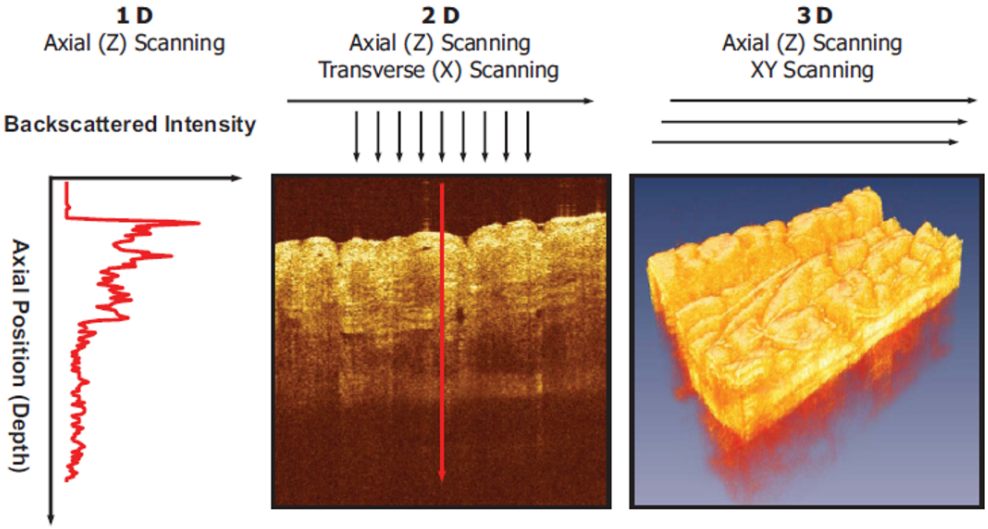


**Figure 3.3 – OCT generates cross-sectional and three-dimensional images by measuring the magnitude and echo time delay of light. A-scans measure the back reflection or backscattering versus depth. Cross-sectional images are generated by performing a series of axial scans at different transverse positions to generate a two-dimensional data set (B-scan), which is displayed as a grey scale or false color image. Three-dimensional data sets can be generated by raster scanning a series of B-scans. (www.rle.mit.edu/boib/ research/optical-coherence-tomography/)**

the backscatterers. The spectral components of the reference and the sample beams can be expressed as

$$E_R(\omega) = E_0(\omega) r_R \exp\left(i(2k_R(\omega)l_R - \omega t)\right), \tag{3.9}$$

$$E_S(\omega) = E_0(\omega) \int_{-\infty}^{+\infty} r'_S(l_S) \exp\left(i(2k_S(\omega)l_S - \omega t)\right) dl_S. \tag{3.10}$$

Here $E_0(\omega)$ denotes the electric field incident on the reference mirror or the sample surface; $r_R$ the amplitude reflectivity of the reference mirror; $r'_S(l_S)$, the object to be imaged, denotes the apparent amplitude reflectivity density or reflectivity per unit depth of the backscatterers along the A-scan in the sample.

If dispersion is neglected, we have

$$\frac{k_R}{n_R} = \frac{k_S}{n_S} = k = \frac{\omega}{c}, \tag{3.11}$$

where $n_R$ denotes the refractive index of the medium in the reference arm and $n_S$ the average refractive index of the sample. Apart from a constant scaling factor, the spectral interferogram is given by an equation similar to Eq.(3.5), this is

$$I(k) = |E_R(kc) + E_S(kc)|^2. \tag{3.12}$$

Substituting Eqs. (3.9) and (3.10) into Eq. (3.12), we obtain

$$\begin{aligned} I(k) = S(k)r_R^2 + 2S(k)r_R \int_{-\infty}^{+\infty} r'_S(l_S)\cos(2k(n_S l_S - l_R))dl_S \\ + S(k)\left|\int_{-\infty}^{+\infty} r'_S(l_S)\exp(i2k(n_S l_S))dl_S\right|^2, \end{aligned} \tag{3.13}$$

where the source power spectral density distribution $S(k) = |E_0(kc)|^2$. The first term on the right-hand side, referred to as the *reference-intensity* term, can be measured by blocking the sample arm ($r'_S(l_S) = 0$). The second term, referred to as the *cross-interference* term, encodes $r'_S(l_S)$ in the integral with a cosine function of the wave number, which is $k/(2\pi) = 1/\lambda$. The third term, the *self-interference* term, originated from the power spectrum $|E_S(kc)|^2$ contains the interference among the partial waves from the various samples depths.

The cross-interference term can be decoded to extract $r'_S(l_S)$ by taking the inverse Fourier transform. The deeper the origin of the backscattered partial wave, the higher the frequency.

Since we are only interested in the pathlength difference between both arms we will define $l_R$ as zero. If the reference point is outside the sample , a new even function

$\hat{r}'_S(l_S)$ can be defined as follows so that $\hat{r}'_S(-l_S) = \hat{r}'_S(l_S)$:

$$\hat{r}'_S(l_S) = \begin{cases} r'_S(l_S) & \text{if} \quad l_S \geq 0 \\ r'_S(-l_S) & \text{if} \quad l_S < 0 \end{cases} \tag{3.14}$$

With this new function, Eq.(3.13) can be written as

$$I(k) = S(k)\left\{r_R^2 + r_R \int_{-\infty}^{+\infty} \hat{r}'_S(l_S)\exp(i2kn_S l_S)dl_S + \frac{1}{4}\left|\int_{-\infty}^{+\infty} \hat{r}'_S(l_S)\exp(i2kn_S l_S)dl_S\right|^2\right\}. \tag{3.15}$$

If we change the variable of the integrals by $l_S = l'_S/2n_S$, and using the Fourier transform

$$F(k) = \mathfrak{F}\{f(l'_S)\}(k) = \int_{-\infty}^{+\infty} f(l'_S)\exp(ikl'_S)dl'_S. \tag{3.16}$$

Equation (3.15) can be rewritten as

$$I(k) = S(k)\left\{r_R^2 + \frac{r_R}{2n_S}\mathfrak{F}\left\{\hat{r}'_S\left(\frac{l'_S}{2n_S}\right)\right\}(k) + \frac{1}{16n_S^2}\left|\mathfrak{F}\left\{\hat{r}'_S\left(\frac{l'_S}{2n_S}\right)\right\}(k)\right|^2\right\}, \tag{3.17}$$

Applying the inverse Fourier transform

$$f(l'_S) = \mathfrak{F}^{-1}\{F(k)\}(l'_S) = \frac{1}{2\pi}\int_{-\infty}^{+\infty} F(k)\exp(-ikl'_S)dk, \tag{3.18}$$

to Eq.(3.17) we get

$$\mathfrak{F}^{-1}\{I(k)\}(l'_S) = \mathfrak{F}^{-1}\{S(k)\}(l'_S) * \left\{\frac{r_R^2}{2n_S}\delta\left(\frac{l'_S}{2n_S}\right) + \frac{r_R}{2n_S}\hat{r}'_S\left(\frac{l'_S}{2n_S}\right) + \frac{1}{16n_S^2}\mathfrak{C}\left\{\hat{r}'_S\left(\frac{l'_S}{2n_S}\right)\right\}\right\}. \tag{3.19}$$

Here, $*$ denotes convolution and $\mathfrak{C}\{\}$ the autocorrelation function operator. Changing the variable back $l'_S = 2n_S l_S$, Eq.(3.19) is converted to

$$\mathfrak{F}^{-1}\{I(k)\}(2n_S l_S) = \mathfrak{F}^{-1}\{S(k)\}(2n_S l_S) * \left\{ \frac{r_R^2}{2n_S}\delta(l_S) + \frac{r_R}{2n_S}\hat{r}'_S(l_S) + \frac{1}{16n_S^2}\mathfrak{C}\{\hat{r}'_S(l_S)\} \right\}. \tag{3.20}$$

The second term in braces is the A-scan image $\hat{r}'_S(l_S)$. The first and last terms represent spurious images. The first term is nonzero only at $l_S = 0$, which is outside the sample; thus, it can be easily removed.

To recover the true image, one may take another interferogram with $kl'_S$ shifted by $\pi$, which causes a sign change in Eq.(3.17):

$$I_2(k) = S(k)\left\{ r_R^2 - \frac{r_R}{2n_S}\mathfrak{F}\left\{\hat{r}'_S\left(\frac{l'_S}{2n_S}\right)\right\}(k) + \frac{1}{16n_S^2}\left|\mathfrak{F}\left\{\hat{r}'_S\left(\frac{l'_S}{2n_S}\right)\right\}(k)\right|^2 \right\}. \tag{3.21}$$

Taking the difference between Eqs.(3.17) and (3.21) yields

$$\Delta I(k) = S(k)\frac{r_R}{n_S}\mathfrak{F}\left\{\hat{r}'_S\left(\frac{l'_S}{2n_S}\right)\right\}(k), \tag{3.22}$$

where $\Delta I(k) = I(k) - I_2(k)$. The A-scan image can then be recovered by

$$\hat{r}'_S\left(\frac{l'_S}{2n_S}\right) = \frac{n_S}{r_R}\mathfrak{F}^{-1}\left\{\frac{\Delta I(k)}{S(k)}\right\}(l'_S). \tag{3.23}$$

Changing the variable $l'_S = 2n_S l_S$ leads to

$$\hat{r}'_S(l_S) = \frac{n_S}{r_R}\mathfrak{F}^{-1}\left\{\frac{\Delta I(k)}{S(k)}\right\}(2n_S l_S), \tag{3.24}$$

which shows that the subtracted and deconvolved spectral interferogram in the braces recovers an ideal image.

Figure 3.4 shows a simulated signal processing in SD-OCT with two backscatterers. The first panel shows the numerically simulated spectral interferogram $I(k)$. The second panel shows the inverse Fourier transform of $I(k)$, where a DC component and a spurious backscatter at $50\mu m$ appear due to interference between the partial waves from the two backscatterers. The third panel shows the inverse Fourier transform of $I(k)/S(k)$, i.e., of the deconvolved interferogram which sharpens the peaks. The last panel shows the inverse Fourier transform of $\Delta I(k)/S(k)$ as shown in Eq. (3.23). As can be appreciated in the graph, the FT of the subtracted and deconvolved spectral interferogram yields a much cleaner 1D image.

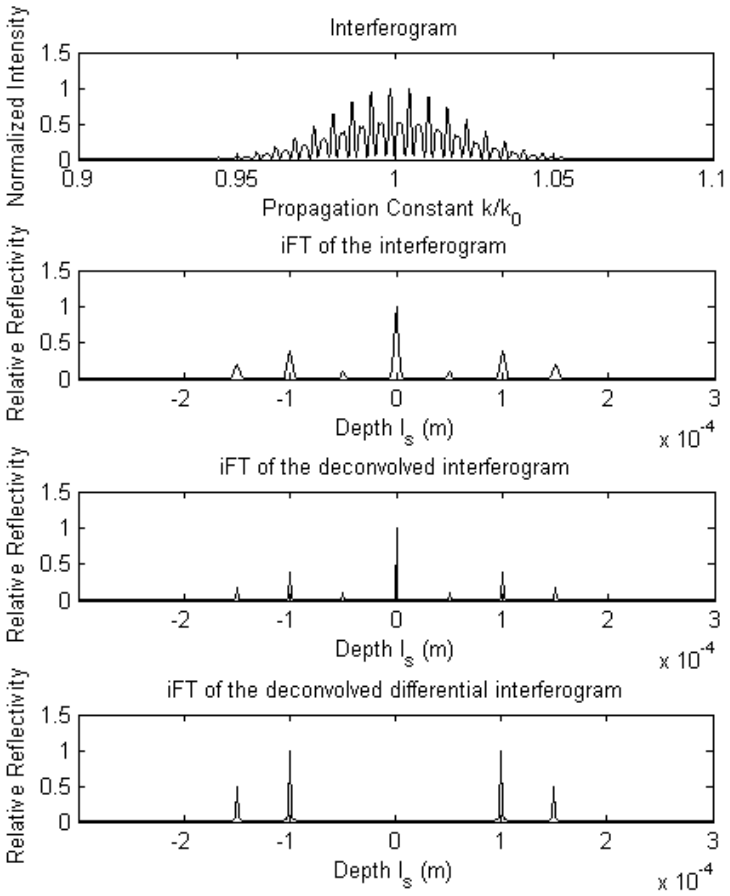


**Figure 3.4 – Numerically simulated signal processing in SD-OCT with two backscatterers [69].**

#### 3.1.2.1 SD-OCT Characteristics

The axial resolution in OCT imaging is determined by the coherence length of the light source, which means that high axial resolution can be achieved independently of the beam-focusing conditions. The coherence length $l_c$ is the spatial width of the field autocorrelation produced by the interferometer, which envelope is equivalent to the Fourier transform of the power spectrum. Thus, the axial resolution is inversely proportional to the width of the power spectrum. For a source with a Gaussian spectral distribution, the axial resolution of OCT in air is given by

$$\Delta Z = \frac{2\ln 2}{\pi}\frac{\lambda_0^2}{\Delta\lambda} = \frac{l_c}{2}, \tag{3.25}$$

with $\lambda_0$ the center wavelength of the light source and $\Delta\lambda$ the full width at half-maximum of the power spectrum.

The axial resolution in air equals half of the coherence length of the source owing to the round-trip propagation of the reference and sample beams. If other factors are negligible, the axial resolution in biological tissue is the axial resolution in air divided by the index of refraction of the tissue.

The CCD has a limited spectral range $\Delta\zeta$. The pixel spacing is chosen as $\Delta Z/2$ (Nyquist condition), which corresponds to one-half the axial resolution. The spectral range is therefore given by

$$\Delta\zeta = \frac{\pi}{2\ln 2}\Delta\lambda. \tag{3.26}$$

If the detector has N pixels, then the axial measurement range equals

$$Z_{max} = \frac{\Delta Z}{2}\frac{N}{2}, \tag{3.27}$$

N is divided by two because the Fourier transform of the real spectrum has conjugate symmetry about zero delay. This equation demonstrates that for a given source

bandwidth or coherence length, the axial scan range is determined by the number of pixels.

## 3.2 Double Scanning SD-OCT

In 2012, when this research project was started, video recording was not an option in commercial OCT devices. Since we are interested in the ocular dynamics and the biomechanical properties of the eye, the determination of ocular rigidity in vivo is of vital importance in the understanding of axonal damage in glaucoma. Therefore, based on a home-made SD-OCT system, previously developed in our laboratory to measure pulsatile displacements of the ocular tissues [70], a device was assembled with the purpose of determine ocular rigidity.

The proposed approach consists on imaging simultaneously the cornea and the retina, acquiring sequences of images at video rate for up to $20s$, from where the axial displacement of both tissues due to pulsatility can be measured. Then, changes in the axial distance between the cornea and the retina can be used to asses ocular volume changes during the cardiac cycle. This parameter determined from the OCT image series could therefore be employed to determine ocular rigidity through Friedenwald's equation [71], since it characterizes the relationship between pressure and volume changes in the eye,

$$\ln\left(\frac{IOP}{IOP_0}\right) = K(V - V_0), \tag{3.28}$$

where $K$ is the ocular rigidity coefficient, which describes the combined structural stiffness of the sclera, choroid, Bruch's membrane, retina and cornea.

The optical setup consists in a SD-OCT system with two sampling arms and two reference arms. The source, a superluminescent diode (Superlum, Cork; $\lambda = 844nm, \Delta\lambda = 46nm$), is coupled into a fiber-based Michelson interferometer where an

80/20 fiber coupler is used to generate the reference and sampling beams respectively. The sample beam, which has a total power of $640\mu m$, is collimated and then divided in two by a polarizing beamsplitter, each polarization is propagated independently. One beam is kept collimated and used to image the retina, the second beam is focused into the cornea. The reference beam is passed through a 50/50 fiber coupler and a neutral density filter in order to decrease its intensity and avoid saturation in the CCD. Then, the beam is collimated and a beam splitter generates the two reference arms. Finally, the recombined beam is dispersed by a diffraction grating of 1200 $lines/mm$ and focused into a linear CCD camera (Spyder 3, Dalsa Technology). The experimental setup is shown in Figure 3.5. The reference mirrors are adjusted in such way that both layers fit within the dynamic range of the spectrometer and the signal detected by the CCD is a mixture of both spectral interferograms. After Fourier transformation, both images can be retrieved simultaneously in the same frame. Figure 3.6 shows the OCT image obtained from a model of the eye.

Although the double scanning SD-OCT prototype is functional, the quality of the images obtained is very low as can be seen in Fig. 3.6. In order to improve it, polarization has to be controlled in the rest of the interferometer, not only at the sampling arm, and eye dispersion has to be compensated. However, when this point was reached, a commercial OCT device with a custom-modified software was available in our laboratory, which has the capability of recording video rate image series and included the recently developed technology of enhanced depth imaging (EDI), a modality that adjust the focusing to improve visualization of external retinal layers, as well as an eye tracker system, assuring the scanning of the same region of the eye trough the whole image sequence. Such improvements in OCT imaging made us change our approach to measure ocular rigidity.

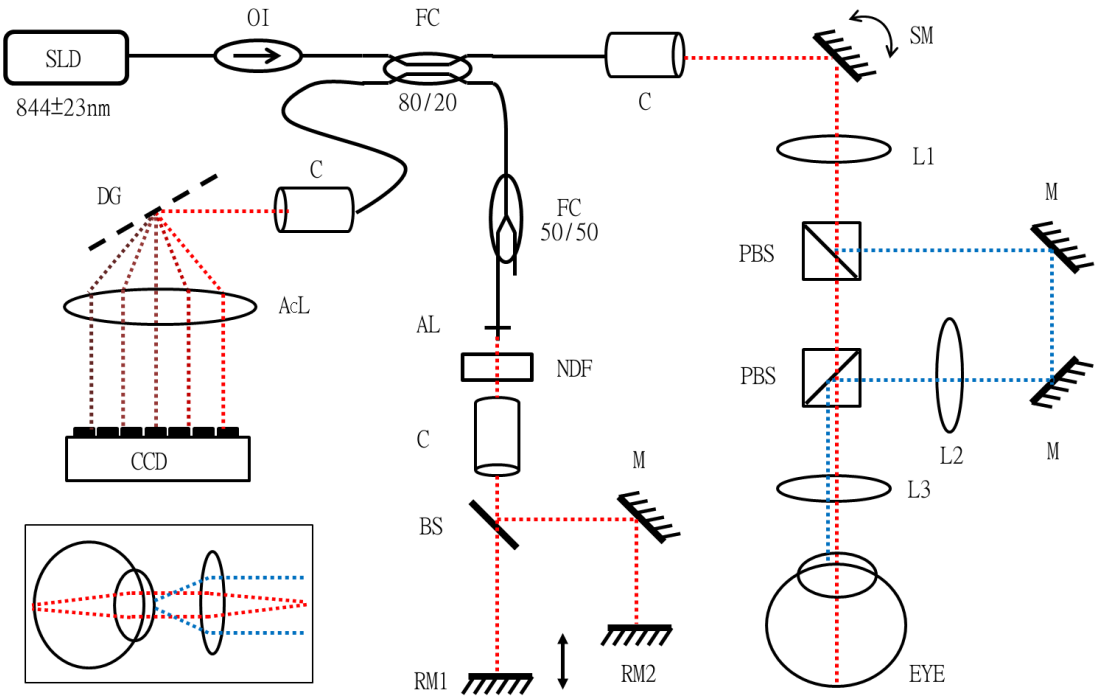


**Figure 3.5 – Schematic diagram of the double scanning SD-OCT prototype. In order to simultaneously scan the cornea and the retina, the sample beam was split in its two polarization components (red and blue dotted lines) and each one is used to scan a different tissue; correspondingly, two reference arms needed to be employed. Each obtained A-scan contains the locations of both ocular layers. The inset shows how the two scanning beams are focused into the eye. Optical components: SLD - superluminescent diode, OI - optical isolator, FC - fiber coupler, C - collimator, SM - scanning mirror, L - lens, L1 - 88.3mm, L2 - 75.6mm, L3 - 50.2mm, PBS - polarizing beam splitter, M - mirror, NDF - neutral density filter, AL - aspheric lens, BS - beam splitter, RM - reference mirror, DG - diffraction grating (1200 lines/mm), AcL - achromatic lens.**

Considering that 85% of the total blood flow in the eye is due to the choroid, it is possible to attribute the pulsatile volume changes to choroidal pulsation. Thus, since EDI allows a more clear visualization of the choroid, the new strategy was focused on measuring pulsatile choroidal volume changes produced by blood inflow from macular video rate OCT image series. In this case, global ocular volume fluctuations are derived from frame to frame choroidal thickness variations using an approximate eye model, which combined with IOP and ocular pulse amplitude measurements can be used to determine ocular rigidity through Eq. 3.28 in a noninvasive manner.

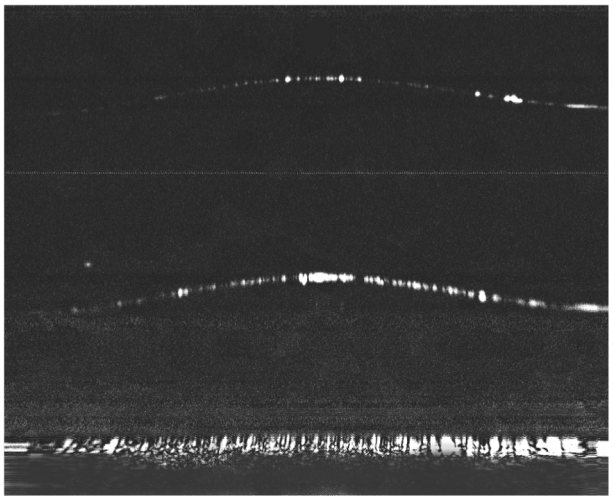

**Figure 3.6 – OCT image of the cornea and retina of a model of the eye obtained with the double scanning SD-OCT prototype.**

This side project was carried out in parallel to the one presented in this work. Since it provides very useful information about the biomechanics of the eye, information that will help in the understanding of retinal tissue deformation, it was worth to mention. Furthermore, ocular rigidity measurements are intended to be added to the protocol developed in this thesis in a future work. In the meantime, a preliminary study of the relationship between ocular rigidity and retinal deformation in the macular region is included in Chapter 7. The characterization was performed using the same set of images previously acquired for the rigidity study. For a detailed description of the ocular rigidity measurement and the validation of the method please see Ref. [72].

# Chapter 4

# Objectives and Study Design

## 4.1 Working Hypothesis

The choroid has the highest blood flow per gram of tissue of any organ in the human body being 80% pulsatile [73]. Considering the fact that these pulsations drive the retina forward while expanding the sclera [74],[75], it is natural to think that the axons running from the retina and through the lamina cribrosa could therefore be strained in systole as the retina moves forward (Fig 4.1). Furthermore, it has been found that choroidal pulsations increase with both, higher IOP [76] and lower arterial blood pressure [77], two major risk factors for glaucoma.

Following this reasoning, we hypothesize that

> *Choroidal pulsatility would result in a periodic deformation of the axons that constitute the optic nerve. The magnitude of this deformation would depend on the biomechanical properties of the tissue as well as the pulsatility of the choroid, and could be correlated with the axonal damage and loss of retinal nerve fiber layer in glaucoma.*

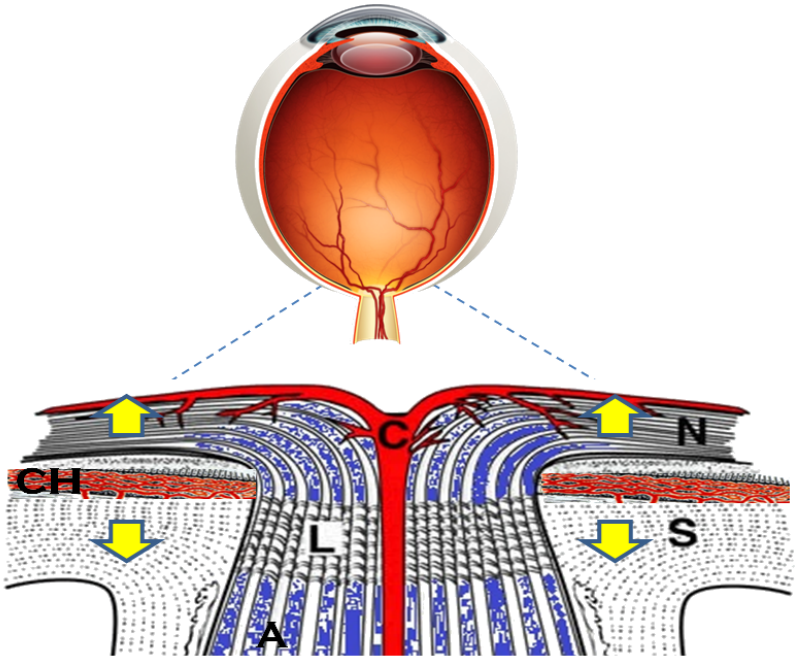


**Figure 4.1 – The filling of the choroid by the blood stream causes its expansion, pushing forward the retina and backwards the sclera (yellow arrows), resulting in a periodic deformation of the axons that could be correlated with glaucoma insult. (C - central retinal artery, N - nerve fiber layer, L - lamina cribrosa, CH - choroid, S - sclera, A - axon).**

Therefore, the motivation of this work as well as the cohort of patients included in this study is to characterize dynamic changes of the ocular fundus related to the development and progression of glaucoma.

## 4.2 Objectives

Within the above mentioned framework and aiming to have a better understanding of the influence and relation of the ocular pulsatility and the outlined risk factors of the glaucomatous pathology, the general objective of this doctoral research is to investigate and characterize the dynamics of the ocular fundus as well as its clinical significance at different stages of the disease, making use of video rate SD-OCT image series. In particular:

- Design imaging protocols that allow retinal deformation measurements and that could be implemented in the clinic.
- Develop fully automated image analysis algorithms to quantify pulsatile tissue displacements on the optic nerve.
- Recruitment of volunteers for OCT imaging.
- Characterize the peripapillary retinal deformation in patients that cover the most representative part of the glaucoma spectrum.
- Investigate the relationship between the proposed biomechanical descriptor and the ocular, vascular and demographic parameters from the eye exam.

## 4.3 Study Design

The design of the study is cross-sectional. Only one visit is required per subject in which a standard eye exam is performed and complementary information is obtained from the patient's medical records. Exclusion criteria, groups' definition and clinical procedure are described in the following subsections.

### 4.3.1 Subjects

Volunteers of 40 years of age or older were recruited, from november 2012 to november 2015, at the Glaucoma Clinic of the Maisonneuve-Rosemont Hospital's Ophthalmology Department in Montreal. Patients at different stages of the glaucomatous neuropathy were selected and classified as follows,

- Early Open-Angle Glaucoma - Typical glaucomatous ONH rim changes; rim notching, if present, not extended to the edge of the disc, visual field MD $> -6.0dB$, no previous incisional glaucoma surgery, no IOP restrictions.

- Open-Angle Glaucoma Suspect - Glaucoma suspicious optic disc, i.e., vertical cup to disc ratio not greater than 0.8, no notching, flame hemorrhage or focal retinal nerve fiber layer defect, normal visual field, no IOP restrictions.

- Ocular Hypertensive - History of IOP $> 24mmHg$ on at least two occasions, normal visual field, normal optic disc and no evidence of progression.

- Normal - Age matched subjects with healthy eyes, i.e., IOP$\leq 21mmHg$, normal visual field, healthy ONH with no characteristics suspicious of glaucoma and no history of glaucoma.

One eye was studied per patient. If both eyes were eligible, the eye with less damage on automated perimetry was chosen and indicated by the specialist. No pupil dilatation was required at any time. Exclusion criteria were corrected visual acuity of 20/50 or worse, history of ocular surgery with the exception of remote cataract surgery, and/or any other ocular disease such as angle-closure glaucoma.

### 4.3.2 Ethical Considerations

This study was performed under protocols approved by the Institutional Review Board of the Maisonneuve-Rosemont Hospital and its Ethics Committee. The research protocol follows the tenets of the Declaration of Helsinki. Informed consent was obtained from all participants after the nature and possible consequences of the study were fully explained.

### 4.3.3 Methodology

With the purpose of measuring retinal tissue displacements accurately during the cardiac cycle in real time, a commercial SD-OCT device (Spectralis OCT Plus[1] , Heidelberg Engineering, Germany) was used for imaging, the software of which has been custom-modified to record video rate image series allowing the export of raw images, including an extensible markup language file (XML) containing the imaging parameters as well as the time stamp of each one of the images acquired. The latter information is essential to perform frequency movement calculations related to the cardiac cycle since the device is equipped with an eye-tracker system that halts acquisition, to avoid movement artifacts, when the current scanned area does not match with the reference position.

The first step of the protocol corresponds to the OCT imaging of the optic nerve head. Series of OCT line scans of the same region of the ONH are acquired at $20Hz$ for $20s$. Each series consists of 401 high resolution images (496x768 pixels) acquired over a $15^{o}$ field of view ($5mm$ approx.) that covers cup, rim, and peripapillary retina (Fig. 4.2). Due to the need of an acquisition rate several times higher than the heart rate, quality had to be sacrificed in order to achieve it. Consequently, the maximum number of averaged B-scans to generate the final image gets restricted to two. Along with the image series, the pulse trace of the subject under examination is recorded with an in-house pulse oxymeter through a LabView platform that allows its visualization in real time, information that will be used during the analysis to determine the heart frequency.

Immediately after imaging, all participants undergo a standard eye exam. Intraocular pressure (IOP) and ocular pulse amplitude (OPA) are measured with a PASCAL dynamic contour tonometer (Ziemer Ophthalmic Systems AG). The Ocular Response

[1]Device specifications - SLD: $\lambda_c = 870nm, \Delta\lambda \simeq 47.7nm$; Scan depth in tissue: $1.9mm$; maximum A-scan rate: $40kHz$, Digital resolution: $3.9\mu m$ axially and $6\mu m$ laterally.

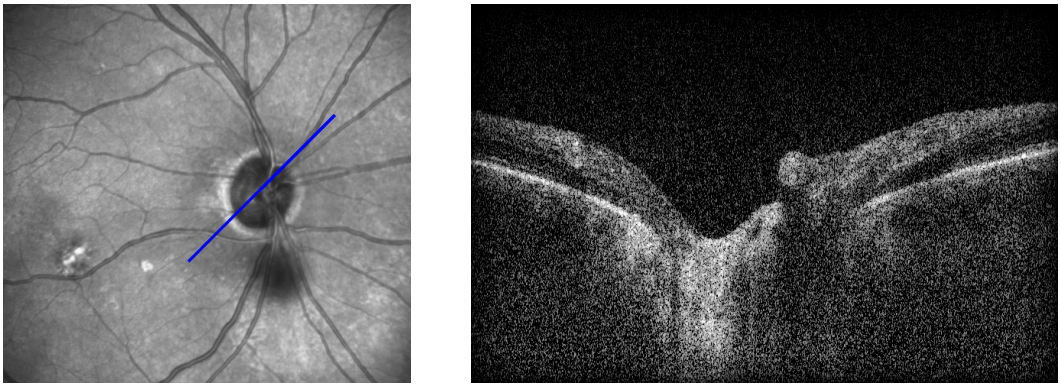

(a) (b)

**Figure 4.2 – Typical image pair from the series. a) Fundus image of a right eye showing the scanned line through the optic nerve head, in this case at 45º with respect to the fovea to disc axis. b) Corresponding optical coherence tomography image with two averaged frames.**

Analyzer (Reichert Ophthalmic Instruments) is used to measure corneal hysteresis (CH), corneal resistance factor (CRF) and central corneal thickness (CCT). Axial length (AL) is determined using an IOLMaster optical biometer (Carl Zeiss Meditec AG).

A brachial arterial blood pressure measurement performed with an automated sphygmomanometer (Spot Vital Signs NIBP, Welch Allyn Inc.) is also included in the exam. Systolic and diastolic blood pressures (SBP, DPB) are used to compute the following parameters:

Mean Arterial Blood Pressure MAP = DBP + 1/3 ( SBP-DBP).

Mean Ocular Perfusion Pressure MOPP = 2/3 MAP - IOP.

Systolic Perfusion Pressure SPP = SBP - IOP.

Diastolic Perfusion Pressure DPP = DBP - IOP.

Finally, in order to have variables related with glaucoma severity, the average peripapillary retinal nerve fiber layer (RNFL) thickness and vertical cup to disc ra-

tio (C/D) from a 200x200 OCT optic disc cube protocol (Cirrus OCT, Carl Zeiss Meditec AG), and the visual field mean defect (MD) from automated perimetry (SITA-Standard 24-2, Humphrey Visual Field Analyzer II, Carl Zeiss Meditec AG) are retrieved from the patient's ophthalmic medical record. The tests must have been performed within the 2 months previous to the exam.

# Chapter 5

# Automatic Segmentation of the Optic Nerve Head and Pulsatile Deformation Analysis

In order to investigate the dynamics of the tissues due to pulsatility, it becomes necessary to have an image acquisition rate several times higher than the heart rate, which implies that only few consecutive B-scans can be merged to conform the final image, making them very susceptible to noise and low quality when compared to those typically acquired, as can be seen in Fig. 5.1. Such characteristics, plus the fact that each series comprises hundreds of images, make the available edge-detection algorithms inadequate to accomplish our measurements. For example, active contour algorithms may seem a good choice to achieve accurate border delimitation [78], [79]. However, although it is possible to define a fixed rectangular initial contour that encloses the whole optic nerve, and the main parameters can be optimized for a set of similar images, the number of iterations necessary to accurately delineate the ILM may vary depending on the size and shape of the ONH, with a computation time in

the order of tens of seconds for a single image [80], [81], making this kind of method inappropriate for large image sets.

Furthermore, retinal deformation is in the order of dozens of microns, making inaccurate delineations a source of error for adequate assessment of the dynamic behavior of the tissue. Therefore, additional to the imaging protocols, an important part of this doctoral research is devoted to develop and test specific image processing and analysis algorithms fully automated and robust enough to successfully segment ONH OCT images allowing deformation measurements.

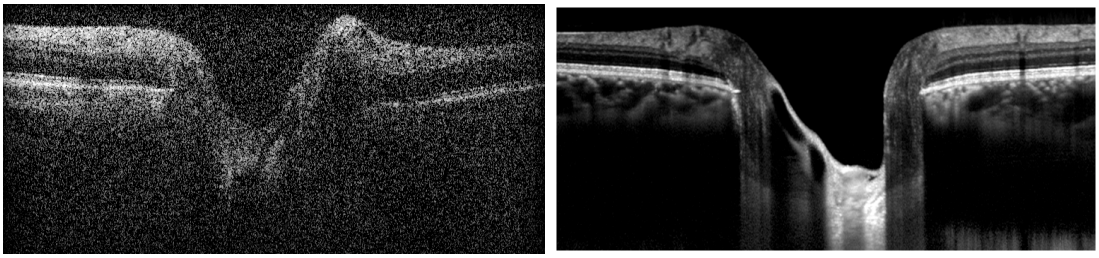

(a) (b)

**Figure 5.1 – OCT image comparison. a) OCT image from the sequence acquired at 20$Hz$, made of 2 averaged B-scans with a Spectralis quality score ($Q$) of 18 $dB$. b) Typical OCT image used in clinical practice made of 100 averaged B-scans with $Q = 40dB$.**

The proposed approach consists on delineating accurately the peripapillary retina and the ONH, i.e., the inner limiting membrane (ILM), on the OCT images and track the position of specific regions in time, this is frame to frame, in order to quantify retinal displacement [82]. The parameters used in the final segmentation algorithm were optimized as follows: a set of 25 images that include healthy and several stages of glaucomatous eyes randomly selected from the database, with Spectralis quality scores[1] ($Q$) ranging from 10 $dB$ (below marginal) to 40 $dB$ (excellent), were presented to five observers.

[1]The Spectralis image quality score is defined as $Q = 10 * \log_{10}(SNR)$, where $SNR = I_{max}(low\,resolution\,image) - I_{max}(image\,without\,sample)$.

Images were segmented varying the values of the main parameters and, raters, masked to parameters and values, were asked to choose the best segmentation for each "unknown" parameter using a graphical user interface specially created with this purpose. The most voted values were selected and kept fixed for all images. All the analysis routines described in the following have been programmed in Matlab (The MathWorks, Inc.).

## 5.1 Preprocessing

In order to prepare the images for segmentation, a preprocessing sequence is required. The first step is to apply a 2-D median filter of size 7x7 pixels for rough speckle noise removal. For alignment, to correct bulk tissue displacements between images, the Matlab intensity-based automatic image registration function was used with mean-squared error metric and one-plus-evolutionary optimizer. The registration is limited to rigid transformations, translation and rotation, taking as a reference the first acquired image.

After the alignment, images are submitted to a two-step contrast enhancement technique to suppress features that may lead to erroneous boundary detection. First, intensity exponentiation ($I(z)^2$) is applied to eliminate floaters near the cup and attachment points in case of vitreoperipapillary detachments, like those observed in Fig.5.2a. Afterwards, intensity exponentiation + attenuation compensation [83] using the formula

$$I_c = \frac{I^3(z)}{2\int_z^\infty I^3(u)du}$$

(with $I_c$ the contrast enhanced and compensated image and $I(z)$ the original image), is required to compensate inhomogeneities due to retinal blood vessels and to sharpen

the edges as shown in Figure 5.2b. This step is crucial to increase the number of eligible videos since around 30% of the eyes under investigation show such characteristics.

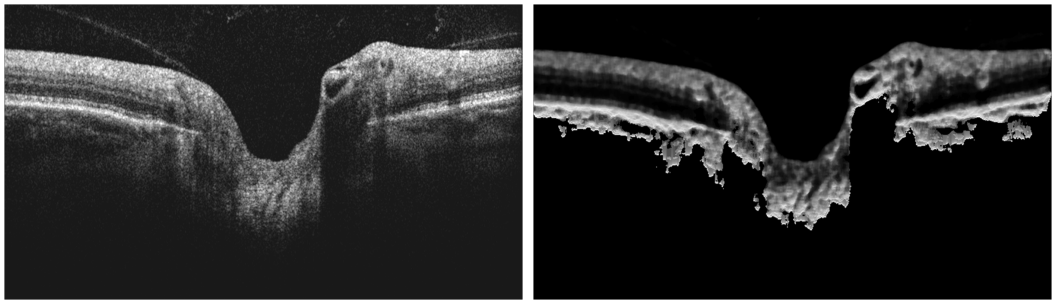

(a) (b)

**Figure 5.2 – Preprocessing example: a) Original ONH image showing peripapillary vitreous detachments on both regions, nasal and temporal. b)Same image after median filtering and contrast enhancement steps applied.**

## 5.2 Inner Limiting Membrane Segmentation

In order to separate the outer layer of the retina from the vitreous, another median filter (7x7 pixels) is applied. Since the image has been previously submitted to contrast enhancement, a threshold of 10% of the maximum intensity is enough to discriminate between the retina and the remaining noise near the edges and it is used to generate the corresponding binary image. An increase of the threshold value results in the loss of the vitreal-retinal boundary information in most cases. The next step is to remove rough edges and bridges by morphological closing with a squared structuring element of 3 pixels width (Fig 5.3b). Pixel labeling of eight connected objects is then used to remove the remaining spurious pixels in the vitreous, usually corresponding to highly reflective floaters, by only keeping objects with more than 1000 elements.

The ILM is set to the most anterior foreground pixel of each A-scan. To exclude misallocated points at the edges of the cup, distances in the axial direction between adjacent contour points $c(x)$ are calculated: $\Delta z_i = c(x_i+1) - c(x_i)$, and we search for

distances of $|\Delta z|$ that are equal or greater than $27\mu$m. When a negative targeted value is followed by a positive one, and separated by maximum 10 points in the transversal direction ($x$), such interval is removed and replaced with a spline-interpolating curve. Figure 5.3c shows the segmented profile.

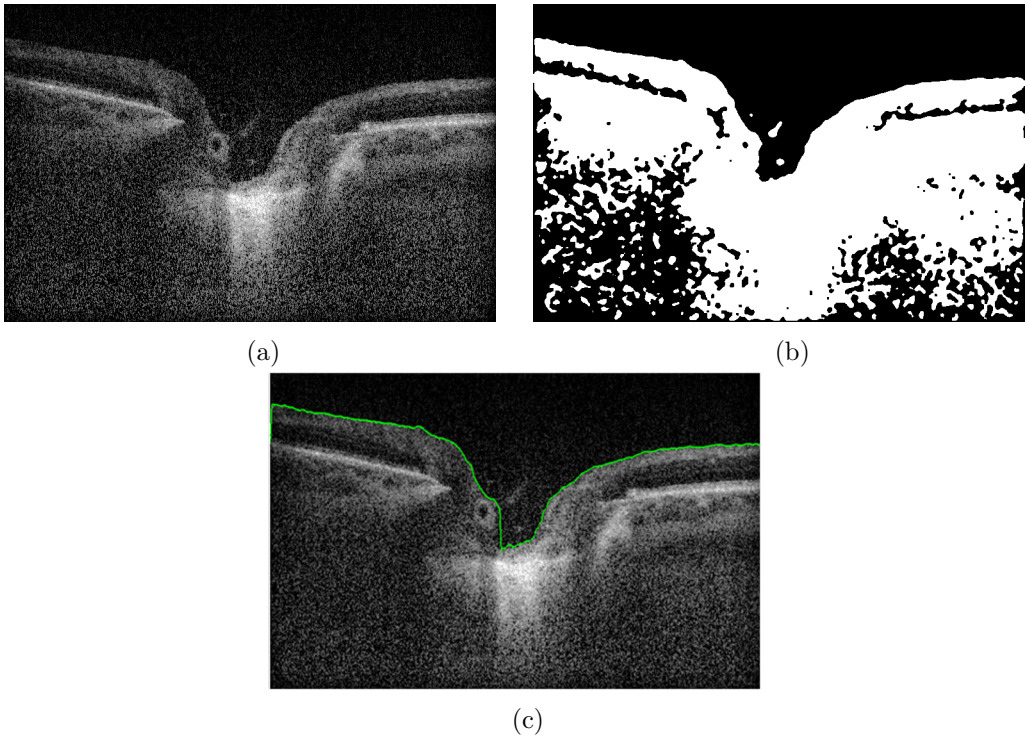

(a) (b)

(c)

**Figure 5.3 – Example of some segmentation steps: a) Original image. b) Binary image after morphological closing. c) Final ILM profile displayed on top of the original image. The edge is detected as the first nonzero pixel in each A-scan and interpolated with smoothing splines.**

When the segmentation has been performed for the full image series, the result is a set of 401 ILM profiles. With the purpose of discarding automatically the profiles where the ILM delineation has failed, all the profiles are aligned in the axial position taking the deepest point of the cup as reference (Fig. 5.4a), and the average and standard deviation (S.D.) of the depth values ($z$) at each A-scan position are computed. Outliers are then tagged in two steps. First, we identify outlier pixels in each one of the profiles, defined as those points located at a distance of 3 S.D. or more from the average value in each A-scan. Next, the S.D. of the number of outlier pixels per

curve is determined, and profiles with more outliers than such S.D. are discarded. Figure 5.4b shows the final profiles that are going to be used in the analysis. In general, the number of discarded profiles per image series is not higher than 15.

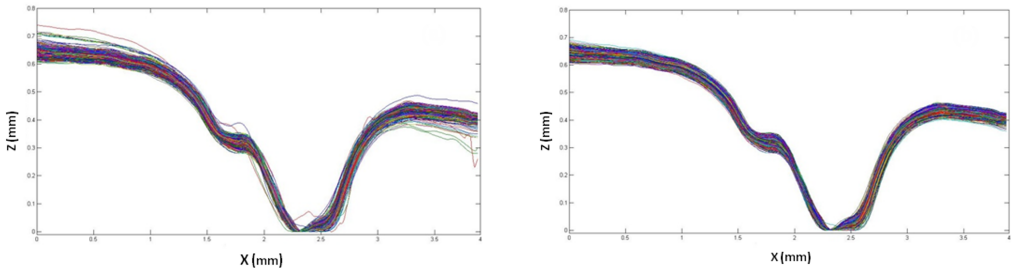


(a) (b)

**Figure 5.4 – a) Profiles resulting from segmentation of the full image series plotted together after vertical shift. Some of the profiles show inaccurate segmentation at the bottom of the cup or the peripapillary retina, hence, a two-step outlier identification is carried out. b) Final profiles after outlier elimination process.**

## 5.3 Deformation Analysis

Once the final ILM profiles are obtained, retinal deformation can be determined from the image series by quantifying changes in the distance measured from the peripapillary retina to the prelaminar tissue (PPR-PLT distance). Since the major blood vessels cross the optic nerve through the retina on the nasal region, we have decided to investigate the temporal side, where vessels are less dense. Three regions of 200$\mu$m are selected along the temporal side to perform the measurements ($T$, $T2$ and $T3$) starting at the Bruch's membrane opening and separated by 160$\mu$m, as shown in Fig. 5.5a . Distances are averaged within each region, resulting in three PPR-PLT values per image. Finally, Neuro-Peripapillary (N-PP) retinal deformation in each region is defined as the standard deviation of the PPR-PLT distances of all images $DT, DT2$ and $DT3$ (Fig. 5.5b).

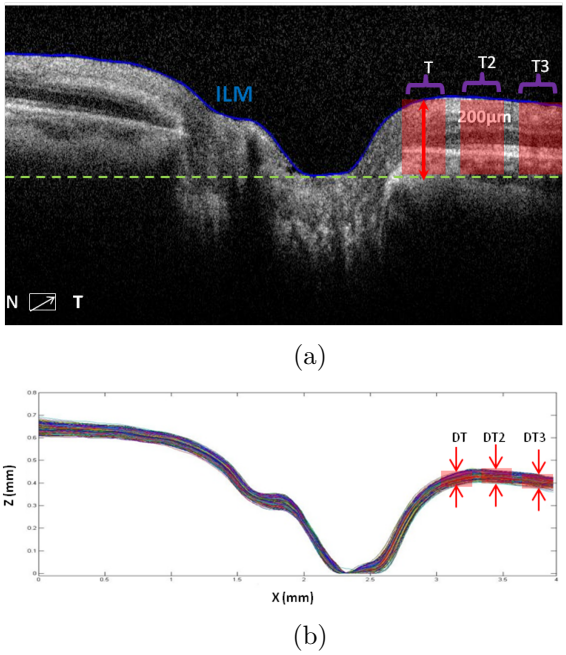


**Figure 5.5 – Deformation measurements: the green line in a) sets the reference at the deepest point of the ONH, and the red arrow represents the PPR-PLT distance measured to determine Neuro-Peripapillary retinal deformation. Three PPR-PLT distance values are calculated per frame, corresponding to the regions $T$, $T2$ and $T3$. b) Deformation is defined as the standard deviation of the PPR-PLT distances of all profiles in each one of the regions (red rectangles).**

Since the fluctuation of the PPR-PLT distance in each one of the regions showed a very similar behavior (Fig. 5.6), and aiming to have a deformation value representative for the whole temporal region, the average of the three deformation values ($DT, DT2$ and $DT3$) is computed and taken as the final neuro-peripapillary retinal deformation.

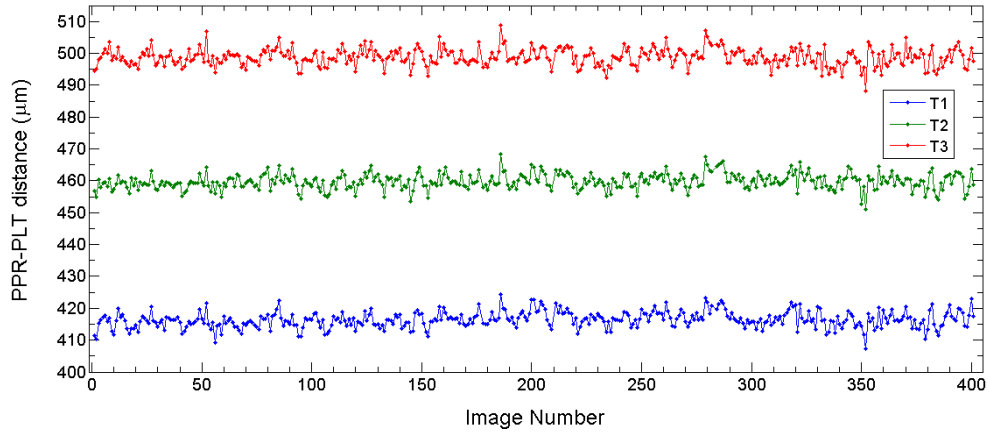


**Figure 5.6 – PPR-PLT distances measured along the full image series. The fluctuation of the distances measured in each one of the regions ($T$, $T2$ and $T3$) shows the same tendency with very similar deformation values, thus the final N-PP retinal deformation of an image series corresponds to the average of the deformation values of the three regions.**

Considering that the displacement measured has more than one periodic movement, e.g., the pulse and the respiration, it is important to assure that the N-PP retinal deformation observed is mainly caused by the blood flow pulsatility, and since the time stamp of each one of the images is known (see Fig. 5.7), spectral analysis is performed as last step of the algorithm.

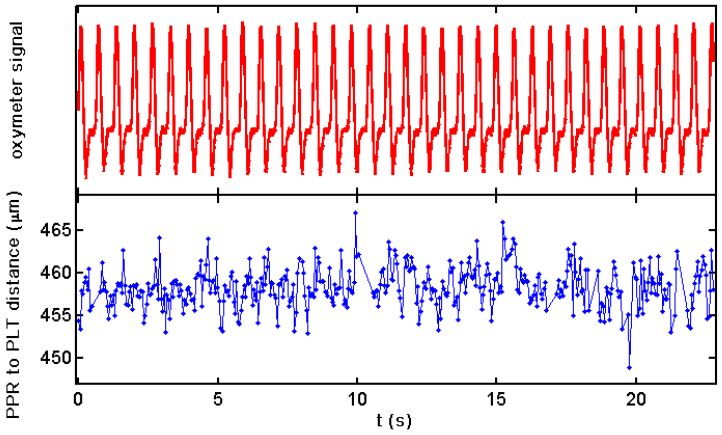


**Figure 5.7 – Temporal series: oximeter signal recorded during the OCT imaging (top) and measured PPR-PLT distance over time (bottom).**

A consequence of the eye tracker system is that images within a series are not taken at regular time intervals thus, the Lomb-Scargle periodogram have to be used, instead of the Fast Fourier Transform, to determine the frequency spectrum of the measured retinal displacement. Such spectrum is then compared with that corresponding to the oximeter signal as can be seen in Figure 5.8. Deformation results are rejected at this stage if it is not possible to identify the heart frequency in the periodogram of the PPR-PLT distances.

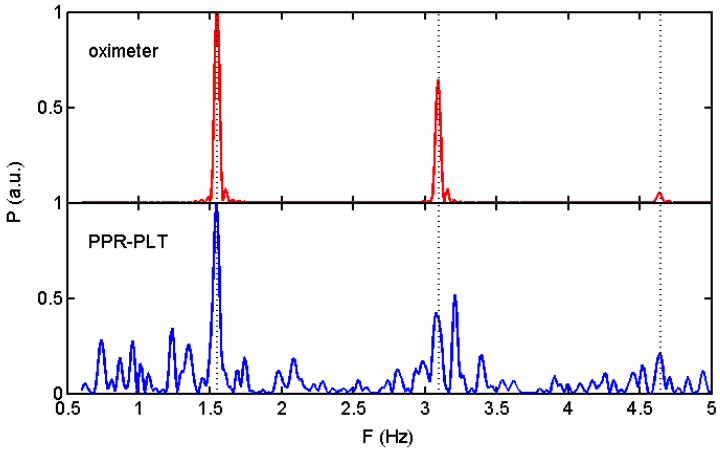


**Figure 5.8 – Spectral analysis. Top: frequency spectrum of the oximeter signal that reveals the heart frequency of the subject, in this case $F_H = 1.55Hz$. Bottom: frequency spectrum of the PPR-PLT distance series that shows the heart frequency as the main spectral component of the retinal deformation. Dashed lines correspond to the heart frequency and its two first harmonics ( $2F_H, 3F_H$), which can be easily identified in both spectra.**

As summary, Figure 5.9 shows a diagram of the full analysis process to determine neuro-peripapillary retinal deformation. The method has been published in [82].

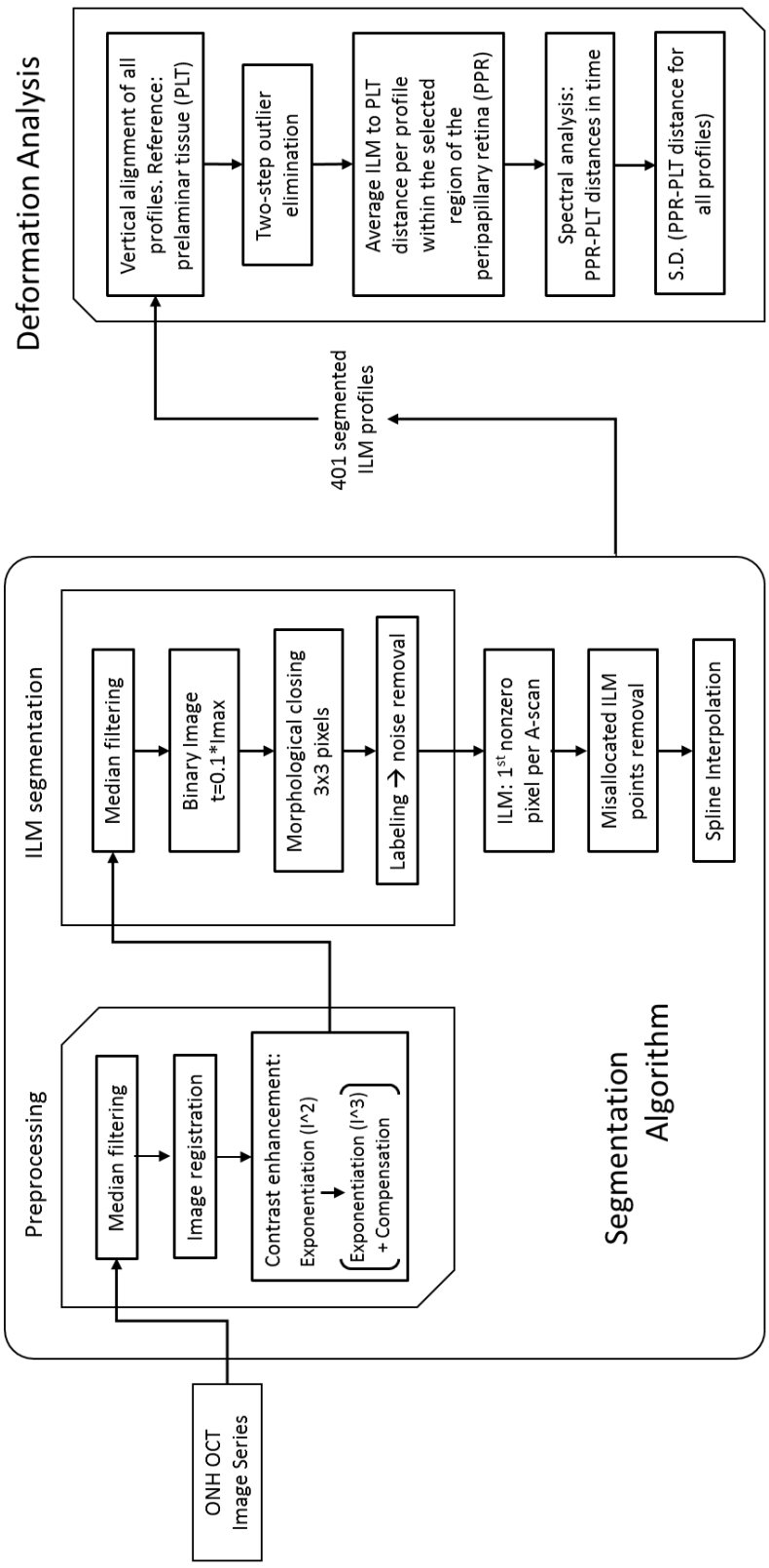


**Figure 5.9 – Schematic representation of the ILM segmentation and deformation analysis algorithms proposed to measure Neuro-Peripapillary retinal deformation from video rate OCT image series of the optic nerve head.**

## 5.4 Algorithm Validation

### 5.4.1 Assessment of the Segmentation Algorithm

Although several methods for automatic segmentation of OCT images of the posterior segment of the eye have been developed, only few can be directly applied to optic nerve head images such as the modified Canny filter [84] (MCF) and the Hierarchic approach [85] (HA). The two methods, proposed and developed by R. Koprowski and Z. Wrobel, were implemented and optimized in the same manner as the algorithm proposed in this thesis, in order to serve as comparison and validation. Both methods are briefly described in the following subsections.

#### 5.4.1.1 Modified Canny Filter

In this algorithm the input image is initially subjected to median filtering with a squared mask of 13 pixels width and the intensity is normalized. Next, Gaussian filtering in both directions with $\sigma_x = 0.2$ and $\sigma_y = 4$ is applied for noise reduction. Then, the first derivative of a Gaussian function is used to create two convolution masks to estimate the gradients in both directions (size 30x30 pixels, $\sigma_x = 0.2$ and size 50x50 pixels, $\sigma_y = 4$) and the resulting gradient image is thresholded with $T = 0.2 * (Imax - Imin) + Imin$, with $Imax$ and $Imin$, the maximum and minimum intensity values of the image being processed. Next, linear interpolation is used in a 3x3 neighborhood to find two pixels that straddle the gradient direction, the central pixel is then defined as an edge point if its gradient magnitude is greater than those of the interpolated points. Finally, the ILM is set as the first nonzero pixel per A-scan.

#### 5.4.1.2 Hierarchic Approach

Intensity normalization, median filtering with a 5x5 pixels mask, and image decomposition to a lower resolution, with a 16 pixel block using the median, constitute the preprocessing. Then, an auxiliary matrix that contains the intensity differences between adjacent pixels in each A-scan is calculated and employed to define two binary images. The first one contains only the pixels with the highest difference value per A-scan, while a threshold arbitrarily set at 0.03 is applied to the auxiliary matrix to generate the second binary image. These two images are used to identify the borders of the retina, and several constrictions must be fulfilled in order to correct erroneous recognition. The next steps consists on reducing the decomposition area by half in each iteration to increase accuracy (8x8, 4x4, 2x2); the positions of the layers determined in the previous iteration are connected with linear interpolation and individual point matching. As final steps, the layers are rescaled, a 5x5 pixels median filter is applied to remove points misallocated in shadowed areas, and interpolation gives the resulting segmented profile.

#### 5.4.1.3 Performance Evaluation

The three approaches were applied to 25 ONH OCT images randomly chosen from the data set, with Spectralis quality scores ($Q$) ranging from 11 to 35. In order to validate the proposed algorithm quantitatively, as there is no gold standard for ONH OCT images to compare with, five specialists were asked to delineate the ILM manually for the same set of images. Manual segmentation was performed using a tablet equipped with a stylus. For each image, the average manually segmented ILM was computed and used to compare the accuracy of every specialist and automated method. Absolute deviation from the mean trace for every A-scan of every image is shown in Fig. 5.10 as violin plots.

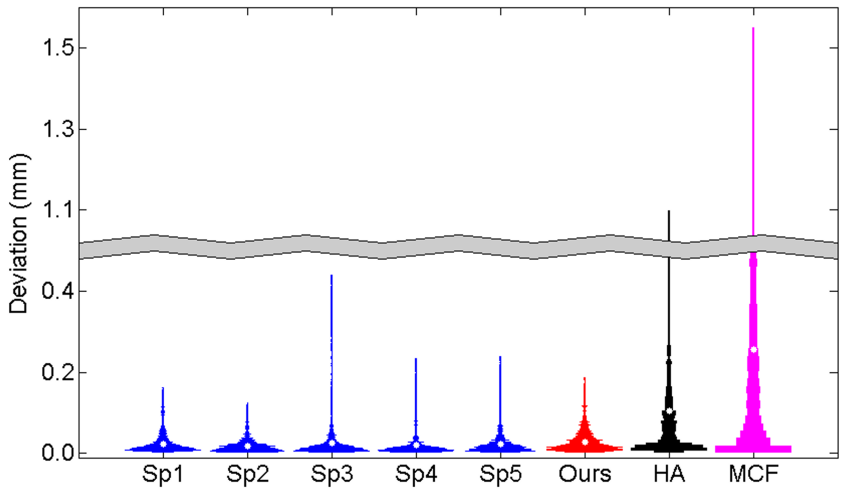


**Figure 5.10 – Quantitative evaluation of the proposed segmentation algorithm. A set of 25 ONH OCT images was manually segmented by five specialists (Sp1-Sp5) and the average ILM was used as gold standard for validation. The accuracy of the segmentation was evaluated by the absolute deviation from the gold standard of each A-scan for all images. The accuracy of the two methods used for comparison, the Modified Canny Filter (MCF) and the Hierarchic Approach (HA), as well as that of each one of the specialists was also evaluated. Results are presented as violin plots, where the white dot represents the mean value of each distribution.**

Our algorithm shows a variability comparable to that of the specialists', highlighting its robust performance on low quality images. On the other hand, MCF failed to segment the vitreal-retinal boundary due to high speckle content on the images. Notwithstanding HA showed a more robust performance to noise than MCF, its border detection was considerably affected by shadow effects that reduce visibility of some retinal regions. Although MCF and HA show good results for high quality images ($Q > 25$), where a significant contrast at the vitreal-retinal boundary is observed, its accuracy on low quality images is not always satisfactory. Fig. 5.11 shows some examples of the segmented results along with the original images.

The time of analysis, together with satisfactory results, is of crucial importance if we take into account that each series comprises hundreds of images. The average ILM segmentation time for MCF, HA and our algorithm is 9.4 s, 2.4 s and 0.40 s,

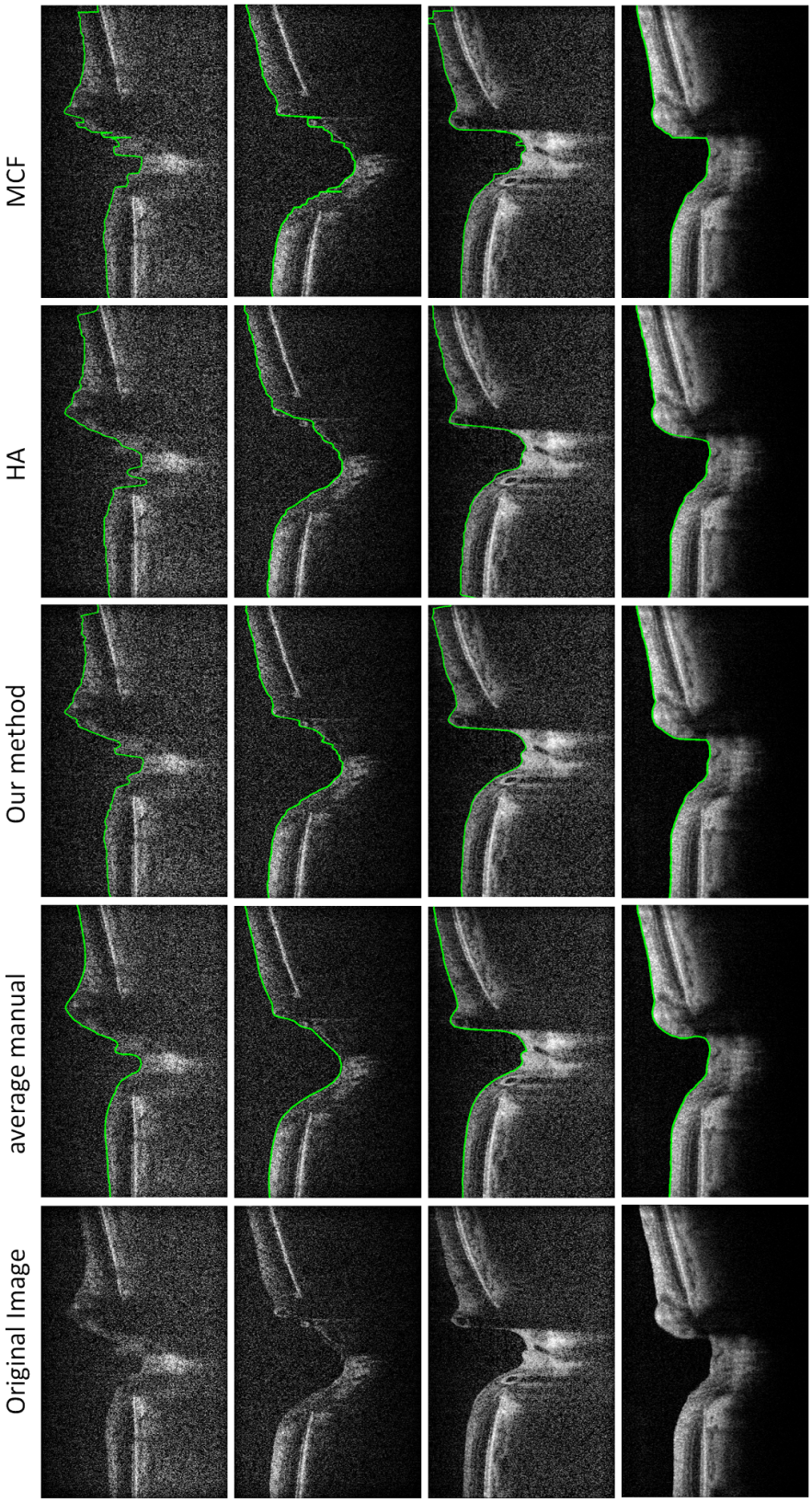


**Figure 5.11 – ILM automated segmentation results using different algorithms: a modified Canny filter (MCF), Hierarchic approach (HA), and the proposed method. The second column shows the average ILM manually segmented used as gold standard. Images shown have Spectralis quality scores of 11, 15, 18 and 30 $dB$ (top to bottom).**

respectively, calculated over a set of 100 images (496 x 768 pixels) analyzed in a PC (3.30 GHz Intel Core i3 processor, 4 GB of RAM).

### 5.4.2 Reproducibility of Deformation Measurements

The reproducibility of the method was assessed by measuring the N-PP retinal deformation repeatedly on eleven subjects randomly chosen from the ophthalmology clinic. Two image series were obtained per subject 10 minutes apart. Results are displayed in Figure 5.12.

An intraclass correlation coefficient (ICC) of 0.86 was obtained with confidence intervals [0.55,0.96] at $\alpha = 0.05$.

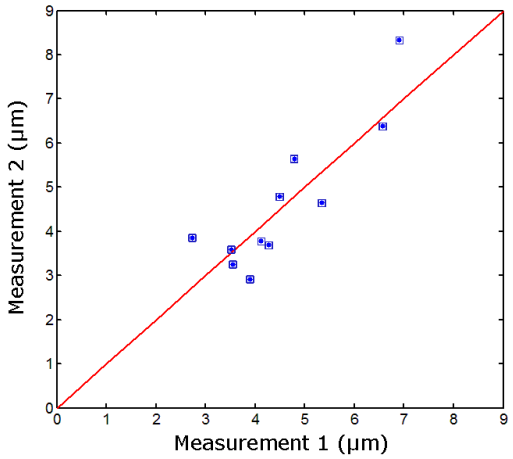


**Figure 5.12 – Neuro-peripapillary retinal deformation reproducibility results obtained from 11 subjects, ICC=0.86, CI [0.55,0.96],** $\alpha = 0.05$**.**

Once the performance and reproducibility of the analysis method has been tested and validated it can now be used to investigate the dynamics of the peripapillary retinal tissue as well as its clinical significance.

# Chapter 6

# Pulsatile Neuro-Peripapillary Retinal Deformation in Glaucoma

In order to investigate the relationship between neuroretinal deformation due to pulsatility and glaucoma insult, N-PP retinal deformation is characterized in four clinical cohorts that cover the most representative part of the glaucoma spectrum: ocular hypertensive, open-angle glaucoma suspect, early open-angle glaucoma, and healthy eyes, recruited from the Glaucoma Clinic of the Maisonneuve-Rosemont Hospital's Ophthalmology Department. Groups' definition and protocol description are detailed in Section 4.3.

## 6.1 Subjects

Eleven ocular hypertensive patients under medical therapy (OHT), 17 open-angle glaucoma suspects without glaucoma medication (OAG-S), 24 early open-angle glaucoma patients under medical therapy and no previous incisional glaucoma surgery (EOAG), and 18 healthy volunteers (no history of glaucoma) were included in the

study. Most normal subjects were consulting for early cataracts or were spouses of glaucoma patients. One eye was studied per patient.

## 6.2 Data Acquisition

Series of OCT line scans of the same region of the ONH were acquired at $20Hz$ for $20s$. Each series consists of 401 high resolution images acquired over a $15^{o}$ field of view ($5mm$ approx.). Two OCT image series are obtained per subject, at $45^{o}$ and $135^{o}$ with respect to the fovea to disc axis, corresponding to the areas of major insult in glaucoma. All eyes are transformed to right-eye format. The pulse trace of the subject was also recorded during the OCT imaging.

Additionally to the OCT image series, a full workup of the eye under examination was performed. The following parameters were measured and included in the analysis: intraocular pressure (IOP), ocular pulse amplitude (OPA), corneal hysteresis (CH), corneal resistance factor (CRF), central corneal thickness (CCT), axial length (AL), visual field mean defect (MD), mean arterial blood pressure (MAP), mean ocular perfusion pressure (MOPP), systolic perfusion pressure (SPP), diastolic perfusion pressure (DPP), mean peripapillary RNFL thickness and vertical C/D.

## 6.3 Data Analysis

The analysis of the OCT image series is performed using the algorithm described in Chapter 5. As a summary, a graphical description of the method is shown in Figure 6.1.

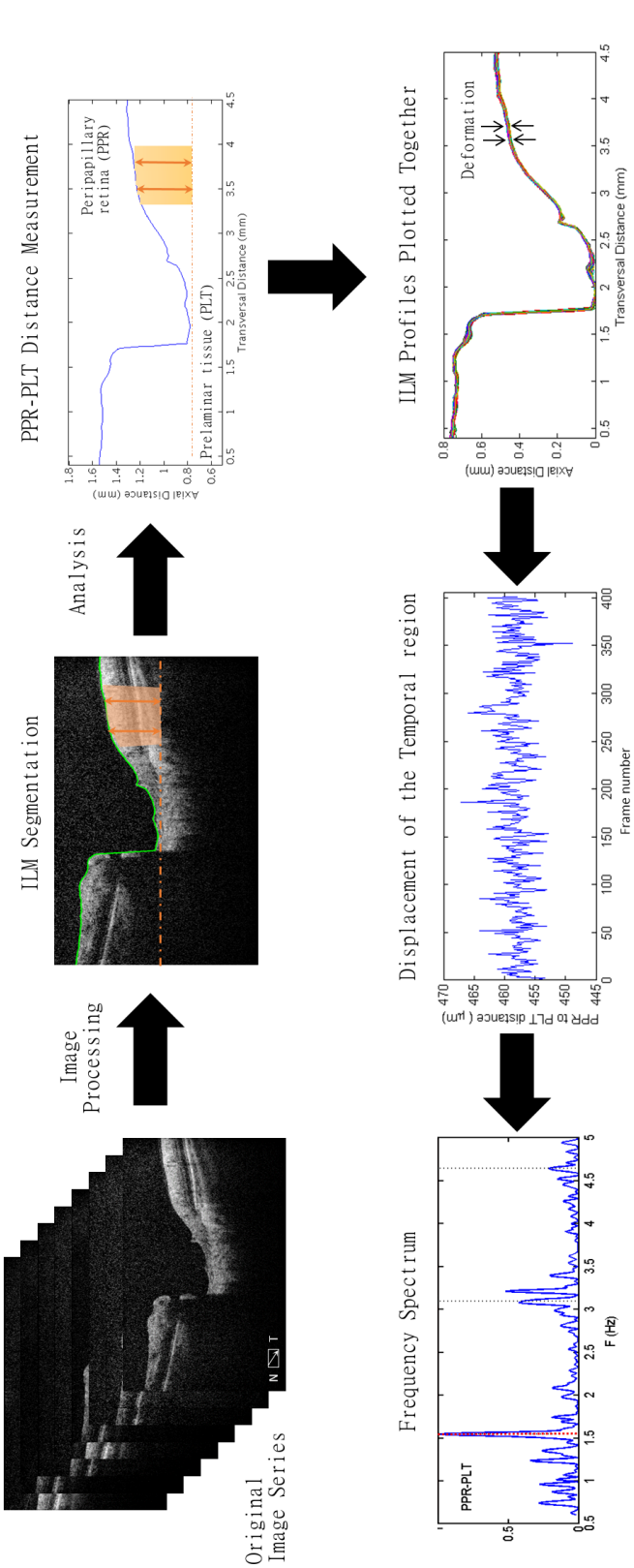


**Figure 6.1 – General description of the image analysis method. All images of the series are registered with a rigid transformation and the inner limiting membrane (ILM) is segmented on each one of the frames comprising the sequence. Next, the average distance between the temporal side of the peripapillary retina and the prelaminar tissue (PPR-PLT distance) is computed for each one of the profiles. Neuro-peripapillary retinal deformation is defined as the standard deviation of the PPR-PLT distances of all frames. Finally, to validate the result, the frequency spectrum of the PPR-PLT distances is calculated to corroborate that the heart frequency (red dotted line) is the main component of the measured retinal displacement.**

## 6.4 Results

Recorded image series were excluded due to fixation problems, poor quality images ($Q < 10dB$ for most of the images), large blood vessels governing the movement of the neuroretinal tissue and the inability to identify the heart frequency in the spectrum of the PPR-PLT distances. Despite the fact that 70 subjects gave valid results not all have successful measurements for both angles, consequently, group sizes may differ from one angle to another.

### 6.4.1 N-PP Retinal Deformation Comparison

Obtained results for the two investigated regions are displayed in Fig. 6.2 as box plots (filled boxes correspond to the superotemporal region or 135º). Analysis of variance (ANOVA) followed by Tukey's HSD post hoc test for multiple comparisons was used to compare the investigated parameters by diagnosis[1], $p$ values $< 0.05$ were considered statistically significant. Test were performed with the IBM SPSS Statistics 21 software.

At the Inferotemporal region, the Normal group had significantly higher deformation ($4.8 \pm 1\mu m$) than the OHT ($3.5 \pm 0.3\mu m$, $p = 0.015$), OAG-S ($3.8 \pm 0.8\mu m$, $p = 0.045$) and EOAG ($3.2 \pm 0.7\mu m$, $p < 0.001$) groups; OAG-S was also significantly different from the EOAG group ($p = 0.0375$) when comparison was performed se-parately. On the other hand, Superotemporal N-PP deformation does not show significant differences among the four groups ($p = 0.139$). This finding can be explained in part by the fact that the loss of neuroretinal rim starts most commonly at the inferotemporal region, being the most affected during the evolution of the glau-

[1]In order to corroborate our results, a non parametric version of ANOVA, the Kruskal-Wallis test, was also performed followed by the Hochberg's GT2 test for multiple comparisons (to be used when the sample sizes are very different), obtaining the same results.

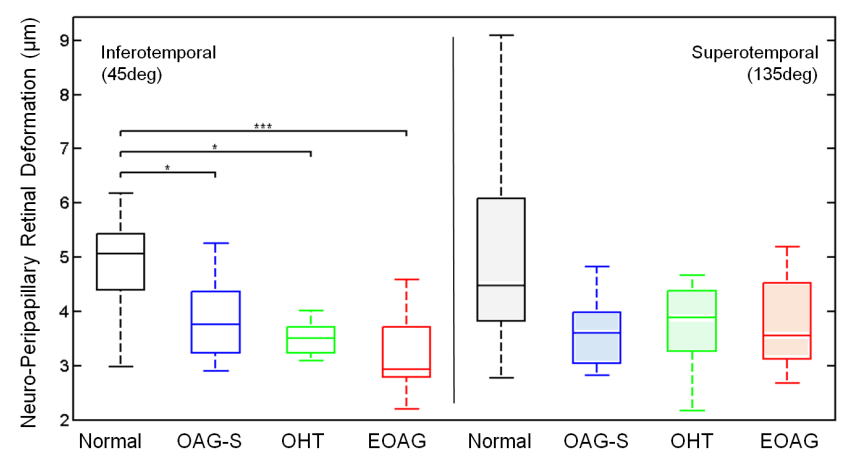


**Figure 6.2 – Comparison of N-PP retinal deformation values between the four cohorts under study for both investigated regions (OAG-S: open-angle glaucoma suspect, OHT: ocular hypertensive, EOAG: early OAG). Significant statistical differences are represented with the following criteria:** $*p < 0.05$**,** $**p < 0.01$ **and** $***p < 0.001$**.**

comatous neuropathy [32]. Table 6.1 contains the demographics by diagnosis as well as the mean deformation values for both regions.

It results interesting the fact that, when comparing the average deformation by region, in the Normal and the OAG-S groups the deformation of the Inferotemporal region is larger than that of the Superotemporal, resulting the opposite in the case of the OHT and EOAG groups (Fig. 6.3).

This could suggest that larger Inferotemporal deformation is actually beneficial to the axonal tissue and its reduction is part of the glaucoma progression, becoming even smaller than that of the Superotemporal region.

It is important to emphasize that the values reported here as deformation correspond to the standard deviation of all distances measured over the 401 frames that constitute the image series. Thus, even though deformation values fall in the range of 2-7$\mu m$, the actual range of the measured distances in a image series is between five and ten times larger.

**Table 6.1 – Mean Neuro-Peripapillary Retinal Deformation and Demographics by Diagnosis**[a]

| | Normal (n=18) | OAG Suspect (n=17) | OHT (n=11) | Early OAG (n=24) |
|---|---|---|---|---|
| Age (y.o.) | 71.0±7.8 (53-83) | 60.3±10.5 (45-78) | 55.9±13.6 (31-73) | 64.3±11.2 (44-90) |
| MAP ($mmHg$) | 96.5±9.0 (84.3-122) | 96.1±11.3 (74-114.7) | 100.5±9.8 (85.7-117) | 99.4±7.6 (81.6-113) |
| AL ($mm$) | 23.4±1.4 (20.1-25.2) | 23.6±1.2 (21.7-25.5) | 24.5±2.9 (21-32.2) | 24.2±1.6 (21.2-26.8) |
| IOP ($mmHg$) | 16.4±2.3 (13.8-21) | 18.5±3.4 (14.5-28.7) | 21.0±3.5 (15.6-29.6) | 18.4±3.2 (12.7-25) |
| OPA ($mmHg$) | 2.9±0.9 (1.3-4.5) | 3.3±1.3 (0.9-6.5) | 3.3±1.2 (0.9-4.6) | 3.3±1.3 (1.6-6.9) |
| MOPP ($mmHg$) | 54.0±7.3 (45.1-70.5) | 51.7±6.6 (38.8-65.2) | 53.0±6.2 (44.4-64.9) | 54.0±5.5 (41.6-62.2) |
| SPP ($mmHg$) | 118.9±17.4 (98.1-165.8) | 114.1±15.9 (94.2-159.1) | 118.6±14.7 (100-150) | 119.2±18.7 (89.8-169.3) |
| DPP ($mmHg$) | 62.1±10 (42.4-84) | 59.3±8.7 (40.2-75.7) | 59.9±7.9 (45.2-71) | 61.8±8.5 (40.7-74.9) |
| CH ($mmHg$) | 10.2±1.5 (7.6-12.8) | 9.8±1.0 (8.5-11.6) | 9.9±2.7 (7-16.1) | 9.3±1.5 (7.1-12.4) |
| CRF ($mmHg$) | 9.9±1.7 (7.6-12.7) | 10.3±1.8 (7.3-15) | 10.5±2.7 (7.2-17.3) | 9.8±1.7 (6.7-13) |
| CCT ($\mu m$) | 549.4±37.8 (498-623) | 541.2±28.8 (485-582) | 558.9±48.3 (498-636) | 531.5±34 (469-597) |
| MD ($dB$) | – – – – – – – | -0.33±1.84 (-4.36 - 1.78) | -1.47±1.59 (-3.92 - 1.6) | -1.6±1.53 (-4.82 - 0.49) |
| PSD ($dB$) | – – – – – – – | 1.81±0.66 (1.08-3.21) | 1.76±0.43 (1.1-2.47) | 2.58±1.28 (1.36-5.26) |
| Mean peripapillary RNFL ($\mu m$) | – – – – – – – | 89.6±11.2 (72-105) | 93.1±7.0 (82-100) | 74.8±12.02 (53-96) |
| Vertical C/D | – – – – – – – | 0.69±0.02 (0.66-0.74) | 0.53±0.13 (0.3-0.66) | 0.71±0.06 (0.59-0.78) |
| N-PP Def. Inferotemporal ($\mu m$) | 4.8±1.1 (3.0-6.2) | **3.8±0.8 (2.9-5.3)**$*$ | **3.5±0.3 (3.1-4.0)**$*$ | **3.2±0.7 (2.2-4.6)**$***$ |
| N-PP Def. Superotemporal ($\mu m$) | 4.6±1.5 (2.8-7.5) | 3.6±0.7 (2.8-4.8) | 4.1±0.5 (3.6-4.7) | 3.8±0.8 (2.7-7.5) |

[a]Data presented as mean±$S.D.$(range). Variables in bold are significantly different from the Normal group ($*p < 0.05, **p < 0.01, ***p < 0.001$).

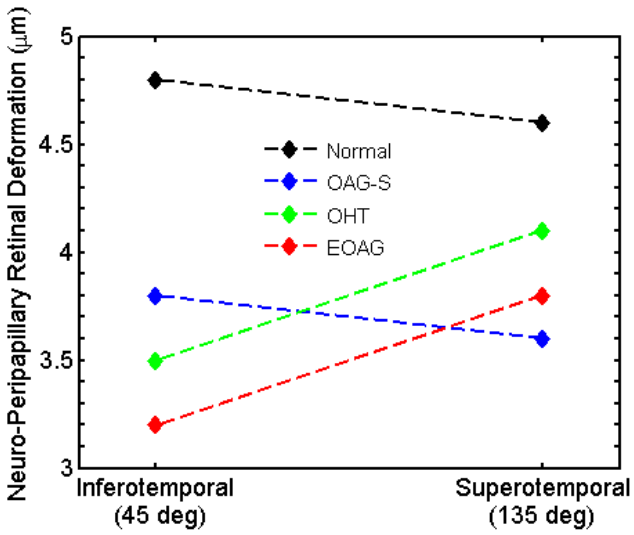


**Figure 6.3 – Average N-PP retinal deformation by group: comparison between inferotemporal and superotemporal regions.**

Intergroup comparisons of the variables under study showed that the Normal group has higher mean age compared to the OAG-S group ($p = 0.041$). However when performing the comparisons controlling for age, the covariate is not significant ($p = 0.235$) and we can conclude that the age has no effect on the differences found in N-PP retinal deformation by diagnosis.

So far we have shown that differences in N-PP retinal deformation of the Inferotemporal region exist between diagnosis groups, but it is also important to understand how such deformation is related to the other ocular, vascular and demographic parameters that were included in the analysis. In order to do so, Pearson correlation was performed as well as multiple linear regression analysis using the stepwise method with a linear model with interactions and squared terms as upper model. Each cohort was analyzed separately. In all cases $p < 0.05$ was considered statistically significant.

### 6.4.2 Normal Group

In this case the linear correlation analysis showed that eyes with thinner corneas tend to have larger Superotemporal deformation than thicker ones ($r = -0.62, p = 0.045$) as can be seen in Figure 6.4. No significant relationships were found for the Inferotemporal region or the multivariate analysis.

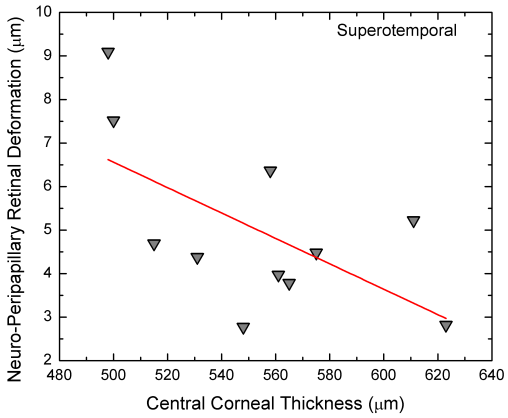


**Figure 6.4 – Linear regression for Superotemporal N-PP deformation vs CCT in healthy eyes ($R^2 = 0.3063$.)**

### 6.4.3 OAG Suspects

In the OAG Suspect group, lower corneal hysteresis (Fig. 6.5a) and thicker peripapillary RNFL's (Fig. 6.5b) were related to larger Inferotemporal deformation ($r = -0.66, p = 0.036; r = 0.95, p = 0.004$). On the other hand, Superotemporal deformation tend to increase with DPP ($r = 0.69, p = 0.027$) (Fig. 6.5c).

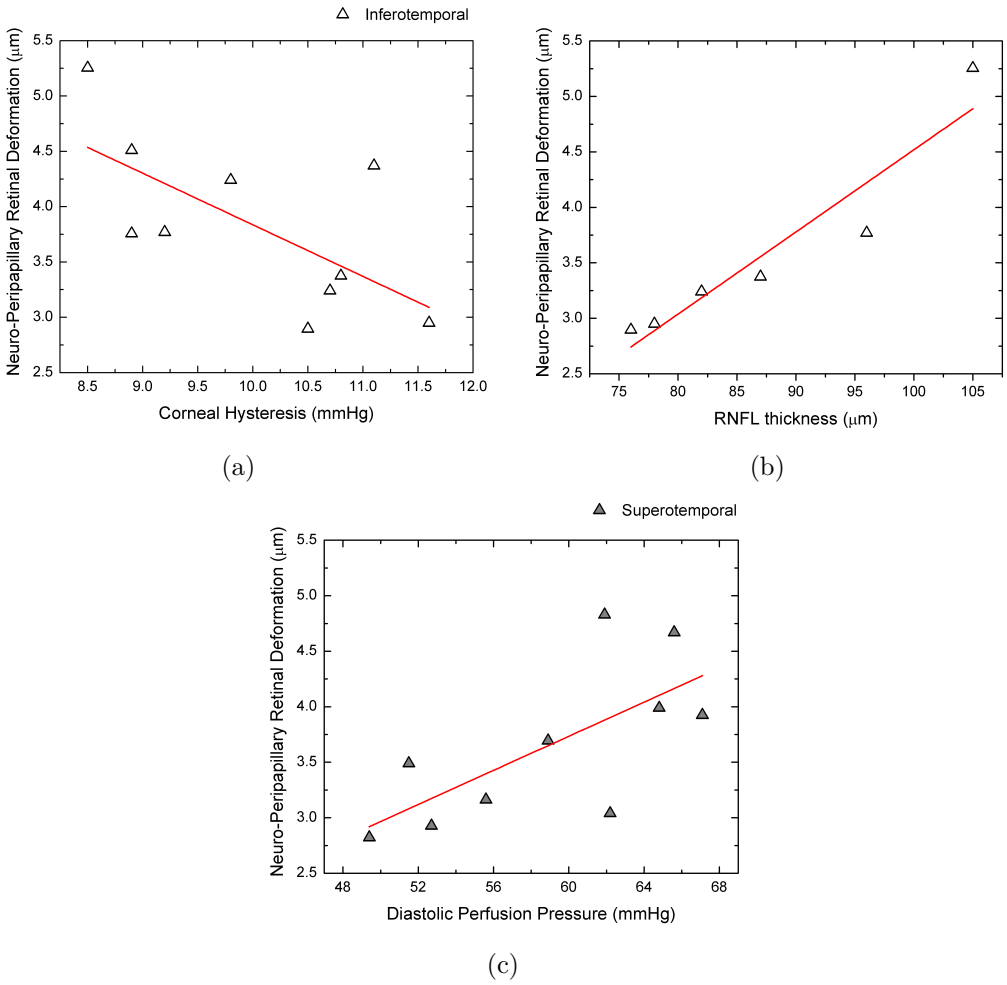


**Figure 6.5 – Linear regression analysis for the OAG-S group: a) Inferotemporal deformation vs CH ($R^2 = 0.372$); b) Inferotemporal deformation vs mean peripapillary retinal nerve fiber layer thickness around the ONH ($R^2 = 0.870$); c) Superotemporal deformation vs DPP ($R^2 = 0.412$).**

### 6.4.4 OHT

For the Inferotemporal region, greater OPA amplitudes as well as less negative MD (more normal) were correlated with larger N-PP deformation ($r = 0.855, p = 0.030; r = 0.921, p = 0.009$). The vertical cup to disc ratio showed a borderline significance, where less Inferotemporal deformation was related to greater glaucoma severity ($r = -0.805, p = 0.053$).

Eyes with small CRF values were associated with greater Superotemporal deformation ($r = -0.984, p = 0.002$). The corresponding graphs are shown in Figure 6.6.

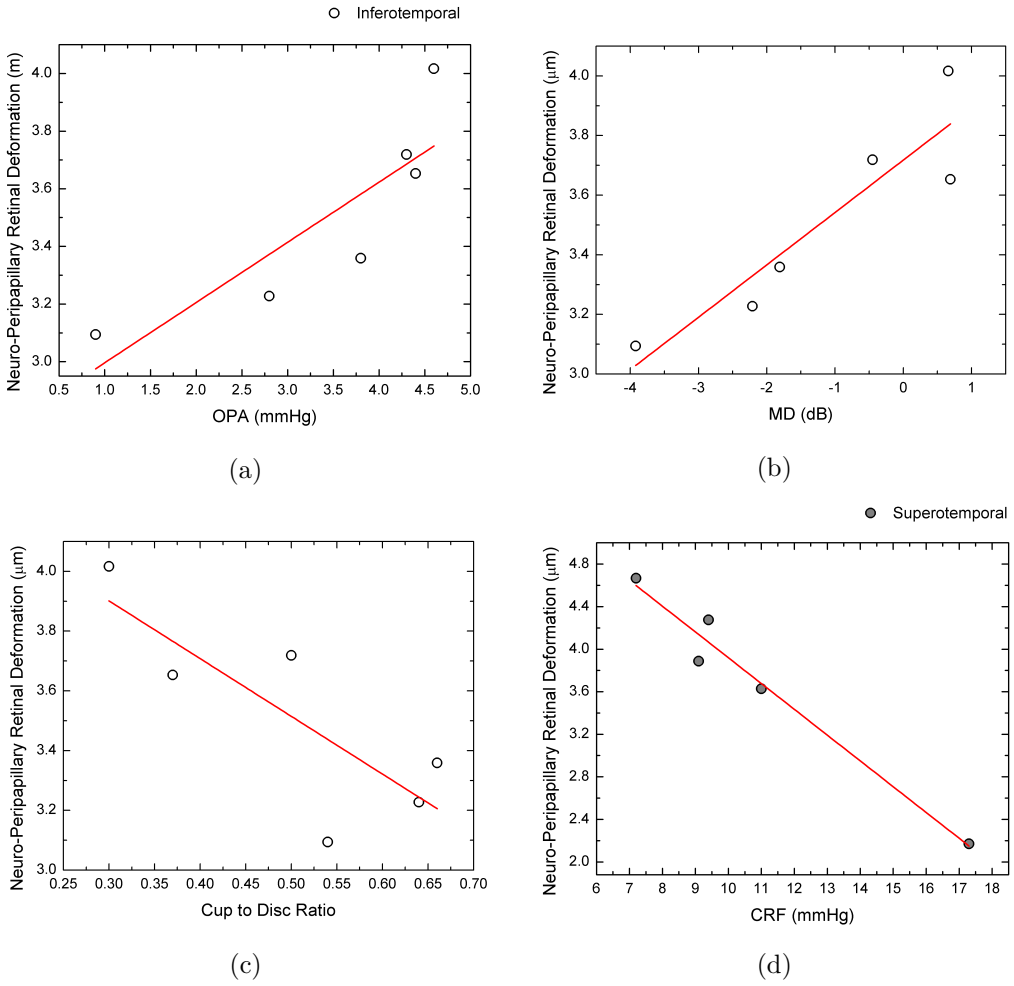


**Figure 6.6 – Linear regression analysis for the OHT group: a) Inferotemporal deformation vs ocular pulse amplitude ($R^2 = 0.664$); b) Inferotemporal deformation vs visual field mean defect ($R^2 = 0.810$); c) Inferotemporal deformation vs vertical C/D ($R^2 = 0.561$) and d) Superotemporal deformation vs corneal resistance factor ($R^2 = 0.960$).**

When multiple linear regression analysis was performed, only one predictor was found statistically significant for each region:

$$N - PP_{InferoT} = 3.7176 + 0.17568MD, \tag{6.1}$$

$$N - PP_{SuperoT} = 6.3433 - 0.24237CRF, \tag{6.2}$$

explaining the 81% ($p = 0.0092$) and the 96% ($p = 0.0025$) of the variance in deformation of each region, respectively.

### 6.4.5 Early OAG

In the early glaucoma group, greater Inferotemporal deformation was associated with thinner corneas ($r = -0.54, p = 0.046$, Fig. 6.7a), while larger Superotemporal deformation was correlated with lower DPPs ($r = -0.564, p = 0.018$, Fig. 6.7b), bigger ocular pulse amplitudes ($r = 0.53, p = 0.028$, Fig. 6.7c) and larger IOP values ($r = 0.49, p = 0.045$, Fig. 6.7d).

In this case, the multiple regression analysis resulted in a model for the Inferotemporal N-PP retinal deformation with two predictors. Despite the fact that CCT showed a significant correlation, only IOP and SPP had significant partial effects in the full model

$$N - PP_{InferoT} = 4.8371 - 0.21339IOP + 0.019232SPP. \tag{6.3}$$

The two predictor model described by Eq.(6.3) and depicted in Figure 6.8a, was able to account for the 76.7% of the variance in deformation ($p = 0.0007$).

Figure 6.8b illustrates the relationship between IOP, SPP and Inferotemporal N-PP retinal deformation in the EOAG group.

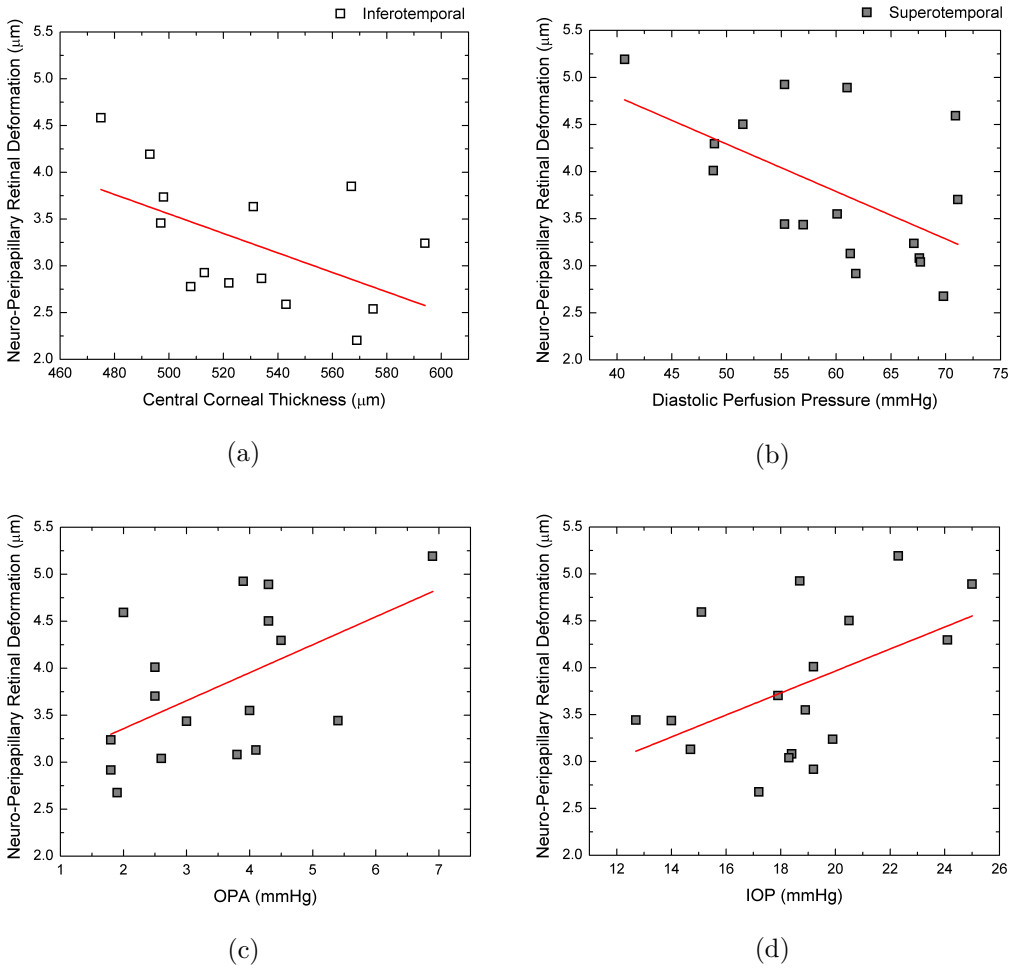


**Figure 6.7 – Linear regression analysis for the EOAG group: a) Inferotemporal deformation vs CCT ($R^2 = 0.233$); b) Superotemporal deformation vs DPP ($R^2 = 0.272$); c) Superotemporal deformation vs ocular pulse amplitude ($R^2 = 0.234$) and d) Superotemporal deformation vs intraocular pressure ($R^2 = 0.192$).**

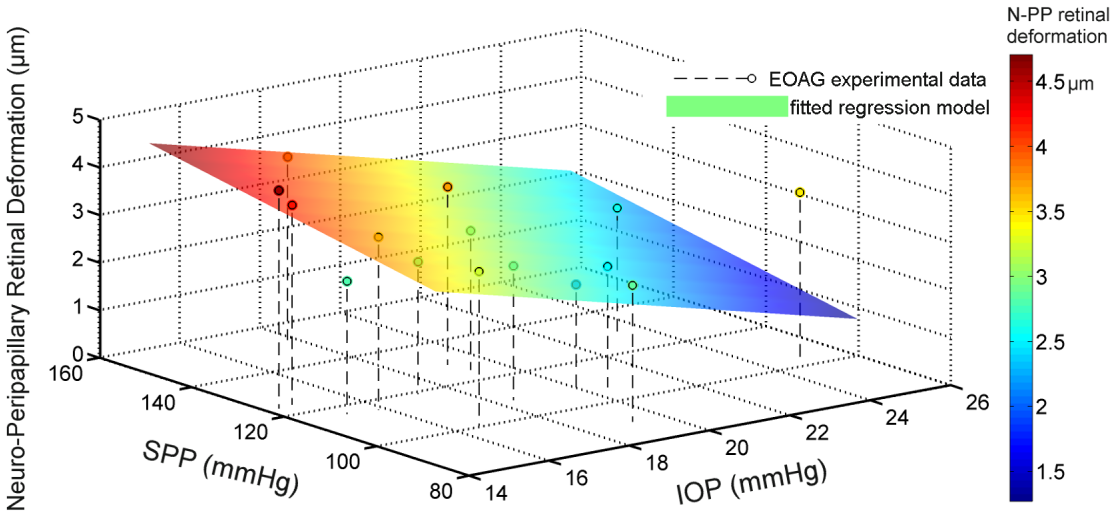


(a)

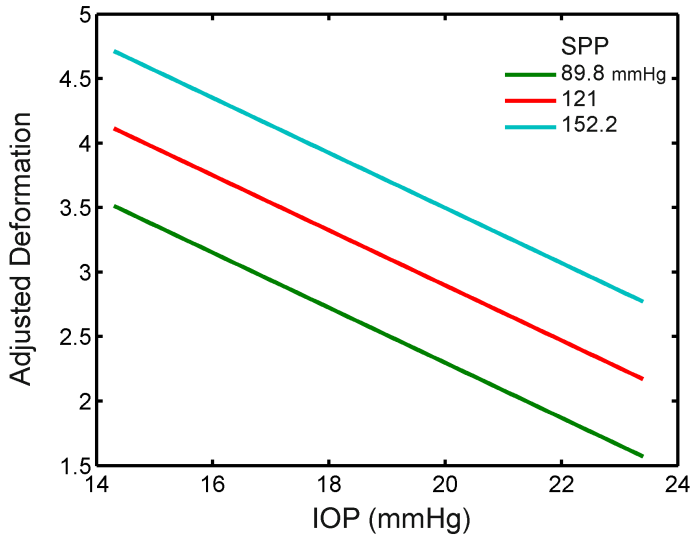


(b)

**Figure 6.8 – Fitted linear model for EOAG Inferotemporal neuro-peripapillary retinal deformation with IOP ($\beta = -0.21339, p = 0.0006$) and SPP ($\beta = 0.019232, p = 0.0194$) as predictors ($R^2 = 0.767, p < 0.001$). a) Experimental data (colored dots) and fitted regression plane corresponding to Eq.(6.3). The color bar indicates the mapping of deformation values that ranges from $1.25\mu m$ (dark blue) to $4.75\mu m$ (dark red). b) Interaction plot between IOP, SPP and N-PP retinal deformation according to the model. The graph shows that the amount of Inferotemporal N-PP retinal deformation diminishes with both, low SPP and high IOP, two major risk factors in glaucoma.**

Regarding the Superotemporal deformation, it was found that diastolic perfusion pressure was the only independent variable affecting significantly the N-PP retinal deformation ($R^2 = 0.272, p = 0.004$) in the multivariate model:

$$N - PP_{SuperoT} = 6.3433 - 0.0504DPP. \tag{6.4}$$

#### 6.4.5.1 Follow Up

From the 24 patients in the EOAG group, only four of them agreed to be tested a second occasion in a different date. Again, not all patients had valid results for both investigated angles and the time between visits varies among the four individuals. Although the number of patients is quite small, this data is presented aiming to illustrate the evolution and complexity of the investigated deformation. The full data is contained in Table 6.2. Figure 6.9 shows, graphically, the data obtained in both visits for the principal parameters identified in the multivariate analysis as well as the deformation values.

Two patients had inferotemporal N-PP deformation results in both visits (2 and 3), both had a considerable decrease in IOP as well as a significant increase in SPP in the second visit, which according to Eq.(6.3) should result in larger N-PP deformation. However, as can be seen in Figure 6.9e this happens only in the case of *patient 3* while *patient 2* shows the opposite behavior. Among the factors that could be influencing such result we have that *patient 2* shows no change in OPA but there was a progression of visual field loss. To this we have to add the fact that *patient 3* shows very low CH: $6.4mmHg$, when mean CH in OAG eyes ranges from 7.2 to $11mmHg$ [86], [87], and lower CH values have been related to greater topographic ONH changes induced by acute pressure reduction in glaucomatous eyes [88].

**Table 6.2** – Early OAG follow up

| | Patient 1 | | Patient 2 | | Patient 3 | | Patient 4 | |
|---|---|---|---|---|---|---|---|---|
| Visit | 1 | 2 | 1 | 2 | 1 | 2 | 1 | 2 |
| MAP ($mmHg$) | 113.33 | 114.67 | 83.00 | 97.00 | 100.33 | 102.33 | 102.00 | 94.00 |
| IOP ($mmHg$) | 17.90 | 18.50 | 20.50 | 14.70 | 25.00 | 16.90 | 19.20 | 20.10 |
| OPA ($mmHg$) | 4.50 | 5.70 | 4.10 | 4.10 | 4.30 | 2.40 | 1.80 | 2.10 |
| MOPP ($mmHg$) | 57.66 | 57.94 | 34.83 | 49.97 | 41.89 | 51.32 | 48.80 | 42.57 |
| SPP ($mmHg$) | 140.10 | 153.50 | 94.50 | 124.30 | 104.00 | 124.10 | 124.80 | 113.90 |
| DPP ($mmHg$) | 73.10 | 67.50 | 46.50 | 61.30 | 61.00 | 66.10 | 61.80 | 53.90 |
| CH ($mmHg$) | 11.60 | 10.80 | 10.70 | 9.10 | 6.40 | 6.00 | 7.50 | 8.00 |
| CRF ($mmHg$) | 11.60 | 11.80 | 10.90 | 9.60 | 7.00 | 6.90 | 8.40 | 9.00 |
| MD ($dB$) | $-2.42$ | $-2.42$ | $-1.44$ | $-2.15$ | $-0.49$ | $-0.80$ | $-3.59$ | $-3.59$ |
| PSD ($dB$) | 1.59 | 1.59 | 1.92 | 1.98 | 2.54 | 2.77 | 5.26 | 5.26 |
| N-PP Def. Inferotemporal ($\mu m$) | 2.52 | - - - | 4.69 | 4.19 | 3.46 | 4.09 | 2.93 | - - - |
| N-PP Def. Superotemporal ($\mu m$) | 2.69 | 2.85 | - - - | 3.13 | 4.89 | 5.44 | 2.92 | 2.18 |
| Time between visits (months) | 4 | | 31 | | 42 | | 45 | |

Patients 1 and 2 were not receiving glaucoma medication in visit 1.

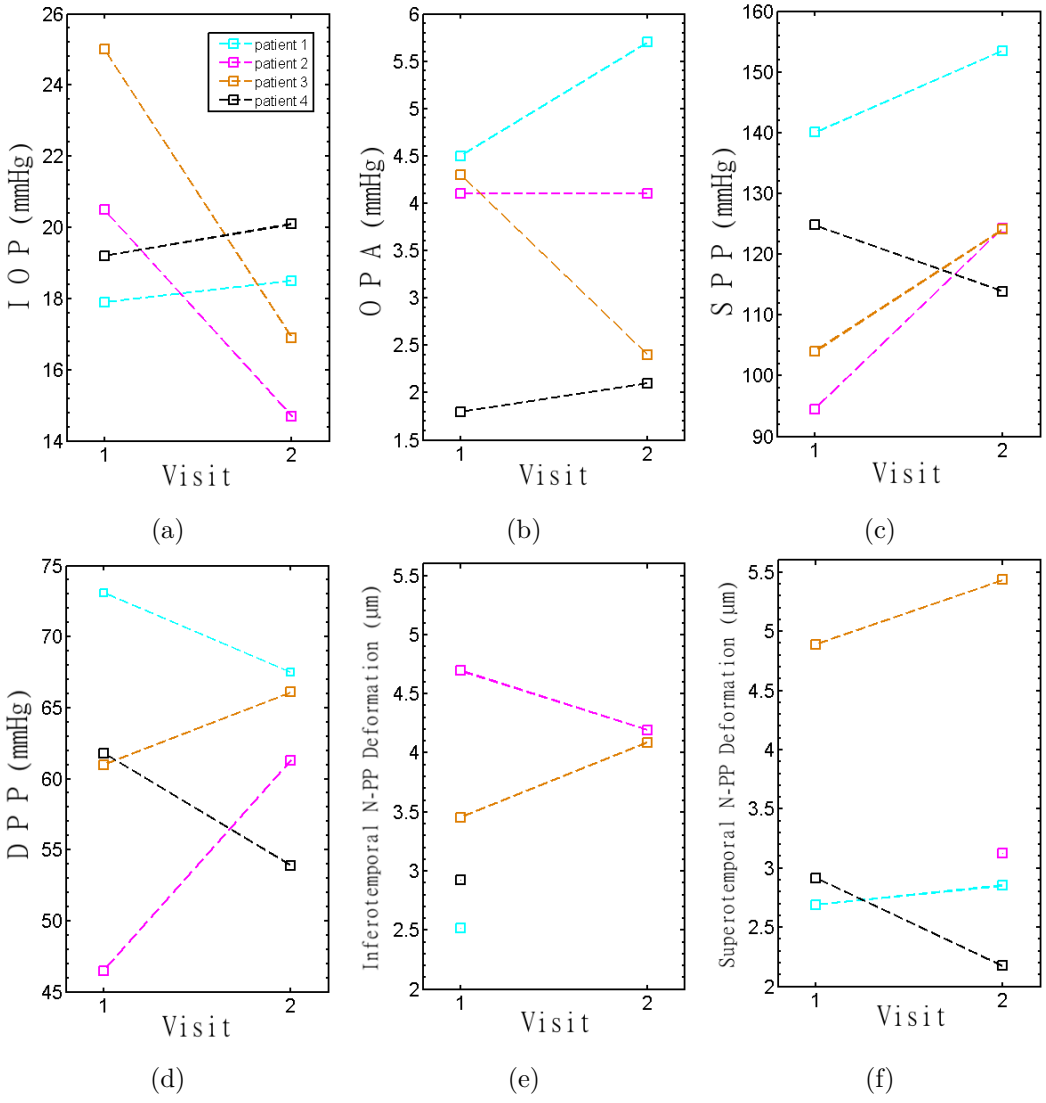


**Figure 6.9 – Evolution of the principal parameters related to N-PP retinal deformation for four EOAG patients in two visits. a) Intraocular pressure, b) ocular pulse amplitude, c) systolic perfusion pressure, d) diastolic perfusion pressure, e) Inferotemporal neuro-peripapillary retinal deformation, f) Superotemporal N-PP retinal deformation. Each color represents a patient, time between visits varies (see Table 6.2).**

## 6.5 Discussion

The obtained results show that healthy eyes have larger displacement of the peripapillary retina compared with the other groups. Three measures of glaucoma severity were investigated: mean peripapillary RNFL thickness, vertical cup to disc ratio, as determined by OCT, and visual field mean defect. When there were significant correlations, these parameters showed less Inferotemporal N-PP retinal deformation with greater glaucoma severity. The C/D showed borderline significance tending in the same direction, with larger ratios being associated with less deformation in the OHT and EOAG groups. This finding is consistent with our observation of smaller pulsatile N-PP retinal deformation in diseased eyes (OAG-S,OHT and EOAG) than in normal eyes. Furthermore, N-PP deformation of the Inferotemporal region was smaller than that of the Superotemporal in OHT and EOAG patients, since the opposite behavior was observed in healthy and OAG-S eyes, this finding suggests that larger Inferotemporal deformation might be normal and its reduction, a consequence of glaucoma progression.

Greater N-PP retinal deformation was observed in eyes with thinner corneas in the EOAG group. Consistently with this finding, greater reversal of cupping following long-term IOP reduction has been observed in eyes with thinner corneas where it was hypothesized that a thinner cornea might be associated with a more mobile lamina cribrosa [60].

It is interesting to note that while the mean IOP of the OHTs is higher than that of the normal group ($p = 0.008$) there was no significant difference in OPA between the 4 cohorts, and only in the OHT and EOAG groups a direct relation with N-PP retinal deformation was found. Although in both cases eyes with bigger OPA showed larger retinal displacement, this tendency reached significance at the Inferotemporal region for the OHT cohort and at the Superotemporal region in the case of the EOAG.

Since the Inferotemporal region is the most damaged area during the evolution of the disease, we can speculate that in the case of the EOAG group the mechanical response of the Superotemporal peripapillary retina is still similar to that shown by a normal ONH and this could be the reason why even though both groups show the same behavior it was localized in different regions.

Since OPA is driven by the choroidal pulse, the positive correlations found suggests that the observed deformations are also driven by choroidal pulsatility and the resultant pulsatile IOP fluctuations, as we would have expected.

It is well known that more rigid eyes yield larger changes in IOP when pulsatile blood flow increases the ocular volume. In accordance with this fact in this work it was found that hypertensive eyes with more rigid corneas (smaller CRF values) show larger Superotemporal deformation. The working hypothesis is that the magnitude of observed pulsatile N-PP retinal deformation depends on the magnitude of the pulsatile choroidal volume change, the elasticity of the load-bearing tissues of the ONH and the peripapillary retina, and the elasticity of tissues anterior to the peripapillary retina such as the cornea or anterior sclera, which can share in absorbing the impact of pulsatile choroidal volume change.

Several studies have shown that low OPP is a risk factor for the prevalence, incidence and progression of glaucoma [89]-[92]. Furthermore, it has been demonstrated that lower DPP is an independent risk factor for OAG and that individuals with DPPs below $30mmHg$ showed six times higher risk of developing glaucoma than those with DPP $> 50mmHg$ [93]. In this study, the Early OAG group showed higher Superotemporal deformation with decreased DPP. It is unclear from our data whether this correlation is due to greater choroidal pulsatility at low DPP or from greater tissue response to the pulse. The opposite relationship was seen in the OAG-S group, suggesting that this aspect of ocular physiology might evolve with the development of glaucoma.

While IOP continues to be a major predictor of glaucoma progression, the Early Manifest Glaucoma Trial found that lower systolic perfusion pressure is also an important predictor of progression in patients with both, lower and higher baseline IOP, suggesting almost a 50% increase risk [94]. Accordingly, the multivariate fitted model that best predicted the magnitude of the pulsatile Inferotemporal N-PP retinal deformation in the EOAG group has these two variables as the only significant predictors. The model suggests that an increase in IOP as well as a low SPP contribute to reduce the neuro-peripapillary retinal deformation in diseased eyes. This finding may have important implications in pathophysiology, and may help validate the use of N-PP retinal deformation as discriminator between healthy and diseased eyes, with the potential to be used as a new biomechanical descriptor of the eye.

Corneal hysteresis is a biomechanical property that refers to the ability of the ocular connective tissues to dampen pressure changes and has been associated with ONH morphology and damage in glaucoma [95],[96]. It has been recently found that eyes with low CH had greater ONH topographic changes following acute pharmacological IOP reduction [88], and significantly greater decrease in axial length after trabeculectomy-induced IOP lowering [97], supporting the hypothesis that CH is related to the material properties of the entire eye wall. Moreover, low CH has also been associated with low IOP in healthy eyes [98]. These results are coherent with our finding of greater deformation in eyes with lower CH in the OAG-S group. The reason for which this relation is not present in the OHT and EOAG groups could be attributed to the fact that tissue viscoelastic properties change in eyes exposed to chronic elevations in IOP [99]. Furthermore, all the OHTs and 80% of the EOAG group in this study are treated with prostaglandin agents (PA). It has been found that a continuous use of PA lead to a decrease in CCT [100], [101], and given their capacity to remodel the extracellular matrix [102] it has also proved to have a significant effect in CH [103], [104].

In summary, this study reveals that the actual mechanical response of the peripapillary retinal tissue to pulsatility is different between healthy and diseased eyes, being significantly larger in the first group. The measured deformation correlated with several risk factors for the glaucomatous optic neuropathy, but these correlations varied depending on the diagnosis. From all variables, CCT, OPA and DPP were found to be related with N-PP retinal deformation for more than one cohort. All these findings suggests that the measurement of pulsatile neuro-peripapillary retinal deformation should be further investigated to demonstrate its role in the pathogenesis of glaucoma. Part of this clinical study was published in [105].

# Chapter 7

# Pulsatile Perifoveal Retinal Deformation in Glaucoma

As mentioned before, a noninvasive method to measure ocular rigidity (OR) in vivo was developed simultaneously to this doctoral research, and a cross sectional study to investigate OR in glaucoma was started, providing a database with additional parameters such as mean macular choroidal thickness (CT) and ocular volume change ($\Delta V$). Considering that the elasticity of the sclera has been suggested as the most important determinant of the ONH stress and strain, a measurement of ocular rigidity would be useful to help understand how this parameter, choroidal pulsatility and pulsatile retinal deformation interact and are transduced into axonal death.

One of the particularities of the segmentation algorithm developed in this work is that it can be applied directly to macular OCT images to delineate the ILM without any modification. Taking advantage of this feature, a preliminary study to investigate retinal deformation around the macula was performed in the rigidity study patients, using the set of images previously acquired and incorporating the resulted parameters to the analysis.

## 7.1 Subjects

Eleven open-angle glaucoma patients under medical therapy and no previous incisional glaucoma surgery (OAG), 22 early open-angle glaucoma under medical therapy and no previous incisional glaucoma surgery (EOAG) and 34 healthy subjects with no history of glaucoma were analyzed. One eye was studied per patient.

## 7.2 Data Acquisition

The protocol followed here is similar to the one described in Section 4.3.3, with the difference relying in the OCT imaging. Since these image series are used to measure changes in choroidal thickness, the scanning line is now centered at the macula (see Fig. 7.1a). In this case the scans are acquired at $8Hz$ (high speed mode) for $50s$ using enhanced depth imaging (EDI) and the scanning angle is chosen to maximize the visibility of the choroid for each subject. Each series consists of 401 images (5 B-scans averaged per image) acquired over a $30^{o}$ field of view which corresponds to $\approx 8mm$ (Fig. 7.1b). All eyes are transformed to right-eye format. The pulse trace of the subject was recorded during the OCT imaging.

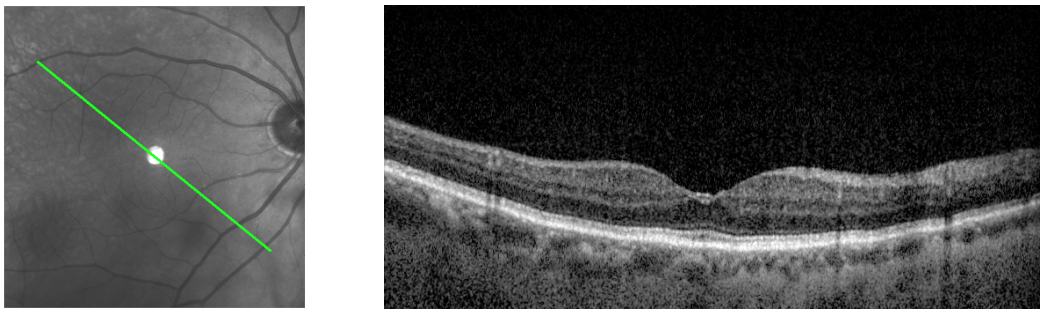

(a) (b)

**Figure 7.1 – Typical pair of images used to determine ocular rigidity and retinal deformation around the macula. a) Fundus image of a right eye showing the scanned line through the macula, in this case at $141^{o}$ with respect to the fovea to disc axis. b) Corresponding optical coherence tomography image with five averaged frames.**

Immediately after imaging the following parameters were measured and included in the analysis: IOP, OPA, CH, CRF, CCT, AL, MD, MAP, MOPP, SPP, DPP, CT, $\Delta V$[1] and OR.

## 7.3 Data Analysis

In this case, instead of using the deepest point of the cup in the optic nerve head, the center of the umbo is employed as reference to measure the axial distance. A region of 600$\mu$m located at the perifovea was selected at each side of the fovea to measure retinal displacement in time (see Fig. 7.2). The same analysis procedure described in Section 5.3 was followed to determine Perifoveal Retinal (PFR) deformation. Spectral analysis was performed to the retinal displacement measured in time to verify that the measured deformation is mainly caused by choroidal pulsatility. Figure 7.3 shows a graphical representation of the analysis method.

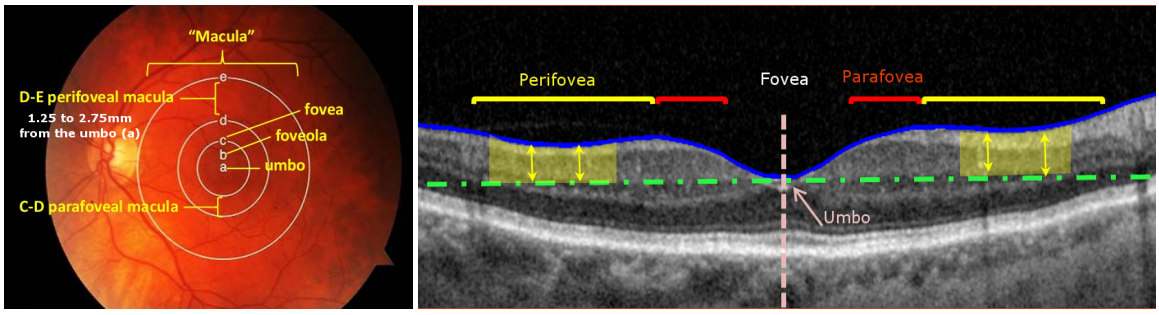


(a) (b)

**Figure 7.2 – Measurement of the perifoveal retinal displacement: a) Regions of the macula. b) The average axial distance between the perifoveal retina and the reference located at the center of the umbo (green line) is computed at both sides of the fovea to determine deformation. ((a) modified from https://image.slidesharecdn.com/ermvmt-161115153401/95/)**

[1]Ocular volume change is derived from the pulsatile choroidal thickness change using a first order approximation of a spherical eye model: $\Delta V = \pi R^2 \Delta CT$, where $R$ is half the axial length distance. For more details on the measurement and computing of the CT, $\Delta V$ and OR parameters see Ref [72].

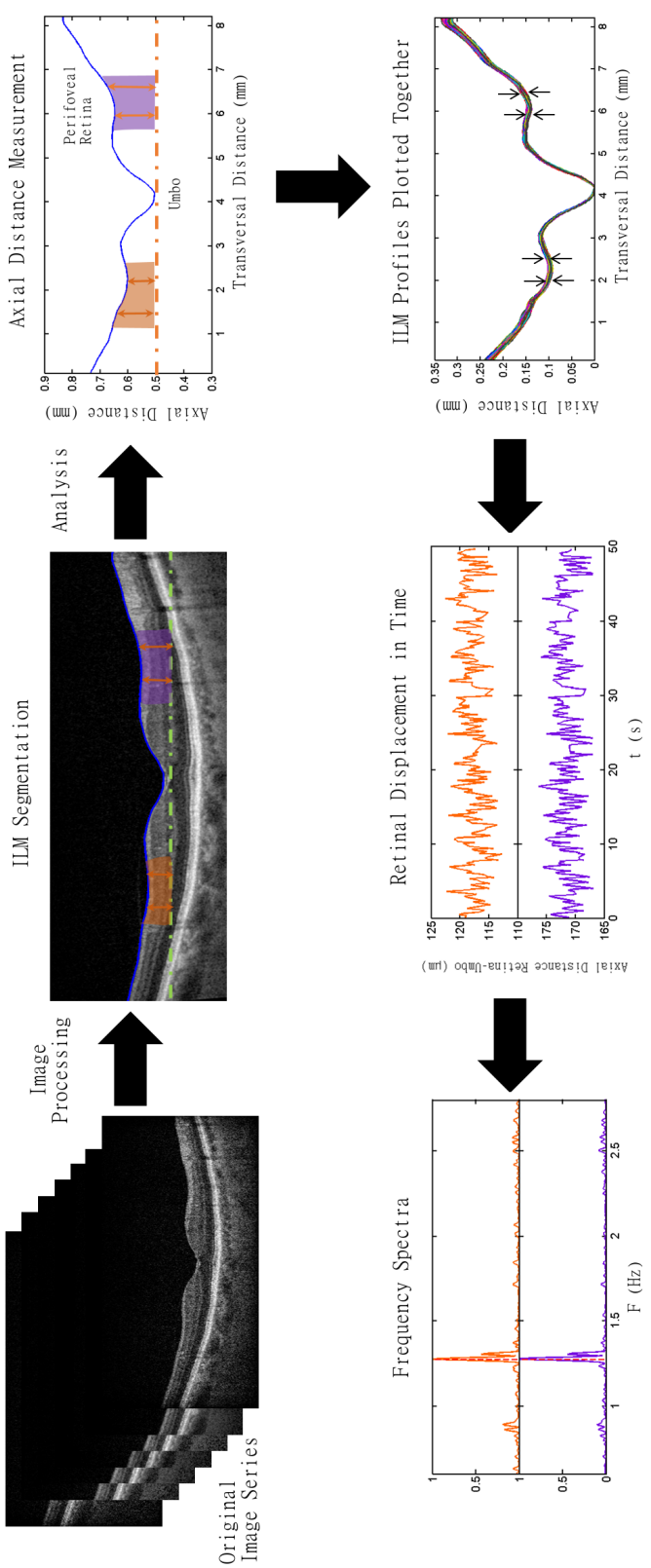


**Figure 7.3 – General description of the image analysis method used to measure retinal deformation around the macula. All images of the series are registered with a rigid transformation and the inner limiting membrane (ILM) is segmented on each one of the frames comprising the sequence. Next, the average axial distance between the perifoveal retina and the reference located at the center of the umbo is computed at both sides of the fovea for each one of the profiles. Retinal deformation on each region is defined as the standard deviation of the measured distances of all frames. Finally, to validate the result, the frequency spectra of the retinal displacement of each side in time is calculated to corroborate that the heart frequency (red dotted line) is the main component of the measured deformation.**

## 7.4 Results

Only image series with ocular rigidity results were analyzed, deformation results were rejected due to wrong ILM delineation in the majority of the images of the series or the inability to identify the heart frequency in the spectrum of the retinal displacement. Since the displacement of the retina in each side of the fovea showed a very similar behavior and there was no difference between both perifoveal retinal deformation values, results presented in the following correspond to the average value of the two investigated regions.

### 7.4.1 PFR Deformation Comparison

Obtained results for the three groups under investigation are presented in Figure 7.4 as boxplots. Analysis of variance (ANOVA) followed by Tukey's HSD post-hoc test for multiple comparisons was applied to all variables investigated by diagnosis, $p$ values $< 0.05$ were considered statistically significant.

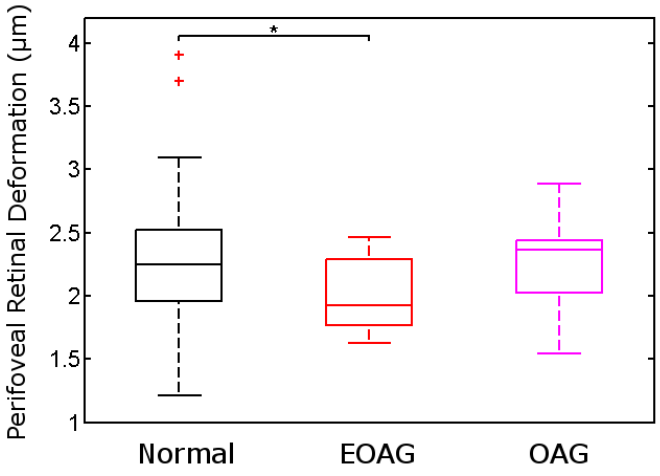


**Figure 7.4 – Perifoveal retinal deformation comparison between the three cohorts under study (EOAG: early open-angle glaucoma, OAG: open-angle glaucoma). The only significant difference was found between Normal and EOAG eyes ($p = 0.039$); Normal - OAG ($p = 0.948$), EOAG - OAG ($p = 0.268$).**

**Table 7.1 – Mean Perifoveal Retinal Deformation and Demographics by Diagnosis[a].**

| | Normal (n=34) | EOAG (n=22) | OAG (n=11) |
|---|---|---|---|
| Age (y.o) | 62.85±15.6 (27-84) | 65.77±13.0 (31-91) | 66.18±10.4 (48-84) |
| MAP ($mmHg$) | 93.8±9.0 (76-116) | 98.4±11.5 (77.3-120.7) | 95.3±6.8 (84-107.3) |
| AL ($mm$) | 24.0±1.4 (21.8-28.3) | 24.9±1.8 (22.6-30.6) | 24.1±0.96 (22.3-25.7) |
| IOP ($mmHg$) | 16.5±2.4 (11.8-23.9) | **19.2±3.6 (14-29.2)**$**$ | 18.9±5.6 (13.6-29.9) |
| OPA ($mmHg$) | 3.0±1.2 (1.5-6.9) | 2.9±0.7 (1.9-4.8) | 3.4±1.2 (1.2-5.7) |
| MOPP ($mmHg$) | 45.7±5.4 (31.5-58.5) | 46.5±8.6 (30.7-59.5) | 44.6±7.8 (32.9-53.6) |
| SPP ($mmHg$) | 112.5±15.7 (80.8-142.1) | 115.6±18.9 (83.1-155.1) | 109.9±14.8 (85.1-134.8) |
| DPP ($mmHg$) | 59.2±6.7 (44.8-80.1) | 61.1±10.7 (43.1-84.7) | 59.6±9.0 (45.5-72.2) |
| CH ($mmHg$) | 10.0±1.3 (6.9-12.9) | **8.8±1.5 (6.0-12.5)** $*$ | 8.2±2.2 (4.2-11.0) |
| CRF ($mmHg$) | 9.9±1.4 (6.6-12.6) | 9.7±2.0 (6.9-14.0) | 8.6±1.4 (6.1-10.6) |
| CCT ($\mu m$) | 549.9±35.4 (506-666) | 533.2±36.6 (440-599) | **518.6±30.9 (462-564)**$*$ |
| MD ($dB$) | −−−−−− | -2.1±1.6 (-4.9 - 0.18) | -10.6±5.4 (-19.3 - -3.5) |
| PSD ($dB$) | −−−−−− | 3.1±1.5 (1.1-6.6) | 7.9±3.3 (2.4-10.9) |
| Choroidal Thickness ($\mu m$) | 188.52±55.13 (110.41-312.66) | 181.76±60.0 (104.2-292.16) | 202.58±38.53 (150.7-275.81) |
| $\Delta V$ ($\mu L$) | 4.66±2.72 (2.10-15.16) | 4.25±2.09 (2.27-10.59) | 5.28±2.29 (2.50-9.37) |
| Rigidity ($\mu L^{-1}$) | 0.044±0.022 (0.006-0.089) | 0.039±0.016 (0.014-0.069) | 0.038±0.020 (0.013-0.076) |
| PFR Deformation ($\mu m$) | 2.23±0.57 (1.17-3.91) | **2.00±0.28 (1.62-2.46)**$*$ | 2.27±0.39 (1.55-2.88) |

[a]Data presented as mean±$S.D.$(range). Variables in bold are significantly different from the Normal group ($*p < 0.05, **p < 0.01, ***p < 0.001$).

Average perifoveal retinal deformation proved to be larger in healthy eyes ($2.23 \pm 0.57\mu m$) than in eyes with EOAG ($2.00 \pm 0.28\mu m, p = 0.039$). Interestingly, no statistical difference was found between the Normal group and OAG ($2.27 \pm 0.39\mu m, p = 0.948$). Table 7.1 contains the demographics as well as the mean perifoveal retinal deformation values by diagnosis.

Intergroup comparisons of the other variables under study showed significant differences in central corneal thickness ($p = 0.044$) and corneal hysteresis ($p = 0.023$), however, the analysis of covariance showed that these variables have no effect on the differences found in PFR deformation.

In order to investigate the relationship between vascular and ocular parameters with perifoveal retinal deformation, Pearson correlation analysis was performed by diagnosis.

### 7.4.2 Linear Correlation Analysis

It results interesting the fact that only the Normal group showed significant correlations with PFR deformation. Healthy eyes with larger changes in ocular volume ($r = 0.412, p = 0.016$, Fig. 7.5a) as well as more elastic eyes (OR: $r = -0.409, p = 0.016$, Fig. 7.5b) showed larger perifoveal retinal deformation.

In the multiple regression analysis the ocular rigidity was the only statistically significant parameter to predict the variance of the PFR deformation in healthy eyes ($R^2 = 0.209, p = 0.028$).

$$PFR_{healthy} = 2.9556 - 14.346OR. \tag{7.1}$$

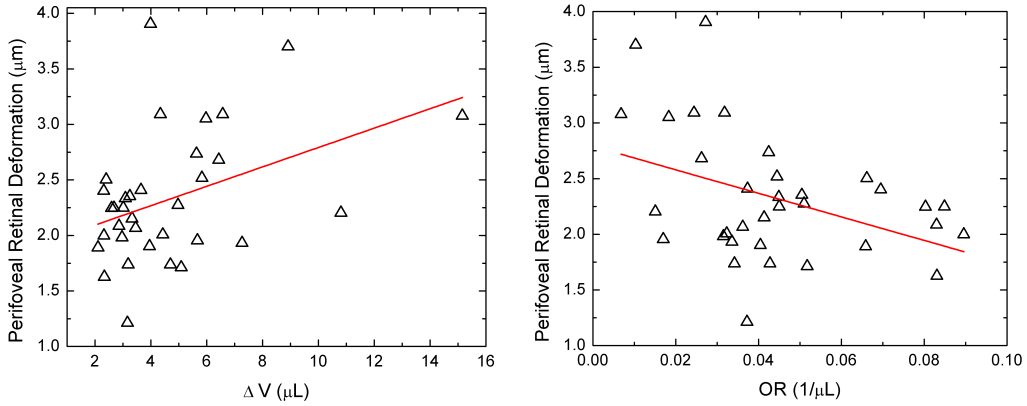


(a) (b)

**Figure 7.5 – Linear regression analysis for the Normal group: a) Perifoveal Retinal Deformation vs ocular volume change ($R^2 = 0.144$); b) PFR deformation vs ocular rigidity ($R^2 = 0.209$).**

Although no linear relationship with PFR deformation was found for neither of the glaucoma groups, it attracts attention the fact that choroidal thickness in the OAG group shows a borderline significant positive correlation with axial length ($r = 0.610, p = 0.06$), contrary to that exhibited by the EOAG group ($r = -0.43, p = 0.046$).

## 7.5 Discussion

Characterization of the perifoveal retinal displacement showed that mean PFR deformation is larger in healthy eyes compared with EOAG. This finding is in good agreement with several studies performed since the 1960's where it has been recognized that early glaucomatous damage can affect the macula [106],[107]. More recently, OCT imaging combined with automated perimetry has shown that, additionally to the thinning of the RNFL in the arcuate regions near the optic disc, thinning of the macular retinal ganglion cell + inner plexiform layers (RGC+) can also be seen in glaucoma suspects even when its visual field (24-12) is classified as normal [108].

Furthermore, video fluorescein angiograms have showed that choroidal blood refreshment time is significantly longer in patients with OAG compared with Normal and OHT [109], fact that also might help explaining the difference found since the measured deformation is mainly caused by choroidal filling.

It is surprising the fact that PFR deformation of the OAG cohort is not statistically different from that of the Normal group or from the EOAG. This finding could be attributed to several factors, e.g. the manner in which the OCT scanning was performed. It has been found that macular damage is typically arcuate in nature and it is often associated with local RNFL thinning in a narrow region of the disc. The macular vulnerability zone corresponds to large sections of the inferior macula which course into the inferior quadrant of the optic disc, the most damaged location in glaucoma, with more pronounced RGC+ thinning on the temporal side of the fovea and the degree of thinning increased with decreased MD [110]. Since the macular OCT image series were acquired to measure changes in choroidal thickness, the angle at which the line scan was positioned depended on the visibility of the choroid; consequently, the region scanned varies from subject to subject. It is possible that such variability resulted in the majority of the line scans in the OAG group located between $135^{o}$ and $180^{o}$ with respect to the fovea to disc axis, which is outside of the vulnerability zone, where the thinning of the RCG+ layer is more subtle. Thus, besides the restriction of the scanning angle, to include the measurement of the retinal layers' thicknesses would be key to understand the cause of the difference in PFR deformation between groups and possibly, to differentiate between the stages of glaucoma.

Using EDI OCT imaging it has been recently found that subfoveal and temporal choroidal thicknesses are thinner in patients with advanced OAG ($MD \leq 12dB$) compared to healthy subjects, even after adjusting for age and axial length [111]. However, in the present study there was no statistically significant difference between groups neither in CT (before or after adjustment) nor in ocular rigidity.

This lack of difference could be explained by the fact that the mean choroidal thickness used in this analysis is the average value calculated over the whole line scan, i.e., it includes the subfoveal as well as the nasal and temporal macular regions. Additionally, the sample size of this group is relatively small compared to the other two.

Regarding the linear correlations, the fact that perifoveal retinal deformation correlates positively with the change in ocular volume corroborates the assumption that the measured displacement is directly related to the pulsatile choroidal filling, at least in the macular region. Furthermore, the finding of larger deformation in more elastic eyes confirms that the amount of deformation experienced by the RGCs depends on the biomechanical properties of the tissue, as hypothesized. No significant correlation with PFR deformation was found in the glaucoma groups, however, the analysis of the other variables showed that an increase of $1dB$ in the PSD value would yield an approximate $1.14\mu m$ reduction in choroidal thickness change ($R^2 = 0.506, p = 0.0126$) in the OAG group. This correlation indicates that the progression of the disease is causing changes not only in the retinal layer structure but also in the biomechanical properties of the choroid and the sclera, and consequently, in the amount and distribution of the stress inflicted on the retina.

# Chapter 8

# Conclusions

Biomechanics plays a critical role in a significant number of ophthalmic diseases like glaucoma. The major concern in ocular biomechanical research is the capability to demonstrate that biomechanical properties of individual ocular tissues can be measurable in vivo, and even more, in a nonivasive manner. Current improvements in imaging technologies, as well as new techniques in image processing, are making possible the study of the structure and biomechanics of the sclera and LC. For example, a combination of a standard inflation test and wide-angle X-ray scattering, in posterior scleras of cadaver eyes, have shown that its collagen fiber architecture is highly anisotropic and inhomogeneous, with a larger degree of fiber alignment in the temporal/superior quadrant and lowest in the supero/nasal. Furthermore, it was found that regional variations in fiber anisotropy in the peripapillary sclera were different between glaucoma and normal eyes, with the former group displaying a more homogeneous structure, larger fiber stiffness and lower meridional strains [112],[113]. However, the question if eyes with a stiffer peripapillary sclera in normal conditions are more prone to glaucoma insult than those with a more elastic one remains.

Notwithstanding histology keeps providing insightful biomechanical infortmation, it can only investigate properties of small regions of the eye while a more comprehensive characterization is needed. Since the eye is a very complex structure of interconected tissues, several methods have been recently developed to study biomechanics ex vivo without the need of tissue sectioning, such as second harmonic-generated imaging, providing eye-specific measurements of the effects of different levels of IOP in human LC [114]. High-field magnetic resonance imaging have revealed outward bowing of the posterior sclera and anterior bulging of the cornea in sheep eyes due to IOP elevation, with a nonlinear corneoscleral shell mechanics and a highly anisotropic deformation of the scleral canal in the nasal direction, where the change in diameter exceeds the $300\mu m$ when IOP goes from 10 to $20mmHg$ [115].

However, most of the research in ocular biomechanics is performed using OCT imaging, where the use of adaptive optics and swept sources has allowed to investigate, for example, the response of the LC to IOP changes in vivo, although in an invasive manner. Recently, optic nerve head strains caused by the interplay effects of IOP and intracranial pressure were characterized in vivo in a rhesus macaque monkey, showing that variations in either pressure can cause substantial focal stretch and compression of the tissues of the LC, in a nonlinear way, and up to 20% [116]. This kind of studies in humans are usually performed comparing images before and after surgery [117], [118]. Among the few noninvasive procedures reported, a lamina cribrosa strain map of horizontal eye movements in healthy eyes was created using volumetric OCT scans, observing shearing deformation of the ONH tissues in adduction[1] ($20^{o}$), with temporal pulling and nasal compression in the transversal plane, possibly due to the action of the ON sheaths [119].

All the studies mentioned above, like the majority found in the literature, are static, measuring tissue displacements and deformations from a small set of images,

[1]Adduction: the action of drawing inward towards the midline of the body.

often 2 or 3, made of hundreds of averaged frames. Since the aim of ocular biomechanics is to elucidate the physiology and pathophysiology of the eye, dynamic studies are also required, preferably noninvasive, that at some point could be translated to the clinic in order to track the evolution of the patients through the development of the disease.

Focusing on that, the main purpose of this doctoral research was to design a method to measure pulsatile retinal deformation in vivo, noninvasively, to investigate its relevance as a novel ocular biomechanical descriptor and its relationship with the potential risk factors of the glaucomatous neuropathy.

The general strategy that has been followed in this work is the use of video rate OCT images of the optic nerve head as well as fully automated image analysis algorithms, that were specially created and continuously developed, to measure and determine Neuro-Peripapillary Retinal Deformation due to choroidal pulsatility.

The OCT imaging protocol chosen consists in series of OCT line scans of the same region of the ONH recorded during $20s$ at $20Hz$. Two image series, with 401 high resolution images each, are obtained per subject at $45^{o}$ and $135^{o}$ with respect to the fovea to disc axis, corresponding to the areas of major insult in glaucoma. Along with the image series, the heartbeat of the subject was recorded simultaneously.

In order to quantify retinal deformation, a fully automated algorithm to segment the peripapillary retina along with the ONH, and to compute peripapillary tissue displacements from the image series was developed. The segmentation method is based in morphological operations and includes a two-step contrast enhancement technique, designed to eliminate floaters in the vitreous, compensate inhomogeneities due to retinal blood vessels and to sharpen edges. It has been demonstrated that the proposed approach is able to accurately segment the ILM even when images show a substantial amount of speckle noise or shadowing, which is typical of high acquisition

rates, proving to be very robust when dealing with low quality images. Furthermore, it accurately detects the inner limiting membrane in healthy eyes as well as in several stages of glaucomatous pathology, which is of vital importance in clinical applications, with the advantages of having an easy implementation and low computation time.

The deformation analysis consists on using the segmented ILM profiles to measure changes in the axial distance between the temporal peripapillary retina and the prelaminar tissue due to choroidal pulsatility. The determined axial distance per frame is an average of the distances measured within a region of $600\mu m$ along the temporal side starting at the BMO, where blood vessels are less dense. N-PP retinal deformation is then defined as the standard deviation of the distances measured over the 400 frames of the image series. To assure that the measured deformation is mainly caused by blood flow pulsatility, the periodogram of the retinal distances in time is calculated and compared with that corresponding to the oximeter signal. Deformation results were rejected if the heart frequency was not identified in the spectrum of the distances. The reproducibility of the method was tested obtaining an ICC of 0.86 ($\alpha = 0.05$).

Using such methodology, pulsatile neuro-peripapillary retinal deformation was characterized in four clinical cohorts that cover part of the glaucoma spectrum: Early OAG, OAG Suspect, OHT and healthy eyes, recruited at the Glaucoma Clinic of the Maisonneuve-Rosemont Hospital in Montréal.

The analysis revealed that Early OAG ($3.2 \pm 0.7\mu m, p < 0.001$), OAG Suspect ($3.8 \pm 0.8\mu m, p = 0.045$) and OHT ($3.5 \pm 0.3\mu m, p = 0.015$) eyes have significantly smaller Inferotemporal pulsatile neuro-peripapillary retinal deformation compared with healthy eyes ($4.8 \pm 1\mu m$).

Several ocular, vascular and demographic parameters were included in the analysis from which CCT, OPA and DPP were found to be related with N-PP retinal

deformation for more than one cohort. Regarding parameters associated to glaucoma insult, eyes with larger vertical cup to disc ratio, thinner peripapillary RNFLs and larger visual field MD showed smaller N-PP retinal deformation.

Multivariate analysis showed that the Inferotemporal N-PP retinal deformation in the EOAG group can be described through a linear combination ($R^2 = 0.767, p < 0.001$) of intraocular pressure ($\beta = -0.21339, p = 0.0006$) and systolic perfusion pressure ($\beta = 0.019232, p = 0.0194$), two major predictors of glaucoma progression.

Taking advantage of the fact that the analysis algorithm can be easily applied to OCT images of the macular region, pulsatile deformation was investigated at the perifoveal retina in a set of patients belonging to the ocular rigidity study. In this case, the line scans were acquired at $8Hz$ for $50s$ using EDI and the scanning angle was chosen to maximize the visibility of the choroid. Here, changes in the axial distance between the perifoveal retina and the reference, located at the vertical location of the center of the umbo, were measured within a $600\mu m$ region at both sides of the fovea. Perifoveal retinal deformation is defined as the standard deviation of the distances measured in all frames.

Results showed that despite there was no significant difference in choroidal thickness, volume change or rigidity coefficient between groups, pulsatile Perifoveal Retinal Deformation was smaller in eyes with Early OAG ($2.00 \pm 0.28\mu m, p = 0.039$) compared to healthy eyes ($2.23 \pm 0.57\mu m$), indicating that the material properties of the macular retinal tissue might be significantly altered by the disease. A positive correlation between PFR deformation and change in ocular volume was found for the Normal group, corroborating that the observed deformation is driven by choroidal pulsatile blood flow. Furthermore, the fact that more elastic eyes showed larger PFR deformation suggests that an elastic cornea-sclera could absorb some of the volume change by expanding, leading to smaller pulsatile IOP changes and reduced pulsatile force exerted over the retinal layers.

The initial hypothesis was that there would be a pulsatile deformation of the retinal tissue and that this deformation would be correlated with glaucomatous axonal loss. In good agreement, this study revealed that the amount of deformation measured in diseased eyes was different from that of healthy eyes. It was observed average pulsatile deformation significantly larger in the normal group compared to eyes with early glaucoma in both regions, peripapillary and perifoveal. Moreover, PFR deformation (measured at the macula) resulted to be significantly smaller than N-PP retinal defomation (measured at the ONH) in healthy and EOAG eyes. Accordingly, it has been reported that the fundus pulsation amplitude (FPA)[2] distribution in healthy eyes is non uniform, being significantly higher in the macula than at the surrounding retina and twice as high in the optic disc [120], which validates the result obtained in this work since FPA is a point of measure of volume changes during the cardiac cycle.

The limitations of this study are that the design is cross-sectional and neither ethnicity nor gender are considered, although the great majority of the subjects were of European origins. Moreover, because of the stringent data requirements, in each cohort only a small number of subjects tested yielded usable data. Choroidal thickness measurements around the ONH would be of great importance in the understanding of the N-PP retinal deformation, unfortunately, accurate automated choroidal segmentation is not feasible in the obtained image series due to its low visibility and an additional image series would be needed using EDI technology to perform such measurements. Furthermore, to have PFR deformation measurements for the same subjects tested in the N-PP retinal deformation study would be ideal to compare the displacement in different parts of the retina under the same conditions, and even more, to investigate its relationship with choroidal volume changes and ocular rigidity.

[2]FPA is defined as the maximum distance change between the cornea and the fundus or retina during the cardiac cycle. Such distance changes are caused by the rhythmic filling of ocular vessels during systole and diastole.

Unfortunately, since both techniques were developed simultaneously this was no possible in the present work.

In a general overview, the obtained results suggest that the observed deformation (N-PP and PFR) is actually beneficial to axonal tissue, and that their diminishment is part of the glaucoma pathophysiology. We could speculate that the pulsatile deformation in some way counters the effects of the simultaneous pulsatile IOP, which itself, might be an impediment to axoplasmic flow.

All these findings support the belief that retinal deformation has the potential to be used as a new biomechanical descriptor of the eye. Further studies will be required to demonstrate the role of pulsatile macular and ONH deformations in the pathogenesis of glaucoma and whether this parameters might be useful for early diagnosis.

In conclusion, the obtained results suggests that the amount of Inferotemporal deformation as well as the Perifoveal deformation could be used as discriminator between healthy and diseased eyes, the former being able to distinguish even between OAG Suspects and Early OAG. The fact that the measured deformation correlates differently with the principal risk factors of the glaucomatous neuropathy depending on the diagnosis, shows that not only the physiological functions are altered by the disease but also the biomechanical properties of the tissue. Consequently, the measurement of the two parameters proposed in this thesis, Neuro-Peripapillary Retinal Deformation and Perifoveal Retinal Deformation, have the potential to be used as new biomechanical descriptors of the eye, helping in the understanding of the relationship between biomechanical properties of the retinal tissue and the insult of the optic nerve, not only in glaucoma but, in principle, in many other eye pathologies.

## 8.1 Perspectives

The findings presented in this thesis demonstrate that the measurement of the pulsatile retinal deformation should be further investigated, aiming to demonstrate its role in the pathogenesis of glaucoma. In order to achieve it, the following measures need to be taken into account:

First, it is necessary to continue the patient recruitment to increase the sample sizes and also to include two more cohorts: advanced glaucoma (MD $< -6dB$) and eyes with functional trabeculectomy blebs, in order to characterize the full spectrum of glaucomatous neuropathy. It also would be important to adjust the parameters of the OCT imaging of the ONH in such manner that choroidal thickness measurements around the optic nerve could be performed from the same image series. Such measurements will allow to understand the relationship between N-PP deformation and choroidal volume changes locally.

Currently both protocols have been merged and now ocular rigidity, N-PP and PFR deformation can be investigated with a single visit. However, the new protocol still needs to be optimized, first to reduce the variability in the scanning angle at the macula and then, to fasten the patient's testing time since 3 OCT image series need to be acquired per patient. It has also to be taken into account that the subjects are volunteers and of older age, and even though glaucoma patients are used to this kind of examination, they usually not tolerate more than two image series per session. The difficulty of imaging at multiple locations is derived from the need for long image series, opposed to the averaged static images commonly seen with OCT. Patients need to fixate much longer, often around 40 seconds for the ONH and approximately 1.5 minutes for the macula, in order to obtain an image series scanned at a single position.

It would be also interesting to perform a prospective study to investigate changes in retinal deformation at the ONH and the macula due to glaucoma progression. Additionally, since the Bruch's membrane opening (BMO) is one of the most important landmarks of the ONH, and is potentially the most consistent site from which to quantify the neuroretinal rim accurately [121], BMO-derived neuroretinal rim parameters recently proposed [122] that characterize the disc margin and peripapillary retinal nerve fiber layer thickness more accurately, such as the minimum rim width, could be measured dynamically from the image series. Such characterization will provide a more detailed picture about the neuroretinal tissue dynamics.

# References


[1] R. Buhrmann, W. Hodge and D. Gold, *Forecasting the Vision Loss Epidemic in Canada: Current and Projected Estimates of Age-Related Eye Disease*, Report submitted to the National Coalition for Vision Health, 2006.

[2] MR. Lesk, GL. Spaeth, A. Azuara-Blanco, SV. Araujo, LJ. Katz, AK. Terebuh, RP. Wilson, MR. Moster, CM. Schmidt, *Reversal of Optic Disc Cupping After Glaucoma Surgery Analyzed with a Scanning Laser Tomograph*, Ophthalmology, 1999; **106**(5):1013-1018.

[3] D. Huang, EA. Swanson, CP. Lin, JS. Schuman, WG Stinson, W. Chang, MR. Hee, T. Flotte, K.Gregory, CA. Puliafito, JG. Fujimoto, *Optical Coherence Tomography*, Science, 1991; **254**(5035): 1178-1181.

[4] K. Singh, C. Dion, M. Wajszilber, T. Ozaki, MR. Lesk, S. Costantino, *Measurement of Ocular Fundus Pulsation in Healthy Subjects Using a Novel Fourier-Domain Optical Coherence Tomography*, Invest. Ophthalmol. Vis. Sci., 2011; **52**(12):8927-8932.

[5] K. Singh, C. Dion, AG. Godin, F. Lorghaba, D. Descovich, M. Wajszilber, T. Ozaki, S. Costantino, MR. Lesk, *Pulsatile Movement of the Optic Nerve Head and the Peripapillary Retina in Normal Subjects and in Glaucoma*, Invest. Ophthalmol. Vis. Sci., 2012; **53**(12):7819-7824.

[6] T. Fabritius, S. Makita, M. Miura, R. Myllyla, Y. Yasuno, *Automated Segmentation of the Macula by Optical Coherence Tomography*, Opt. Express, 2009;**17**(18):15659-15669.

[7] MA. Mayer, J. Homegger, CY. Mardin, RP. Tomow, *Retinal Nerve Fiber Layer Segmentation on FD-OCT Scans of Normal Subjects and Glaucoma Patients*, Biomed. Opt. Express, 2010; **1**(5):1358-1381.

[8] SJ. Chiu, XT. Li, P. Nicholas, CA. Toth, JA. Izatt, S. Farsiu, *Automatic Segmentation of Seven Retinal Layers in SD-OCT Images Congruent with Expert Manual Segmentation*, Opt. Express, 2010; **18**(18):19423-19428.

[9] MD. Abramoff, K. Lee, M. Niemeijer, WL. Alward, EC. Greenlee, MK. Garvin, M. Sonka, YH. Kwon, *Automated Segmentation of the Cup and Rim from Spectral Domain OCT of the Optic Nerve Head*, Invest. Ophthalmol. Vis. Sci., 2009; **50**(12):5778-5784.

[10] K. Lee, M. Niemeijer, MK. Garvin, YH. Kwon, M. Sonka, MD. Abramoff, *Segmentation of the Optic Disc in 3-D OCT Scans of the Optic Nerve Head*, IEEE Trans. Med. Imaging, 2010; **29**(1):159-168.

[11] DC. Fernandez, HM. Salinas and CA. Puliafito, *Automated Detection of Retinal Layers Structures on Optical Coherence Tomography Images*, Opt. Express, 2005; **13**(25):10200-10216.

[12] DC. DeBuc, GM. Somfai, S. Ranganathan, E. Tatrai, M. Ferencz, CA. Puliafito, *Reliability and Reproducibility of Macular Segmentation Using a Custom-built Optical Coherence Tomography Retinal Image Analysis Software*, J. Biomed. Opt. 2009; **14**(6):064023.

[13] DC. DeBuc, HM. Salinas, S. Ranganathan, E. Tatrai, W. Gao, M. Shen, J. Wang, GM. Somfai, CA. Puliafito, *Improving Image Segmentation Performance and Quantitative Analysis Via a Computer-aided Grading Methodology for Optical Coherence Tomography Retinal Image Analysis*, J. Biomed. Opt., 2010; **15**(4):046015.

[14] Y. Wang, H. Jiang, M. Shen, BL. Lam, DC. DeBuc, Y. Ye, M. Li, A. Tao, Y. Shao, J. Wang, *Quantitative Analysis of the Intraretinal Layers and Optic Nerve Head Using Ultra-High Resolution Optical Coherence Tomography*, J. Biomed. Opt., 2012; **17**(6):066013.

[15] GJ. Tortora, B. Derrickson, *The Special Senses* in Principles of Anatomy and Physiology 13th edition, John Wiley and Sons Inc., 2012; 642-656.

[16] WF. Boron, EL. Boulpaep, *Sensory Transduction* in Medical Physiology: A cellular and Molecular Approach (updated edition), Elsevier-Saunders, 2005; 331-343.

[17] E. Hecht, *Geometrical Optics* in Optics 4th edition, Addison Wesley, 2002; 201-210.

[18] P. Artal, *Image Formation in the Living Human Eye*, Annu. Rev. Vis. Sci., 2015; (1):1-17.

[19] JS. Distelhorst and GM. Hughes, *Open-Angle Glaucoma*, Am Fam Physician, 2003; **67**(9):1937-1944.

[20] DR. Anderson, *Standard Perimetry*, Ophthalmol Clin North Am., 2003; **16**(2):205-212.

[21] MF. Armaly, *The Size and Location of the Normal Blind Spot*, Arch Ophthalmol., 1969; **81**(2):192-201.

[22] PGD. Spry and CA. Johnson, *Senescent Changes of the Normal Visual Field: an Age-Old Problem*, Optom Vis. Sci., 2001; **78**(6):436-441.

[23] PA. Sample, F. Dannheim, PH. Artes, J. Dietzsch, D. Henson, CA. Johnson, M. Ng, U. Schiefer, M. Wall, *Imaging and Perimetry Society Standards and Guidelines*, Optom Vis Sci, 2011; **88**:4-7.

[24] A. Heijl, *The Humphrey Field Analyzer, Construction and Concepts* in Sixth International Visual Field Symposium: Santa Margherita Ligure, May 27-31, 1984, Springer Netherlands, 1985; 77-84.

[25] B. Bengtsson, J. Olsson, A. Heijl, H. Rootzen, *A New Generation of Algorithms for Computerized Threshold Perimetry, SITA*, Acta Ophthalmol Scand., 1997; **75**(4):368-375.

[26] Visual Fields: Examination and Interpretation, Third Edition, Oxford University Press, 2011.

[27] LM. Alencar, FA. Madeiros, *The Role of Standard Automated Perimetry and Newer Functional Methods for Glaucoma Diagnosis and Follo-Up*, Indian J Ophthalmol., 2011; **59**, Suppl. S1:53-58.

[28] DF. Garway-Heath, D. Poinoosawmy, FW. Fitzke, RA. Hitchings, *Mapping the Visual Field to the Optic Disc in Normal Tension Glaucoma Eyes*, Ophthalmology, 2000; **107**(10):1809-1815.

[29] HA. Quigley, *Open-Angle Glaucoma*, N. Engl. J. Med., 1993; **328**(15):1097-1106.

[30] JB. Jonas, GC. Gusek, GOH. Naumman, *Optic Disc, Cup and Neuroretinal Rim Size, Configuration and Correlations in Normal Eyes*, Invest. Ophthalmol. Vis. Sci., 1998; **29**(7):1151-1158.

[31] JB. Jonas, GC. Gusek, GOH. Naumann, *Optic Disc Morphometry in Chronic Primary Open-Angle Glaucoma. I. Morphometric Intrapapillary Characteristics*, Graefe's Arch. Clin. Exp. Ophthalmol., 1988; **226**:522-530.

[32] JB. Jonas, MC. Fernandez, J. Sturmer, *Pattern of Glaucomatous Neuroretinal Rim Loss*, Ophthalmology 1993; **100**(1):63-68.

[33] MC. Leske, A. Heijl, M. Husein, B. Bengtsson, L. Hyman, E. Komaroff, *Factors for Glaucoma Progression and the Effect of Treatment. The Early Manifest Glaucoma Trial*, Arch. Ophthalmol. 2003; **121**(1):48-56.

[34] Eye Diseases Prevalence Research Group, *Prevalence of Open-angle Glaucoma Among adults in the United States*, Arch. Ophthalmol., 2004; **122**(4):532-538.

[35] HA. Quigley, SK. West, J. Rodriguez, B. Munoz, R. Klein, R. Snyder, *The Prevalence of Glaucoma in a Population-Based Study of Hispanic Subjects. Proyecto VER*, Arch. Ophthalmol. 2001; **119**(12):1819-1826.

[36] JM. Tielsch, J. Katz, A. Sommer, HA. Quigley, JC. Javitt, *Family History and Risk of Primary Open Angle Glaucoma. The Baltimore Eye Survey*, Arch. Ophthalmol., 1994; **112**(1):69-73.

[37] BEK. Klein, R. Klein, KE. Lee, *Heritability of Risk Factors for Primary Open-angle Glaucoma: The Beaver Dam Eye Study*, Invest. Ophthalmol. Vis. Sci., 2004; **45**(1):59-62.

[38] P. Mitchell, F. Hourihan, J. Sandbach, JJ. Wang, *The Relationship Between Glaucoma and Myopia: the Blue Mountains Eye Study*, Ophthalmology, 1999; **106**(10):2010-2015.

[39] TY. Wong, BEK. Klein, R. Klein, M. Knudtson, KE. Lee, *Refractive Errors, Intraocular Pressure, and Glaucoma in a White Population*, Ophthalmology, 2003; **110**(1):211-217.

[40] L. Xu, Y. Wang, S. Wang, Y. Wang, JB. Jonas, *High Myopia and Glaucoma Susceptibility. The Beijing Eye Study*, Ophthalmology, 2007; **114**(2):216-220.

[41] MO. Gordon, JA. Beiser, JD. Brandt, DK. Heuer, EJ. Higginbotham, CA. Johnson, JL. Keltner, JP. Miller, RK. Parrish, MR. Wilson, MA. Kass, *The Ocular Hypertension Treatment Study: Baseline Factors that Predict the Onset of Primary Open-Angle Glaucoma*, Arch. Ophthalmol. 2002; **120**(6):714-720.

[42] European Glaucoma Prevention Study Group, *Predictive Factors for Open-Angle Glaucoma among Patients with Ocular Hypertension in the European Glaucoma Prevention Study*, Ophthalmology, 2007; **114**(1):3-9.

[43] L. Schmetterer, MR. Lesk, *Blood Flow Changes in Glaucoma*, in Ocular Disease Mechanisms and Management, Elsevier Press, 2010; 223-230.

[44] MR. Lesk, AS. Hafez, *Role of Vascular Blood Flow in Pathogenesis of Glaucoma*, in Glaucoma Vol. 1, Elsevier Press, 2009; 91-102.

[45] H. Mueller, *Anatomische Beitraege zur Ophthalmologic: Ueber Nerven-Veranderungen an der Eintrittsstelle des Sehnerven*, Arch. Ophthalmol., 1858; **4**:1-5.

[46] E. von Jaeger, *Ueber glaucoma und seine heilung durch iridectommie*, Z Gesante Aertze Wein, 1858; **14**:484.

[47] A. Heijl, MC. Leske, B. Bengtsson, L. Hyman, M. Hussein, Early Manifest Glaucoma Trial Group, *Reduction of Intraocular Pressure and Glaucoma Progression: Results From the Early Manifest Glaucoma Trial*, Arch. Ophthalmol., 2002; **120**(10):1268-1279.

[48] PC. Maier, J. Funk, G. Schwarzer, G. Antes, YT. Falck-Ytter, *Treatment of Ocular Hypertension and Open Angle Glaucoma: Meta-analysis of Randomized Controlled Trials*, B. M. J., 2005; **331**(7509):134.

[49] Y. Suzuki, A. Iwase, M. Araie, T. Yamamoto, H. Abe, S. Shirato, Y. Kuwayama, HK. Mishima, H. Shimizu, G. Tomita, Y. Inoue, Y. Kitazawa, Tajimi Study Group, *Risk Factors for Open-Angle Glaucoma in a Japanese Population: The Tajimi Study*, Ophthalmology, 2006; **113**(9):1613-1617.

[50] YC. Fung, *Introduction: A Sketch of the History and Scope of the Field* in Biomechanics: Mechanical Properties of Living Tissues 2nd edition, Springer-Verlag New York, 1993; 1-22.

[51] IA: Sigal, C.R. Ethier, *Biomechanics of the Optic Nerve Head*, Exp. Eye Res., 2009; **88**(4):799-807.

[52] J. Flammer, S. Orgul, VP. Costa, N. Orzalesi, GK. Krieglsteing, LM. Serra, JP. Renard, E. Stefansson, *The Impact of Ocular Blood Flow in Glaucoma*, Prog. Retin. Eye Res., 2002; **21**:359-393.

[53] G. Michelson, MJ. Langhans, J. Harazny, A. Dichtl, *Visual Field Defect and Perfusion of the Juxtapapillary Retina and The Neuroretinal Rim Area in Primary Open-Angle Glaucoma*, Graefes ARch. Clin. Exp. Ophthalmol., 1998; **236**(2):80-85.

[54] CF. Burgoyne, JC. Downs, AJ. Bellezza, JKF. Suh, RT. Hart, *The Optic Nerve Head as a Biomechanical Structure: a New Paradigm for Understanding the Role of IOP-Related Stress and Strain in the Pathophysiology of Glaucomatous Optic Nerve Head Damage*, Prog. Reti. Eye Res., 2005; **24**(1):39-73.

[55] MR. Hernandez, *The Optic Nerve Head in Glaucoma: Role of Astrocytes in Tissue Remodeling*, Prog. Retin. Eye Res., 2000; **19**(3):297-321.

[56] NS. Levy, EE. Crapps, *Displacement of Optic Nerve Head in Response to Short-term Intraocular Pressure Elevation in Human Eyes*, Arch. Ophthalmol., 1984; **102**(5):782-786.

[57] DB. Yan, FM. Coloma, A. Metheetrairut, GE. Trope, JG. Heathcote, CR. Ethier, *Deformation of the Lamina Cribrosa by Elevated Intraocular Pressure*, Br. J. Ophthalmol., 1994; **78**(8):643-648.

[58] J. Albon, PP. Purslow, WS. Karwatowski, DL. Easty, *Age Related Compliance of the Lamina Cribrosa in Human Eyes*, Br. J. Ophthalmol., 2000; **84**(3):318-323.

[59] IG. Pallikaris, GD. Kymionis, HS. Ginis, GA. Kounis, M.K Tsilimbaris, *Ocular Rigidity in Living Human Eyes*, Invest. Ophthalmol. Vis. Sci., 2005; **46**(2):409-414.

[60] MR. Lesk, AS. Hafez, D. Descovich, *Relationship Between Central Corneal Thickness and Changes of the Optic Nerve Head Topography and Blood Flow After Intraocular Pressure Reduction in Open-Angle Glaucoma and Ocular Hypertension*, Arch. Ophthalmol., 2006; **124**(11):1568-1572.

[61] ASC. Reis, N. O'Leary, MJ. Stanfield, LM. Shuba, MT. Nicolela, BC. Chauhan, *Laminar Displacement and Prelaminar Tissue Thickness Change after Glaucoma Surgery Imaged with Optical Coherence Tomography*, Invest. Ophthalmol. Vis. Sci., 2012; **53**(9):5819-5826.

[62] MA. Fazio, R. Grytz, JS. Morris, L. Bruno, SK. Gardiner, CA. Girkin, JC. Downs, *Age-Related Changes in Human Peripapillary Scleral Strain*, Biomech. Model Mechanobiol., 2014; **13**(3):551-563.

[63] J. Albon, P. Purslow, W. Karwatowski, D. Easty, *Age Related Compliance of the Lamina Cribrosa in Human Eyes*, Br. J. Ophthalmol., 2000; **84**(3):318-323.

[64] IA. Sigal, JG. Flanagan, CR. Ethier, *Factors Influencing Optic Nerve Head Biomechanics*, Invest. Ophthalmol. Vis. Sci., 2005; **46**(11):4189-4299.

[65] IA. Sigal, JG. Flanagan, I. Tertinegg, CR. Ethier, *Predicted Extension, Compression and Shearing of the Optic Nerve Head Tissues*, Exp. Eye Res., 2007; **85**(3):312-322.

[66] A. Harris, G. Guidoboni, JC. Arciero, A. Amireskandari, LA. Tobe, BA. Siesky, *Ocular Hemodynamics and Glaucoma: the Role of Mathematical Modeling*, Eur. J. Ophthalmol. 2013; **23**(2):139-146.

[67] C. Bowd, LM. Zangwill, FA. Madeiros, IM. Tavares, EM. Hoffmann, RR. Bourne, PA. Sample, RN. Weinreb, *Structure-Function Relationships Using Confocal Scanning Laser Ophthalmosxopy, Optical Coherence Tomography, and Scanning Laser Polarimetry*, Invest. Ophthalmol. Vis. Sci., 2006; **47**(7):2889-2895.

[68] R. Sihota, P. Sony, V. Gupta, T. Dada, R. Singh, *Diagnostic Capability of Optical Coherence Tomography in Evaluating the Degree of Glaucomatous Retinal Nerve Fiber Damage*, Invest. Ophthalmol. Vis. Sci., 2006; **47**(5):2006-2010.

[69] LV. Wang, H. Wu, *Optical Coherence Tomography* in Biomedical Optics: Principles and Imaging, John Wiley and Sons Inc., 2007; 181-218.

[70] K. Singh, C. Dion, S. Costantino, M. Wajszilber, MR. Lesk, T. Ozaki, *Development of a Novel Instrument to Measure the Pulsatile Movement of Ocular Tissues*, Exp. Eye Res., 2010; **91**(1):63-68.

[71] JS. Friedenwald, *Contribution to the Theory and Practice of Tonometry*, Am. J Ophthalmol., 1937; **20**(10):985-1024.

[72] L. Beaton, J. Mazzaferri, F. Lalonde, M. Hidalgo-Aguirre, D. Descovich, MR. Lesk, S. Costantino, *Non-Invasive Measurement of Choroidal Volume Change and Ocular Rigidity Through Automated Segmentation of High-Speed OCT Imaging*, Biomed. Opt. Express, 2015; **6**(5):1694-1706.

[73] ME. Langham, RA. Farrell, V. O'Brien, DM. Silver, P. Schilder, *Blood Flow in the Human Eye*, Acta Ophthalmol Suppl., 1998; **67**(S191):9-13.

[74] L. Schmetterer, S. Dallinger, O. Findl, U. Graselli, HG. Eichler, M. Woltz, *A Comparison Between Laser Interferometric Measurement of Fundus Pulsation and Pneumotonometric Measurement of Pulsatile Ocular Blood Flow 2. Effects of Changes in pCO2 and pO2 and of Isoproterenol*, Eye, 2000; **14**:46-52.

[75] H. Kasprzak, DR. Iskander, T. Bajraszewski, A. Kowalczyk, W. Nowak-Szczepanowska, *High Accuracy Measurement of Spectral Characteristics of Movements of the Eye Elements*, Opt. Pura Apl., 2007; **40**(1):7-11.

[76] CE. Riva, P. Titze, M. Hero, BL. Petrig, *Effect of Acute Decreases of Perfusion Pressure on Choroidal Blood Flow in Humans*, Invest. Ophthalmol. Vis. Sci., 1997; **38**(9):1752-1760.

[77] B. Kiss, S. Dallinger, K. Polak, O. Findl, HG. Eichler, L. Schmetterer, *Ocular Hemodynamics during isometric exercise*, Microvasc. Res., 2001; **61**(1):1-13.

[78] TF. Chan and LA. Vese, *Active Contours without Edges*, IEEE Trans. Image Process., 2001; **10**(2):266-277.

[79] C. Li, C. Xu, C. Gui, MD. Fox, *Level Set Evolution without Re-initialization: a New Variational Formulation*, in Proc. IEEE Conf. on Computer Vision and Pattern Recognition, 2005; pp. 430-436.

[80] W. Yu, F. Franchetti, YJ. Chang, T. Chen, *Fast and Robust Active Contours for Image Segmentation*, in Proc. IEEE Int. Conf. on Image Processing (ICIP), 2010.

[81] R. Ksantono, B. Boufama, S. Memar, *A New Efficient Active Contour Model without Local Initialization for Salient Object Detection*, EURASIP J. Image Video Process., 2013; **2013**:40.

[82] M. Hidalgo-Aguirre, J. Gitelman, MR. Lesk, S. Costantino, *Automatic Segmentation of the Optic Nerve Head for Deformation Measurements in Video Rate Optical Coherence Tomography*, J. Biomed. Opt., 2015; **20**(11):116008.

[83] MJA. Girard, NG. Strouthidis, CR. Ethier, JM. Mari, *Shadow Removal and Contrast Enhancement in Optical Coherence Tomography Images of the Human Optic Nerve Head*, Invest. Ophthalmol. Vis Sci., 2011; **52**(10):7738-7748.

[84] R. Koprowski and Z. Wrobel, *Identification of Layers in a Tomographic Image of an Eye Based on the Canny Edge Detection*, in Information Technologies Biomedicine, Advances in Soft Computing, 2008; **47**:232-239. Springer-Verlag, Berlin, Heidelberg.

[85] R. Koprowski and Z. Wrobel, *Hierarchic Approach in the Analysis of Tomographic Eye Image*, in Computer Recognition System 3, Advances in Intelligent and Soft Computing, 2009; **57**:463-470

[86] F. Bochmann, GS. Ang, A. Azuara-Blanco, *Lower Corneal Hysteresis in Glaucoma Patients with Acquired Pit of the Optic Nerve*, Graefes Arch Clin Exp Ophthalmol., 2008; **246**:735.

[87] SA. Hussnain, JB. Alsberge, JR. Ehrlich, M. Shimmyo, NM. Radcliffe, *Change in Corneal Hysteresis Over Time in Normal, Glaucomatous and Diabetic Eyes*, Acta Ophthalmol., 2015; **93**(8):627-630.

[88] TS. Prata, VC. Lima, CG. Vasconcelos de Morales, LM. Guedes, FP. Magalhaes, SH. Teixeira, R. Ritch, A. Paranhos Jr, *Factors Associated with Topographic Changes of the Optic Nerve Head Induced by Acute Intraocular Pressure Reduction in Glaucoma Patients*, Eye, 2011; **25**:201-207.

[89] I. Dielemans, JR. Vingerling, D. Algra, A. Hofman, DE. Grobbee, PT. de Jong, *Primary Open-Angle Glaucoma, Introcular Pressure, and Systemic Blood Pressure in the General Elderly Population. The Rotterdam Study*, Ophthalmology, 1995; **102**(1):54-60.

[90] L. Bonomi, G. Marchini, M. Marraffa, P. Bernardi, R. Morbio, A. Varotto, *Vascular Risk Factors for Primary Open Angle Glaucoma: the Egna-Neumarkt Study*, Ophthalmology, 2000; **107**(7):1287-1293.

[91] HA. Quigley, SK. West, J. Rodriguez, B. Munoz, R. Klein, R. Synder, *The Prevalence of Glaucoma in a Population-Based Study of Hispanic Subjects. Proyecto Ver*, Ophthalmology, 2008; **119**(12):1819-1826.

[92] MC. Leske, SY. Wu, A. Hennis, R. Honkanen, B. Nemesure, BESs Study Group, *Risk Factors for Incident Open-Angle Glaucoma: the Barbados Eye Studies*, Ophthalmology, 2008; **115**(1):85-93.

[93] JM. Tielsch, J. Katz, A. Sommer, HA. Quigley, JC. Javitt, *Hypertension, Perfusion Pressure, and Primary Open-Angle Glaucoma. A Population-Based Assessment*, Arch. Ophthalmol., 1995; **113**(2):216-221.

[94] MC. Leske, A. Heijl, L. Hyman, B. Bengtsson, L. Dong, Z. Yang, EMGT group, *Predictors of Long-Term Progression in the Early Manifest Glaucoma Trial*, Ophthalmology, 2007; **114**(11):1965-1972.

[95] TS. Prata, VC. Lima, LM. Guedes, LG. Biteli, SH. Teixeira, CG. de Morales, R. Ritch, A. Paranhos Jr, *Association Between Corneal Biomechanical Properties and Optic Nerve Head Morphology in Newly Diagnosed Glaucoma Patients*, Clin. Experiment. Ophthalmol., 2012; **40**(7):682-688.

[96] AP. Khawaja, MPY. Chan, DC. Broadway, DF. Garway-Heath, R. Luben, JLY. Yip, S. Hayat, KT. Khaw, PJ. Foster, *Corneal Biomechanical Properties and Glaucoma Related Quantitative Traits in the EPIC-Norfolk Eye Study*, Invest. Ophthalmol. Vis. Sci., 2014; **55**(1):117-124.

[97] H. Chukai, M. Zhang, Y. Huang, B. Chen, DSC. Lam, N. Congdon, *Corneal Hysteresis is Correlated with reduction in Axial Length after Trabeculectomy*, Curr. Eye Res., 2012; **37**(5):381-387.

[98] C. Scott, *An Evaluation of Corneal Hysteresis in Normal Eyes*, American Academy of Optometry Annual Meeting 2006; Abstract 065208.

[99] MJA. Girard, JKF. Suh, M. Bottlang, CF. Burgoyne, JG. Downs, *Biomechanical Changes in the Sclera of Monkey Eyes Exposed to Chronic IOP Elevations*, Invest. Ophthalmol. Vis. Sci., 2011; **52**(8):5656-5669.

[100] PJ. Harasymowycz, DG. Papamatheakis, M. Ennis, M. Brady, KD. Gordon, *Relationship Between Travoprost and Central Corneal Thickness in Ocular Hypertension and Open-Angle Glaucoma*, Cornea, 2006; **26**(1):34-41.

[101] Y. Zhong, X. Shen, J. Yu, H. Tan, Y. Cheng, *The comparison of the Effects of Latanoprost, Travoprost, and Bimatoprost on Central Corneal Thickness*, Cornea, 2011; **30**(8):861-864.

[102] JD. Lindsey, K. Kashiwagi, F. Kashiwagi, RN. Weinreb, *Prostaglandins Alter Extracellular Matrix Adjacent to Human Ciliary Muscle Cells in Vitro*, Invest. Ophthalmol. Vis. Sci., 1997; **38**(11):2214-2223.

[103] A. Lanzagorta-Aresti, F. Pastor-Pascual, P. Alcocer-Yuste, J. Menezo-Rozalen, A. Navea-Tejerina, *The Effect of Prostaglandin Analogs on Corneal Hysteresis*, Invest. Ophthalmol. Vis. Sci., 2008; **49**(13):2622.

[104] G. Bolivar, C. Sanchez-Barahona, M. Teus, MA. Castejon, J. Paz-Moreno-Arrones, C. Gutierrez-Ortiz, DG. Mikropoulos, *Effect of Topical Prostaglandin Analogues on Corneal Hysteresis*, Acta Ophthalmol., 2015; **93**(6):e495-e498.

[105] M. Hidalgo-Aguirre, S. Costantino, MR. Lesk, *Pilot Study of the Pulsatile Neuro-Peripapillary Retinal Deformation in Glaucoma and its Relationship with Glaucoma Risk Factors*, Curr. Eye Res., 2017; **42**(12):1620-1627.

[106] E. Aulhorn, H. Harms, *Early Visual Field Defects in Glaucoma*, Glaucoma, Tutzing Symposium, August 1966; 151-186.

[107] SM. Drance, *The Early Field Defects in Glaucoma*, Invest. Ophthalmol. Vis. Sci., 1969; **8**(1):84-91.

[108] DC. Hood, AS. Raza, CGV. de Moraes, CA. Johnson, JM. Liebmann, R. Ritch, *The Nature of Macular Damage in Glaucoma as Revealed by Averaging Optical Coherence Tomography Data*, Transl. Vis. Sci., 2012; **1**(1):3.

[109] HFA. Duijm, TJTP. van den Berg, EL. Greve, *A Comparison of Retinal and Choroidal Hemodynamics in Patients with Primary Open-angle Glaucoma and Normal-pressure Glaucoma*, Am. J. Ophthalmol., 1997; **123**(5):644-656.

[110] DC. Hood, AS. Raza, CG. de Moraes, JM. Liebmann, R. Ritch, *Glaucomatous Damage of the Macula*, Prog Retin Eye Res., 2013; **32**:1-21.

[111] R. Sacconi, N. Deotto, T. Merz, R. Morbio, S. Casati, G. Marchini, *SD-OCT Choroidal Thickness in Advanced Primary Open-Angle Glaucoma*, J Glaucoma, 2017; **26**(6):523-527.

[112] JK. Pijanka, B. Coudrillier, K. Ziegler, T. Sorensen, KM. Meek, TD. Nguyen, HA. Quigley, C. Boote, *Quantitative Mapping of Collagen Fiber Orientation in Non-Glaucoma and Glaucoma Posterior Human Sclerae*, Invest. Ophthalmol. Vis. Sci., 2012; **53**(9):5258-5270.

[113] B. Coudrillier, JK. Pijanka, JL. Jefferys, A. Goel, HA. Quigley, C. Boote, TD. Nguyen, *Glaucoma-related Changes in the Mechanical Properties and Collagen Micro-architecture of the Human Sclera*, PLoS ONE, 2015; **10**(7):e0131396.

[114] IA. Sigal, JL. Grimm, NJ. Jan, K. Reid, DS. Minckler, DJ. Brown, *Eye-Specific IOP- induced Displacements and Deformations of Human Lamina Cribrosa*, Invest. Ophtahlmol. Vis. Sci., 2014; **55**(1):1-15.

[115] AP. Voorhees, LC. Ho, NJ. Jan, H. Tran, Y. van der Merwe, K. Chan, IA. Sigal, *Whole-Globe Biomechanics Using High-Field MRI*, Exp Eye Res., 2017; **160**:85-95.

[116] H. Tran, J. Grimm, B. Wang, MA. Smith, A. Gogola, S. Nelson, E. Tyler-Kabara, J. Schuman, G. Wollstein, IA. Sigal, *Mapping In-Vivo Optic Nerve Head Strains Caused by Intraocular and Intracranial Pressures*, Proc. SPIE 10067, Optical Elastography and Tissue Biomechanics IV, 2017; 100670B.

[117] WJ. Lee, HJ. Kim, KH. Park, YW. Kim, MJA. Girard, JM. Mari, SK. Kim, JH. Phi, JW. Jeoung, *Dynamic Change in Optic Nerve After Intracranial Pressure Reduction in Children*, Ophthalmology Reports, 2017; doi.org/10.1016/j.ophtha.2017.05.017.

[118] H. Quigley, K. Arora, S. Idrees, F. Solano, S. Bedrood, C. Lee, J. Jefferys, T. Nguyen, *Biomechanical Responses of Lamina Cribrosa to Intraocular Pressure Change Assessed by Optical Coherence Tomography in Glaucoma Eyes*, Invest. Ophthalmol. Vis. Sci., 2017; **58**(5):2566-2577.

[119] X. Wang, MR. Beotra, TA. Tun, M. Baskaran, S. Perera, T. Aung, NG. Strouthidis, D. Milea, MJA. Girard, *In Vivo 3-Dimensional Strain Mapping Confirms Large Optic Nerve Head Deformations Following Horizontal Eye Movements*, Invest. Ophthalmol. Vis. Sci., 2016; **57**(13):5825-5833.

[120] L. Schmetterer, S. Dallinger, O. Findl, HG. Eichler, M. Wolzt, *A Comparison Between Laser Interferometric Measurement of Fundus Pulsation and Pneumotonometric Measurement of Pulsatile Ocular Blood Flow 1. Baseline Considerations*, Eye, 2000; **14**:39-45.

[121] ASC. Reis, GP. Sharpe, H. Yang, MT. Nicolela, CF. Burgoyne, BC. Chauhan, *Optic Disc Margin Anatomy in Patients with Glaucoma and Normal Controls with Spectral Domain Optical Coherence Tomography*, Ophthalmology, 2012; **119**(4):738-747.

[122] ASC. Reis, N. O'Leary, H. Yang, GP. Sharpe, MT. Nicolea, CF. Burgoyne, BC. Chauhan, *Influence of Clinically Invisible, but Optical Coherence Tomography Detected, Optic Disc Margin Anatomy on Neuroretinal Rim Evaluation*, Invest. Ophthalmol. Vis. Sci., 2012; **53**(4):1852-1860.

# Appendix A

# Publications, Conferences and Awards

## A.1 Scientific Publications

1. **M. Hidalgo-Aguirre**, S. Costantino, MR. Lesk, *Pilot Study of the Pulsatile Neuro-Peripapillary Retinal Deformation in Glaucoma and its Relationship with Glaucoma Risk Factors*, Curr. Eye Res., 2017; 42(12):1620-1627.

2. **M. Hidalgo-Aguirre**, J. Gitelman, MR. Lesk, S. Costantino, *Automatic Segmentation of the Optic Nerve Head for Deformation Measurements in Video Rate Optical Coherence Tomography*, J. Biomed. Opt., 2015; 20(11):116008.

3. L. Beaton, J. Mazzaferri, F. Lalonde, **M. Hidalgo-Aguirre**, D. Descovich, MR. Lesk, S. Costantino, *Non-Invasive Measurement of Choroidal Volume Change and Ocular Rigidity Through Automated Segmentation of High-Speed OCT Imaging*, Biomed. Opt. Express, 2015; 6(5):1694-1706.

## A.2 Conference Presentations and Invited Talks

- "Neuroretinal tissue deformation in healthy subjects and glaucoma patients by automatic segmentation of video rate OCT image series". M. Hidalgo-Aguirre, MR. Lesk, S. Costantino. Centre de Recherche, Hopital Maisonneuve-Rosemont, Montreal, Qc., CA (2015).

- "Deformation measurements of retinal nerve fiber layer by automatic segmentation on video rate optical coherence tomography". M. Hidalgo-Aguirre, MR.

Lesk, S. Costantino. 27e Journee de la Recherche en Ophtalmologie de l'Univeriste de Montreal, Mtl., Qc., CA (2015).

- "Automatic segmentation of the retinal nerve fiber layer for deformation measurements on high frequency OCT". M. Hidalgo-Aguirre, J. Gitelman, MR. Lesk, S. Costantino. 20e réunion annuelle du Réseau de recherche en santé de la vision (RRSV), Quebec, Qc., CA (2014).

- "Deformation measurements of the retinal nerve fiber layer by automatic segmentation on high frequency OCT". M. Hidalgo-Aguirre, J. Gitelman, MR. Lesk, S. Costantino. 2º semaine de la recherche de l'Hopital Maisonneuve-Rosemont, Montreal, Qc., CA., (2014).

- "Automatic segmentation of the retinal nerve fiber layer for deformation measurements on high frequency OCT". M. Hidalgo-Aguirre, J. Gitelman, D. Descovich, MR. Lesk, S. Costantino. 16th Photonics North Conference, Montreal, QC., CA (2014).

- "Deformation measurements of the retinal nerve fiber layer by automatic segmentation on high frequency optical coherence tomography". M. Hidalgo-Aguirre, J. Gitelman, D. Descovich, MR. Lesk, S. Costantino. Association for Research in Vision and Ophthalmology Annual Meeting (ARVO), Orlando, Florida, USA (2014).

- "Characterization of the retinal deformation from normal to glaucomatous eyes". M. Hidalgo-Aguirre, J. Gitelman, MR. Lesk, S. Costantino. CREATE Neuroengineering program, McGill University, Montreal, Qc., CA (2013).

- "Characterization of the retinal deformation as a promising glaucoma diagnostic technique". M. Hidalgo-Aguirre, J. Gitelman, MR. Lesk, S. Costantino. 19e reunion Annuelle du Reseau de Recherche en Sante de la Vision, Montreal, Qc., CA (2013).

- "Characterization of the retinal deformation in normal and glaucomatous eyes". M. Hidalgo-Aguirre, J. Gitelman, MR. Lesk, S. Costantino. 20e journee de la recherche de l'Hopital Maisonneuve-Rosemont, Montreal, Qc., CA., (2013).

## A.3 Awards

Full scholarship for PhD studies, National Council of Science and Technology (CONACyT), México.

# Appendix B

# Résumé

Le glaucome est la deuxième cause de cécité dans le monde entier. Les faits que glaucome ne présente aucun symptôme jusqu'à ce que la perte visuelle importante s'est produite et que les principales causes de cette neuropathie demeurent inconnus rendent difficile pour les deux, le diagnostic et le traitement. Alors que la pression intraoculaire (PIO) reste le principal facteur de risque, d'autres paramètres comme la pression de perfusion oculaire basse, le flux sanguin oculaire et l'élasticité de la sclère et de la lame criblée ont été identifiés dans les dernières années comme facteurs additionnels potentiells de le risque, de la prévalence et de la progression de la neuropathie glaucomateuse.

Théoriquement, la susceptibilité d'un individu à la PIO est déterminée en partie par la géométrie de l'œil et l'anatomie des tissus oculaires, par conséquent, il semble naturel de considérer la biomécanique comme cadre pour expliquer comment le stress et la déformation liés à la PIO influencent la physiologie et la physiopathologie des tissus conjonctifs, neurologiques et vasculaires, provoquant les changements dans l'intégrité structurelle et fonctionnelle du nerf optique observés dans le glaucome. La principale difficulté est alors de comprendre comment la biomécanique oculaire, en combinaison avec les facteurs de risque précités, se traduit par des lésions tissulaires.

Il a été démontré que le glaucome est directement lié aux déficiences de flux sanguin dans la circulation rétinienne et choroïdienne. La choroïde a le plus haut débit sanguin par gramme de tissu de tous les organes du corps humain et ce flux est 80% pulsatile. Il a émis l'hypothèse que cette pulsatilité déplace la rétine vers l'avant tout en élargissant la sclère, générant une déformation pulsé des axones qui s'étendent de la rétine à travers la lame criblée vers le cerveau. Si l'on considère que les propriétés mécaniques des tissus sont également modifiées durant la progression de la maladie, il est alors très probable que telles déformations peuvent changer.

Dans ce contexte, le présent ouvrage est centré sur l'étude et la caractérisation de la déformation du tissu rétinien péripapillaire en raison de la pulsatilité vasculaire choroïdienne et son implication éventuelle dans des lésions axonales et la perte de la couche des fibres nerveuses rétiniennes dans le glaucome. La stratégie générale conçue pour effectuer cette enquête consiste à utiliser des images de la tomographie par cohérence optique, acquis á vidéo-taux, du nerf optique combinée avec des algorithmes d'analyse d'images entièrement automatisés et spécialement développés pour mesurer et déterminer la déformation rétinienne. Une étude transversale a été réalisée à la clinique d'ophtalmologie de l'Hôpital Maisonneuve-Rosemont pour évaluer la déformation rétinienne péripapillaire dans une cohorte de patients représentative du spectre glaucomateux.

Les résultats obtenus montrent que les yeux normaux ont une déformation de la rétine péripapillaire significativement plus élevée par rapport au spectre glaucomateux. La déformation mesurée est corrélée différemment avec les principaux facteurs de risque de la neuropathie glaucomateuse selon le diagnostic. Le déplacement rétinien réduit s'est avéré être lié à des facteurs prédictifs de la progression du glaucome, montrant que les propriétés biomécaniques de l'œil sont modifiées, même quand il n'y a aucun changement évident dans la structure du nerf optique.

En raison de la versatilité de l'algorithme de segmentation, il a été possible d'effectuer une étude préliminaire pour étudier la déformation rétinienne autour de la macula en utilisant des images précédemment acquises pour une étude clinique différente. Dans ce cas, la déformation rétinien périfovéolaire dans les yeux sains a été significativement plus grande que dans le glaucome précoce. En outre, la rigidité oculaire ainsi que les changements du volume oculaire ont été corrélés avec le déplacement rétinien perifovéolaire dans les yeux sains, ce qui confirme que la déformation observée est causée par la pulsatilité choroïdienne.

Tous ces résultats suggèrent que l'ampleur de la déformation de la rétine devrait être étudiée plus attentivement car il pourrait être potentiellement utilisé comme un nouveau descripteur biomécanique de l'œil pour un diagnostic précoce et l'évaluation de la progression du glaucome.

**Mots-clés**: Nerf Optique; Glaucome; Traitement d'Image; Tomographie par Cohérence Optique; Biomécanique Oculaire; Déformation Rétinienne.

# Appendix C

# Synopsis en Français

## C.1 Introduction

Le glaucome est une maladie très complexe caractérisée par la perte de la vision périphérique. C'est la deuxième cause de cécité dans le monde entier, affectant plus de 400 000 Canadiens, avec plus de 20 000 qui risquent de devenir aveugle à cause de cette maladie en 2031 [1]. De plus, environ 50% des personnes qui sont touchées par la maladie ne sont pas diagnostiqués.

Grâce aux progrès des technologies d'imagerie, les médecins ont appris à compter sur ces dispositifs afin de différencier les patients sains de ceux qui sont atteints de glaucome selon des changements caractéristiques visibles du nerf optique associés avec les patrons typiques de perte visuelle dans le glaucome. L'imagerie du nerf optique (NO) a montré que le volume de la papille optique augmente avec la pression intraoculaire (PIO), et que ces changements peuvent parfois être partiellement renversés en réduisant la PIO [2]. Cependant, comme le glaucome ne présente aucun symptôme jusqu'à ce qu'une perte visuelle importante s'est produite, il devient difficile à la fois de diagnostiquer et de le traiter. En outre, de prévoir à quelle vitesse la maladie va progresser est toujours une tâche impossible, empéchant la possibilité de distinguer

les patients atteints de glaucome qui devient rapidement dégénératif de ceux ayant une évolution plus bénigne, limitant ainsi les options et l'intensité du traitement.

Parmi ces nouvelles technologies, la tomographie par cohérence optique (OCT) est une puissante technique d'imagerie non invasive qui est devenue l'outil standard dans la clinique et la recherche en ophtalmologie, offrant une visualisation directe et précise de la rétine et sa structure [3]. Cette information aide à détecter et surveiller une variété de maladies de la rétine comme la dégénérescence maculaire liée à l'âge, la rétinopathie diabétique et le décollement de la rétine. L'OCT est particulièrement prometteur pour détecter le glaucome, où une caractérisation précise des changements du nerf optique ainsi que de la couche des fibres nerveuses rétiniennes péripapillaires est d'une importance cruciale pour la gestion de la maladie.

En utilisant cette technique, il a été démontré récemment que le tissu autour du NO est déformé lors de pulsations cardiaques [4], et que ce mouvement est différent chez les patients sains et les patients avec glaucome [5]. Toutefois, étant donné que la grande majorité des projets de recherche fondés sur l'OCT s'appuient sur des images statiques composées de plusieurs frames en moyenne, ces résultats soulignent la pertinence des études dynamiques pour lesquelles il est nécessaire de développer de nouvelles stratégies d'imagerie.

Un élément essentiel du traitement des données OCT est la segmentation, et un de ses problèmes plus difficiles est la conception d'un système qui fonctionne correctement en applications cliniques, c'est-à-dire le développement de méthodes robustes capables de traiter les cas pathologiques, où la structure de la rétine peut changer radicalement. Plusieurs méthodes ont été proposées pour segmenter la limite vitré-rétine dans des images OCT de la region maculaire [6]-[8]; cependant, ces modèles ne peuvent pas être simplement appliqués à la région du NO en raison des différences anatomiques. Bien que la segmentation du NO fait partie du logiciel d'analyse des appareils commerciaux d'OCT, ce type de logiciel n'est pas apte à être intégré dans

les routines d'analyse puisque leur code source n'est pas disponible et ils ne sont pas compatibles entre les différentes compagnies d'OCT. Il faut également considérer que l'étude des processus dynamiques nécessite la segmentation de grands ensembles d'images de qualité médiocre, une tâche non triviale qui n'a pas été accomplie avant. Par conséquent, des mesures systématiques de la dynamique du tissu du NO ne peuvent être réalisées avec les outils de logiciels commerciaux, qui visent principalement des paramètres cliniques, ni avec les méthodes de segmentation disponibles à la communauté des chercheurs, soulignant la nécessité de nouvelles méthodes d'analyse d'images qui seraient utile à la compréhension des maladies de la rétine comme le glaucome.

## C.2 Le Glaucome et la Biomécanique Oculaire

Le glaucome est une neuropathie optique multifactorielle, consistant en un groupe hétérogène d'affections qui normalement affectant les deux yeux et se manifeste par une apparence anormale du disque optique avec une perte lente de la sensibilité visuelle. Dans le glaucome primaire à angle ouvert (GAO), la forme la plus fréquente de glaucome, l'angle entre la cornée et l'iris reste ouvert, comme dans un œil sain, mais dans certains cas, il y a un écoulement lent de l'humeur aqueuse à travers le trabéculum, ce qui provoque une augmentation chronique de la PIO (Fig. 2.12).

Le GAO est reconnu comme une maladie progressive caractérisée par la perte des cellules ganglionnaires neurorétiniennes, courber les axones qui transportent l'information visuelle de la rétine au cerveau et par conséquent, provoquant des changements sur l'intégrité structurelle et fonctionnelle du nerf optique et de la lame criblée (LC).

Dans la plupart des yeux les axones ne remplissent pas le disque optique complètement, laissant une dépression physiologique en son centre appelée excavation

papillaire. Comme les fibres nerveuses meurent dans les patients atteints de glaucome, l'anneau neurorétinien s'amincit causant l'élargissement de l'excavation. Le rapport entre le diamètre de l'excavation papillaire et le diamètre total du disque est utilisé pour estimer le volume de tissu dans l'anneau neurorétinien [29]. Le rapport excavation-disque (C/D) normale est de 0,3 [30] tandis que dans le glaucome avancé il peut atteindre des valeurs proches de 1 [31]. L'excavation du disque est le résultat de l'effondrement mutuel des plaques consécutives du tissu conjonctif de la lame criblée et sa rotation au point d'insertion dans la sclère (Fig. 2.13).

Les principales causes de la neuropathie glaucomateuse restent inconnues, mais de gros efforts on été faits au cours des années pour tenter d'expliquer les mécanismes de la maladie résultant en deux principales théories: mécanique et vasculaire. La théorie mécanique met l'accent sur les dommages subis par les neurones du nerf optique lorsqu'ils traversent les pores de la lame criblée en raison de son incurvation ou l'effondrement causé par la PIO élevée, qui peut entraîner une ischémie provoquant la mort des cellules [45]. La théorie vasculaire suggère que les yeux avec intrinsèquement mauvais approvisionnement vasculaire du NO sont plus prédisposés aux dommages causés par une PIO normale ou élevée [46]. La différence entre ces théories a peu d'impact clinique puisque actuellement la réduction de la PIO, soit sur le plan pharmacologique ou chirurgical, est le seul traitement qui a été efficace pour ralentir la progression du glaucome [47],[48]. Le fait que dans certains groupes ethniques la majorité des patients atteints de GAO ont la PIO normale [49] et que la plupart des sujets avec PIO élevée (>21mmHg) ne développeront jamais la neuropathie glaucomateuse ou la perte de champ visuel [41] démontre que la compréhension de la maladie est insuffisante.

Par définition, la PIO est la force normale par unité de surface exercée par les liquides intraoculaires sur les tissus qui les contiennent. La réponse mécanique est fonction de la géométrie individuelle de l'œil, son anatomie et des propriétés mé-

caniques des tissus, des facteurs qui contribuent à déterminer la susceptibilité d'un individu à la PIO. Par conséquent, il est naturel de considérer que la biomécanique joue un rôle important dans la neuropathie glaucomateuse et le principal défi est alors de comprendre comment la combinaison de ces facteurs entraîne des lésions tissulaires.

Le nerf optique est une région d'intérêt biomécanique spéciale parce que c'est une discontinuité dans la coque cornéo-sclérale, et ce genre de discontinuités généralement donnent lieu à des concentrations de stress/déformation en systèmes mécaniques [51]. Il est soumis à l'action mécanique de la PIO, la tension de la sclérotique et la pression du liquide céphalo-rachidien et alors que la présence de ces forces est physiologique, son changement pourrait être pathologique et pourrait induire une déformation anormale des tissus. Malgré tous les progrès qui ont été réalisés, une grande partie de ce qui est connu sur les propriétés biomécaniques du NO, la LC et la sclère s'appuient sur l'examen histologique post-mortem [56]-[58], procédures invasives comme la canulation [59], et plus récemment sur des techniques d'imagerie statique in vivo [60], [61].

En raison de la complexité de l'étude in vivo des propriétés biomécaniques du NO et de la LC, la modélisation mathématique est devenue la méthode préférée pour effectuer une telle recherche. La recherche basée sur la modélisation par éléments finis a conduit á deux conclusions principales: 1) l'élasticité et l'épaisseur de la sclère peuvent être les déterminants les plus importants du stress et de la déformation du nerf optique, et 2) l'élévation de la PIO provoque les tissus du NO à être soumis à un environnement complexe de déformation dont la grandeur et la distribution varient à travers le nerf optique. Par ailleurs, les amplitudes les plus élevées de tous les modes de déformation (élongation, compression) se produisent dans les régions du tissu neural et non dans la lame criblée [65], comme on le croyait auparavant.

Afin d'avoir une meilleure compréhension de ce paradigme biomécanique et des forces qui causent des dommages au nerf optique et de tissu neural, c'est d'une im-

portance vitale d'avoir la capacité d'évaluer la biomécanique oculaire in vivo et de manière non invasive.

## C.3 Hypothèse

La choroïde a le débit sanguin le plus haut par gramme de tissu que tous les organes du corps humain étant 80% pulsatile [73]. Considérant le fait que ces pulsations conduisent la rétine vers l'avant alors qu'ils élargissent la sclère [74],[75], il est naturel de penser que les axones qui passent de la rétine et à travers la lame criblée pourraient donc être tendus en systole lorsque la rétine se déplace vers l'avant (Fig C.1). Par ailleurs, il a été constaté que les pulsations choroïdienne augmentent avec une PIO plus élevé [76] et une tension artérielle basse [77], deux grands facteurs de risque de glaucome.

Suivant ce raisonnement, nous émettons l'hypothèse que

> *La pulsatilité de la choroïde se traduirait par une déformation périodique des axones qui forment le nerf optique. L'ampleur de cette déformation dépendra des propriétés biomécaniques du tissu ainsi que de la pulsatilité de la choroïde et pourrait être liée à des lésions axonales et la perte de la couche des fibres nerveuses rétiniennes dans le glaucome.*

Par conséquent, la motivation de ce travail, ainsi que la cohorte de patients inclus dans cette étude vise à caractériser les changements dynamiques du fond de l'œil asociées à l'apparition et la progression du glaucome.

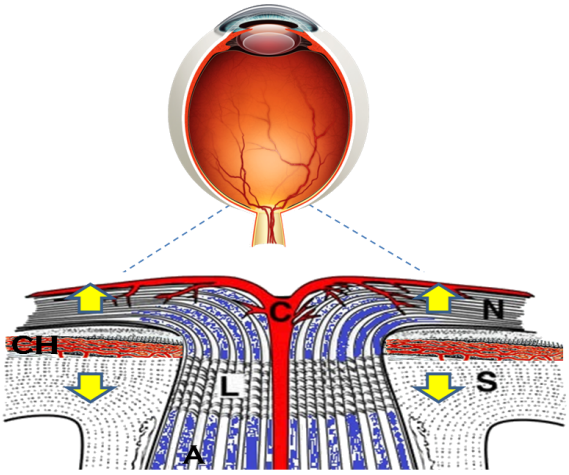


**Figure C.1 – Le remplissage de la choroïde par le débit sanguin provoque son expansion, poussant la rétine vers l'avant et la sclère vers l'arrière (flèches jaunes), qui se traduit par une déformation périodique des axones qui pourrait être corrélée avec des dommages dans le glaucome (C - artère centrale de la rétine, N - couche des fibres nerveuses, L - lame criblée, CH - choroïde, S - sclère, A - axon)**

## C.4 Objectifs de Recherche

Dans le contexte susmentionné et l'objectif d'avoir une meilleure compréhension de l'influence de la pulsatilité oculaire et sa relation avec les facteurs de risque de la pathologie glaucomateuse, l'objectif général de ce projet de recherche est d'étudier et de caractériser la dynamique du fond de l'œil ainsi que sa pertinence clinique à différents stades de la maladie en utilisant des séries d'images OCT acquises à vidéofréquence. Particulièrement:

- Conception de protocoles d'imagerie diagnostique qui permettent des mesures de déformation de la rétine et qui peuvent être implémentés en clinique.
- Développement d'algorithmes d'analyse d'image entièrement automatisés afin de quantifier le déplacement pulsatile du tissu dans le nerf optique.
- Recrutement de volontaires pour l'imagerie OCT.

- Caractérisation de la déformation de la rétine peripapillaire chez une cohorte de patients la plus représentative du spectre du glaucome.
- Étude de la relation entre le descripteur biomécanique proposé et les paramètres oculaires, vasculaires et démographiques obtenus lors de l'examen ophtalmologique.

## C.5 Étude Clinique

L'étude a une conception transversale et a été réalisée selon des protocoles approuvés par le comité de révision institutionnelle de l'hôpital Maisonneuve-Rosemont et son comité d'éthique. Le protocole de recherche suit les principes de la Déclaration d'Helsinki. Un consentement éclairé a été obtenu de tous les participants après que la nature et les conséquences possibles de l'étude ont été pleinement expliquées. Une seule visite est requise par sujet.

### C.5.1 Sujets

Des volontaires de 40 ans et plus ont été recrutés à la clinique de glaucome du département d'ophtalmologie de l'Hôpital Maisonneuve-Rosemont à Montréal. Un œil a été étudié par sujet. Des patients avec différents niveaux de progression de la neuropathie glaucomateuse ont été sélectionnés et classés comme suit:

- Glaucome précoce à angle ouvert (EOAG) - Modifications glaucomateuses typiques du bord du nerf optique; encoches de l'anneau neurorétinien, si présentes, non étendues au bord du disque, défaut moyen du champ visuel MD $> -6,0dB$, pas de chirurgie antérieure du glaucome par incision, aucune restriction de la PIO.

- Suspicion de glaucome à angle ouvert (OAG-S) - Disque optique suspect de glaucome, c.-à-d., rapport excavation-disque vertical ne dépassant pas 0,8, pas d'éntendues, hémorragie de flamme ou défaut focal de la couche fibreuse rétinienne, champ visuel normal, aucune restriction de PIO.

- Hypertension oculaire (OHT)- Antécédents de PIO $> 24mmHg$ au moins deux occasions, champ visuel normal, disque optique normal et aucun signe de progression.

- Normal - Sujets appariés selon l'âge ayant des yeux sains, c'est-à-dire, avec une PIO$\leq$ $21mmHg$, champ visuel normal, NO sain avec aucune caractéristique suspecte du glaucoma et sans antécédents de glaucome.

### C.5.2 Protocole

Dans le but de mesurer avec exactitude les déplacements du tissu rétinien au cours du cycle cardiaque en temps réel, un dispositif de SD-OCT a été utilisé pour l'imagerie (Spectralis OCT Plus [1] , Heidelberg Engineering, Germany), le logiciel a été modifié pour enregistrer des séries d'images vidéofréquence permettant l'exportation des images brutes, y compris un fichier de langage d'étiquetage extensible (XML) qui contient les paramètres d'imagerie ainsi que l'horodatage de chacune des images acquises. Cette dernière information est indispensable pour effectuer des calculs de fréquence de mouvement liés au cycle cardiaque puisque l'appareil est équipé d'un système d'eye-tracker qui stoppe l'acquisition, pour éviter les artefacts de mouvement, lorsque la zone balayée ne correspond pas à la position de référence.

La première étape du protocole correspond à l'imagerie OCT du nerf optique. Des scans de la même région du nerf optique sont acquis à $20Hz$ pendant 20 secondes.

[1]Spécifications de l'appareil - SLD: $\lambda_c = 870nm, \Delta\lambda \simeq 47.7nm$; Scan profondeur dans les tissus: $1.9mm$; Taux maximal de A-scan: $40kHz$, Résolution numérique: $3.9\mu m$ axialement et $6\mu m$ latéralement.

Chaque série se compose de 401 images à haute résolution (496 x 768 pixels) acquises sur un champ de vision de 15º (5$mm$ environ) (Fig. C.2). En raison de la nécessité d'un taux d'acquisition plusieurs fois supérieur à la fréquence cardiaque, la qualité doit être sacrifiée pour y parvenir, et le nombre maximum de B-scans qui peuvent être moyennés pour générer l'image finale est limité à deux. Avec la série d'images, le pouls du sujet à l'examen est enregistré avec un oxymètre de pouls fait maison, grâce à une interface dans LabView qui permet sa visualisation en temps réel. Cette information sera utilisée dans l'analyse subséquente pour déterminer la fréquence du cœur.

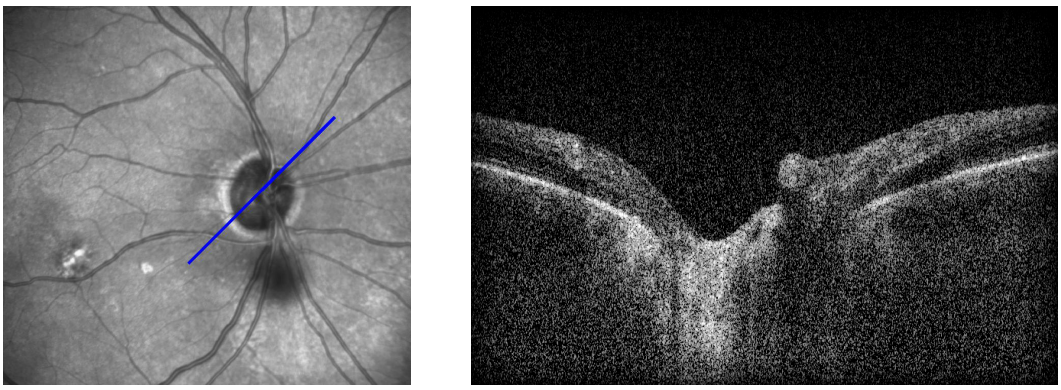

(a) (b)

**Figure C.2 – Paire d'images typiques de la série. a) Image de fond d'un œil droit montrant la ligne scannée à travers du nerf optique, dans ce cas à 45º par rapport à l'axe fovéa-disque. b) Image de tomographie par cohérence optique correspondante conforme par deux B-scans moyennées.**

Immédiatement après l'imagerie, tous les participants subissent un examen de la vue standard. La pression intraoculaire (PIO) et l'amplitude de pulsation oculaire (OPA) sont mesurées avec un tonomètre dynamique de contour PASCAL (Ziemer Ophthalmic Systems AG). L'analyseur de réponse oculaire (ORA, Reichert Ophthalmic Instruments) est utilisé pour mesurer l'hystérésis cornéenne (CH), le facteur de résistance cornéen (CRF) et l'épaisseur cornéenne centrale (CCT). La longueur axiale (AL) est déterminée à l'aide d'un biomètre optique IOLMaster (Carl Zeiss Meditec AG). Une mesure de pression artérielle brachiale réalisée avec un tensiomètre

automatique (Spot Vital Signs NIBP, Welch Allyn Inc.) est également incluse dans l'examen. Les pressions artérielles systolique et diastolique (SBP, DPB) sont utilisées pour calculer 1) la pression artérielle moyenne MAP = DBP + 1/3 ( SBP-DBP); 2) la pression oculaire de perfusion moyenne MOPP = 2/3 MAP - PIO; 3) la pression de perfusion systolique SPP = SBP - PIO, et 4) la pression de perfusion diastolique DPP = DBP - PIO. Finalement, les variables liées à la gravité du glaucome sont extraites du dossier médical ophtalmique du patient.

## C.6 Segmentation Automatique du Nerf Optique et Analyse de la Déformation Pulsatile

L'approche proposée consiste à délimiter avec précision la rétine péripapillaire et le nerf optique, c'est-à-dire la membrane limitante interne (ILM), sur les images OCT et suivre la position de régions spécifiques dans le temps, afin de quantifier le déplacement de la rétine. Toutes les routines d'analyse décrites ci-après ont été programmées dans Matlab (The MathWorks, Inc.).

### C.6.1 Prétraitement

Afin de préparer les images pour la segmentation, une séquence de prétraitement est requise. La première étape consiste à appliquer un filtre médian 2D de taille 7x7 pixels pour la suppression du bruit speckle. Pour l'alignement, pour corriger les déplacements brusques de tissus entre les images, la fonction d'enregistrement automatique des images de Matlab basée sur l'intensité de l'image a été utilisée avec une transformation rigide, consistant en la traslation et la rotation, prenant comme référence la première image acquise.

Après l'alignement, les images sont soumises à une technique d'amélioration du contraste en deux étapes pour supprimer les caractéristiques qui peuvent conduire à une détection de limite erronée (voir la Fig. C.3). D'abord, l'exponentiation d'intensité est appliquée ($I(z)^2$), suivie de l'exponentiation + compensation d'atténuation [83] en utilisant la formule $I_c = \frac{I^3(z)}{2\int_z^\infty I^3(u)du}$ (avec $I_c$ l'image compensée avec le contraste amélioré et $I(z)$ l'image originale)

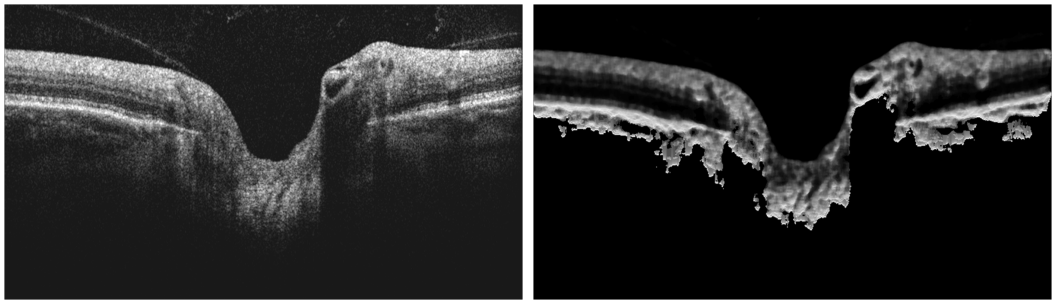

(a) (b)

**Figure C.3 – Exemple de prétraitement: a) Image du NO original montrant des décollements du vitré sur les deux régions, nasale et temporale. b) Même image après le filtrage médian et les étapes d'amélioration du contraste appliquées.**

### C.6.2 Segmentation de la Membrane Limitante Interne

Afin de séparer la couche externe de la rétine et le vitré, un filtre médian (7x7 pixels) est appliqué. L'étape suivante consiste à obtenir l'image binaire correspondante en définissant un seuil d'intensité de 10% de l'intensité maximale de l'image; comme prévu, l'image résultante a des aspérités et des ponts qui sont supprimés en appliquant une fermeture morphologique avec un élément structurant carré de 3 pixels de largeur (Fig C.4b). L'étiquetage des pixels de huit objets connectés est ensuite utilisé pour supprimer les pixels parasites restants dans le vitré en conservant les objets qui contiennent plus de 1000 éléments.

L'ILM est définie sur le pixel de premier plan de chaque A-scan. Pour exclure les points mal répartis sur les bords de la papille optique, les distances dans la direction

axiale entre les points de contour adjacents $c(x)$ sont calculées: $\Delta z_i = c(x_i + 1) - c(x_i)$, et nous cherchons les distances de $|\Delta z|$ qui sont égales ou supérieures à $27\mu$m. Lorsqu'une valeur négative ciblée est suivie d'une valeur positive ciblée et séparée par un maximum 10 points dans la direction transversale ($x$), cet intervalle est supprimé et remplacé par une interpolation. La Figure C.4c affiche le profil segmenté.

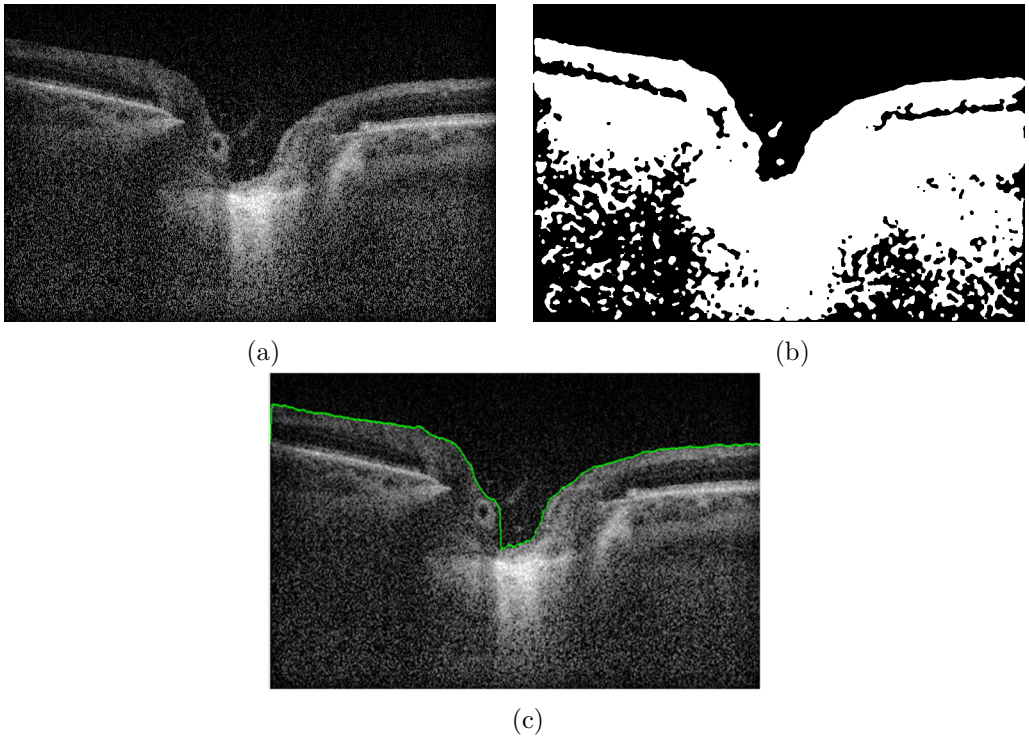

(a) (b)

(c)

**Figure C.4 – Exemple de certaines étapes de segmentation: a) Image originale. b) Image binaire après fermeture morphologique. c) Profil final d'ILM, le bord est détecté comme le premier pixel différent de zéro dans chaque A-scan et interpolé.**

Le résultat de la segmentation est un ensemble de 401 profils d'ILM par série d'images. Dans le but d'éliminer automatiquement les profils où la délimitation ILM a échoué, tous les profils sont alignés dans la direction axiale en prenant comme référence le point le plus profond de l'excavation (Fig. C.5a), la moyenne et l'écart-type (SD) des valeurs de profondeur ($z$) à chaque position du A-scan sont calculées aussi. Les valeurs aberrantes sont ensuite marquées en deux étapes.

Tout d'abord, nous identifions les pixels aberrants dans chacun des profils, définis

comme les points situés à une distance de 3 écart-types ou plus de la valeur moyenne dans chaque A-scan. Ensuite, l'écart-type du nombre de pixels aberrants par profil est déterminé, et les profils avec plus de valeurs aberrantes que celui-ci sont rejetés. La Figure C.5b montre les profils finaux qui vont être utilisés dans l'analyse.

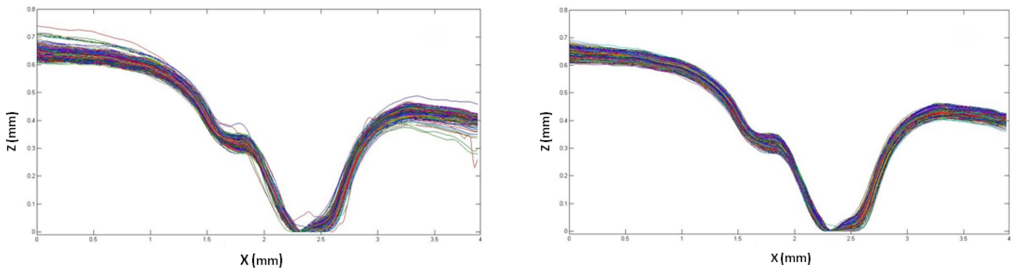


(a) (b)

**Figure C.5 – a) Profils résultant de la segmentation de la série d'images tracées ensemble après un décalage vertical. Certains profils montrent une segmentation inexacte au fond de l'excavation ou de la rétine péripapillaire, d'où l'identification en deux étapes des profils aberrants. b) Profils finaux après le processus d'élimination des profils aberrants.**

### C.6.3 Analyse de la Déformation

Une fois que les profils ILM finaux sont obtenus, la déformation rétinienne peut être déterminée à partir de la série d'images en quantifiant les changements de la distance mesurée entre la rétine péripapillaire et le tissu rétro-laminaire (distance PPR-PLT). Trois régions de 200$\mu$m sont sélectionnées le long du côté temporal pour effectuer les mesures ($T$, $T2$ et $T3$) à partir de l'ouverture de la membrane de Bruch et séparées par 160$\mu$m, comme indiqué sur la Figure C.6. Les distances sont moyennées dans chaque région, ce qui donne trois valeurs PPR-PLT par image. Finalement, la déformation rétinienne neuro-péripapillaire (N-PP) dans chaque région est définie comme l'écart type des distances PPR-PLT de toutes les images $DT, DT2$ et $DT3$.

Puisque la fluctuation de la distance PPR-PLT dans chacune des régions a montré un comportement très similaire, la moyenne des trois valeurs de déformation

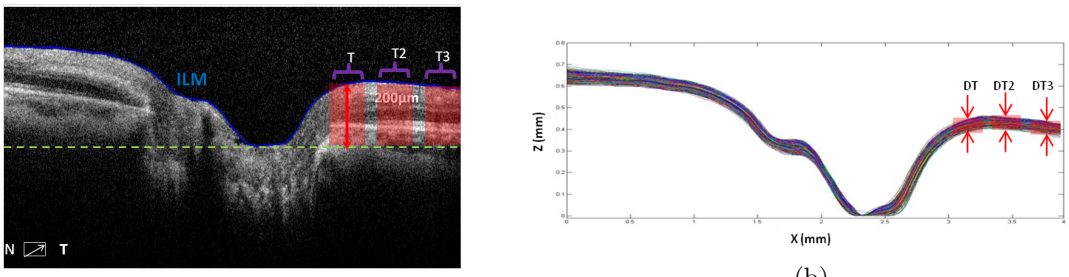


(a) (b)

**Figure C.6 – Mesures de déformation: la ligne verte en a) définit la référence au point le plus profond du NO et la flèche rouge représente la distance PPR-PLT mesurée pour déterminer la déformation rétinienne neuro-péripapillaire. Trois valeurs de distance PPR-PLT sont calculées par image, correspondant aux régions $T$, $T2$ et $T3$. b) La déformation est définie comme l'écart-type des distances PPR-PLT de tous les profils dans chacune des régions (rectangles rouges).**

($DT, DT2$ et $DT3$) est calculée et prise comme la déformation rétinienne N-PP final. Pour assurer que la déformation rétinienne N-PP observée est principalement causée par la pulsatilité du flux sanguin, et comme l'horodateur de chacune des images est connu, le spectre de fréquence du déplacement rétinien mesuré est comparé à celui correspondant au signal de l'oxymètre comme dernière étape de l'algorithme. Les résultats de déformation sont rejetés s'il n'est pas possible d'identifier la fréquence cardiaque dans le spectre des distances PPR-PLT.

La reproductibilité de la méthode a été évaluée en mesurant la déformation rétinienne N-PP à plusieurs reprises sur onze sujets choisis au hasard. Un coefficient de corrélation intraclasse (ICC) de 0,86 a été obtenu avec des intervalles de confiance [0,55,0,96] à $\alpha = 0,05$.

## C.7 Déformation Pulsatile de la Rétine Neuro-Péripipillaire dans le Glaucome

Afin d'étudier la relation entre la déformation rétinienne due à la pulsatilité et l'endomma-gement causé par le glaucome, la déformation rétinienne N-PP est caractérisée dans 11 patients OHT, 17 OAG-S sans médicament de glaucome, 24 EOAG et 18 volontaires en bonne santé.

Deux séries d'images OCT sont obtenues par sujet, à $45^{o}$ et à $135^{o}$ par rapport à l'axe fovéa-disque, correspondant aux zones d'endommagement majeures dans le glaucome. Tous les yeux sont transformés en format œil-droit. Les séries d'images enregistrées ont été exclues en raison de problèmes de fixation, d'images de mauvaise qualité ($Q < 10$ pour la plupart des images), de gros vaisseaux sanguins régissant le mouvement du tissu neurorétinien et d'incapacité à identifier la fréquence cardiaque dans le spectre des distances. L'analyse de variance suivie par le test post hoc HSD de Tukey pour les comparaisons multiples a été utilisée et les valeurs de $p < 0,05$ ont été considérées statistiquement significatives.

### C.7.1 Comparaison de la Déformation N-PP

Les résultats obtenus pour les deux régions étudiées sont affichés dans la Fig. C.7 sous forme de boîtes à moustaches. À la région inférotemporal, le groupe Normal présentait une déformation significativement plus élevée ($4,8 \pm 1 \mu m$) que les groupes OHT ($3,5 \pm 0,3 \mu m$, $p = 0,015$), OAG-S ($3,8 \pm 0,8 \mu m$, $p = 0,045$) et EOAG ($3,2 \pm 0,7 \mu m$, $p < 0,001$). Le groupe OAG-S était également significativement différent du groupe EOAG ($p = 0,0375$) lorsque la comparaison était effectuée séparément. D'autre part, la déformation N-PP superotemporal ne montre pas de différences significatives entre les quatre groupes ($p = 0,139$). Ce résultat peut s'expliquer en partie par le fait que

la perte du bord neurorétinien commence le plus souvent à la région inférotemporal, étant la plus affectée au cours de l'évolution de la neuropathie glaucomateuse [32].

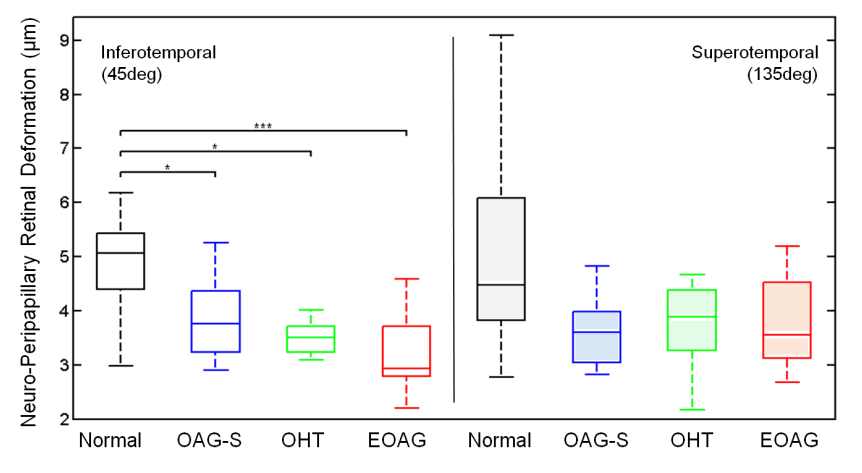


**Figure C.7 – Comparaison des valeurs de déformation rétinienne N-PP entre les quatre groupes pour les deux régions étudiées (OAG-S: suspicion de glaucome à angle ouvert, OHT: hypertension oculaire, EOAG: glaucome précoce à angle ouvert). Les différences statistiques significatives sont représentées avec les critères suivants:** $*p < 0.05$**,** $**p < 0.01$ **et** $***p < 0.001$**.**

Le Tableau 6.1 contient les données démographiques par diagnostic ainsi que les valeurs de déformation moyennes pour les deux régions.

Afin de comprendre comment cette déformation est liée aux autres paramètres oculaires, vasculaires et démographiques qui ont été inclus dans l'analyse, la corrélation de Pearson a été réalisée ainsi que l'analyse de régression linéaire multiple. Chaque groupe a été analysé séparément.

## C.7.2 Régression Linéaire

### Groupe Normal

Dans ce cas, l'analyse de corrélation linéaire a montré que les yeux avec des cornées plus minces ont tendance à avoir une déformation superotemporal plus grande que les yeux avec des cornées plus épaisses ($r = -0,62, p = 0,045$).

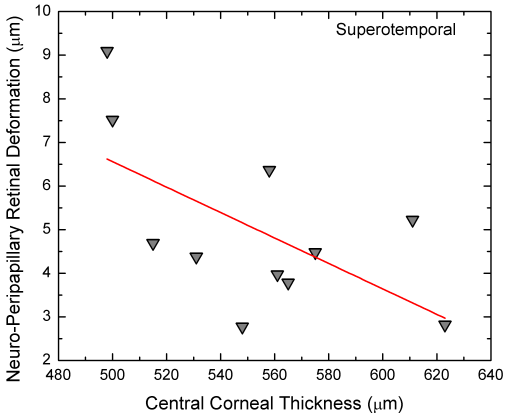


**Figure C.8 – Régression linéaire pour la déformation N-PP superotemporale vs CCT dans les yeux normaux ($R^2 = 0,3063$.)**

### Suspicion de Glaucome

Dans le groupe OAG-S la hystéresis cornéenne basse et la RNFL péripapillaire plus épaisse étaient liées à une déformation inférotemporal plus grande ($r = -0,66, p = 0,036, r = 0,95, p = 0,004$). D'autre part, la déformation superotemporal a tendance à augmenter avec DPP ($r = 0.69, p = 0.027$). (voir la Fig. C.9)

### Hypertension Oculaire

Pour la région inferotemporal, des amplitudes plus élevées de l'OPA et des MD moins négatifs (plus normaux) ont été corrélées avec une déformation N-PP plus grande ($r = 0,855, p = 0,030, r = 0,921, p = 0,009$). Le rapport vertical excavation-disque a montré une signification limite, où moins de déformation inférotemporal était liée à une plus grande sévérité du glaucome ($r = -0,805, p = 0,053$). Pour la région superotemporal, les yeux avec de petites valeurs de CRF étaient associés à une plus grande déformation ($r = -0,984, p = 0,002$). Les graphiques correspondants sont montrés dans la Figure C.10.

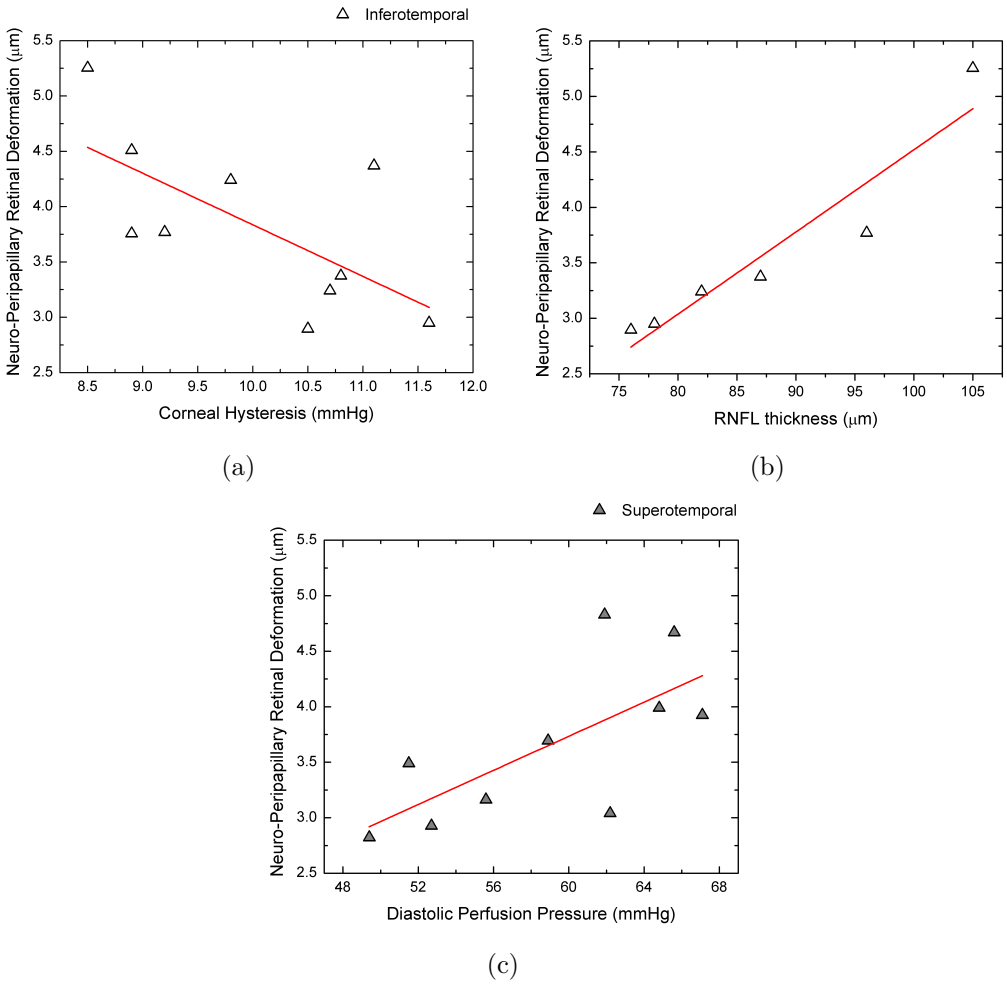


**Figure C.9 – Analyse de régression linéaire pour le groupe OAG-S: a) Déformation inférotemporelle vs CH ($R^2 = 0,372$); b) Déformation inférotemporelle vs épaisseur moyenne de la couche de fibres nerveuses rétiniennes péripapillaires autour du nerf optique ($R^2 = 0,870$); c) Déformation superotemporelle vs DPP ($R^2 = 0,412$).**

La régression linéaire multiple n'a trouvé qu'un prédicteur significatif par région:

$$N - PP_{InferoT} = 3.7176 + 0.17568MD, \tag{C.1}$$

$$N - PP_{SuperoT} = 6.3433 - 0.24237CRF, \tag{C.2}$$

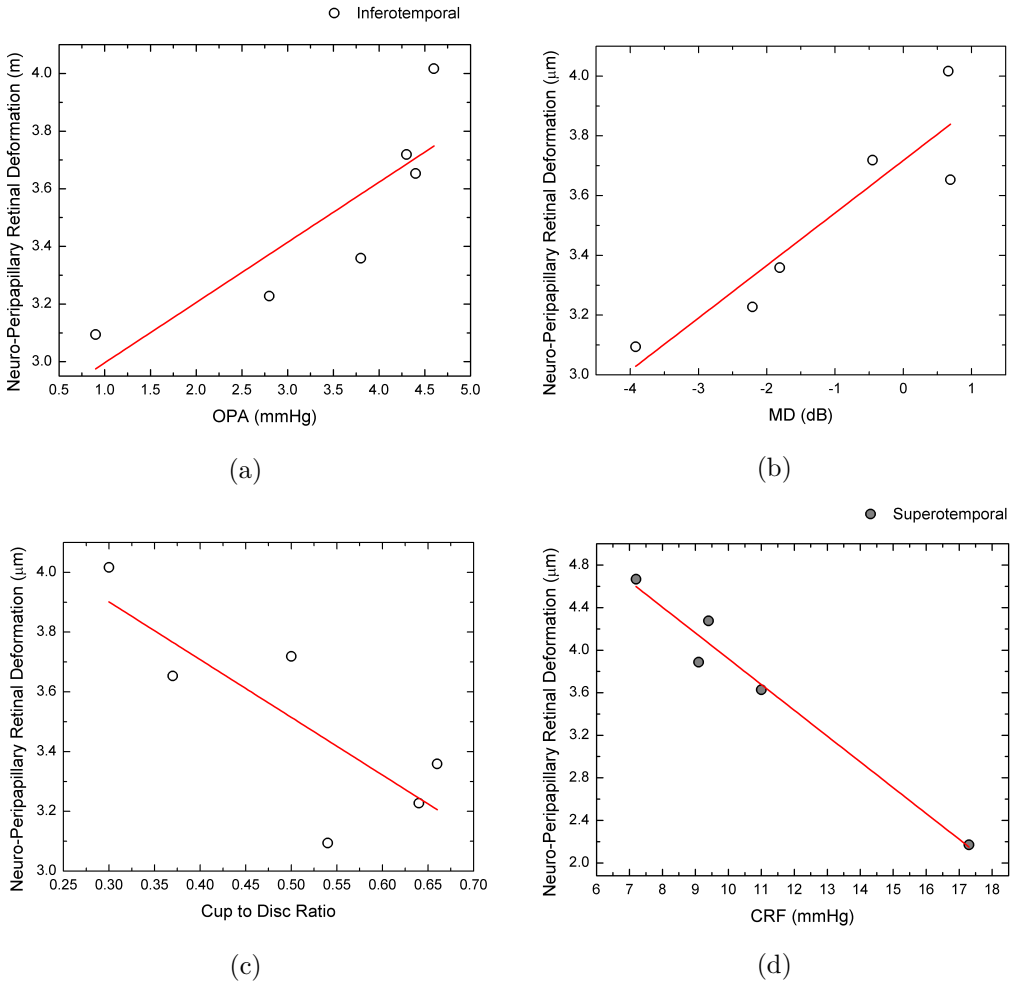


**Figure C.10 – Analyse de régression linéaire pour le groupe OHT: a) Déformation inférotemporelle vs amplitude de pulsation oculaire ($R^2 = 0.664$); b) Déformation inférotemporelle vs défaut moyen du champ visuel ($R^2 = 0,810$); c) Déformation inférotemporelle vs vertical C/D ($R^2 = 0,561$) and d) Déformation superotemporelle vs factor de résistance cornéen ($R^2 = 0,960$).**

### Glaucome Précoce à Angle Ouvert

Dans ce groupe une plus grande déformation inférotemporal était associée à des cornées plus minces ($r = -0,54, p = 0,046$), tandis qu'une déformation superotemporal majeure était corrélée avec des DPPs plus bas ($r = -0,564, p = 0,018$), des amplitudes oculaires plus grandes ($r = 0,53, p = 0,028$) et des valeurs de PIO plus élevées ($r = 0,49, p = 0,045$) comme le montre la Figure C.11 .

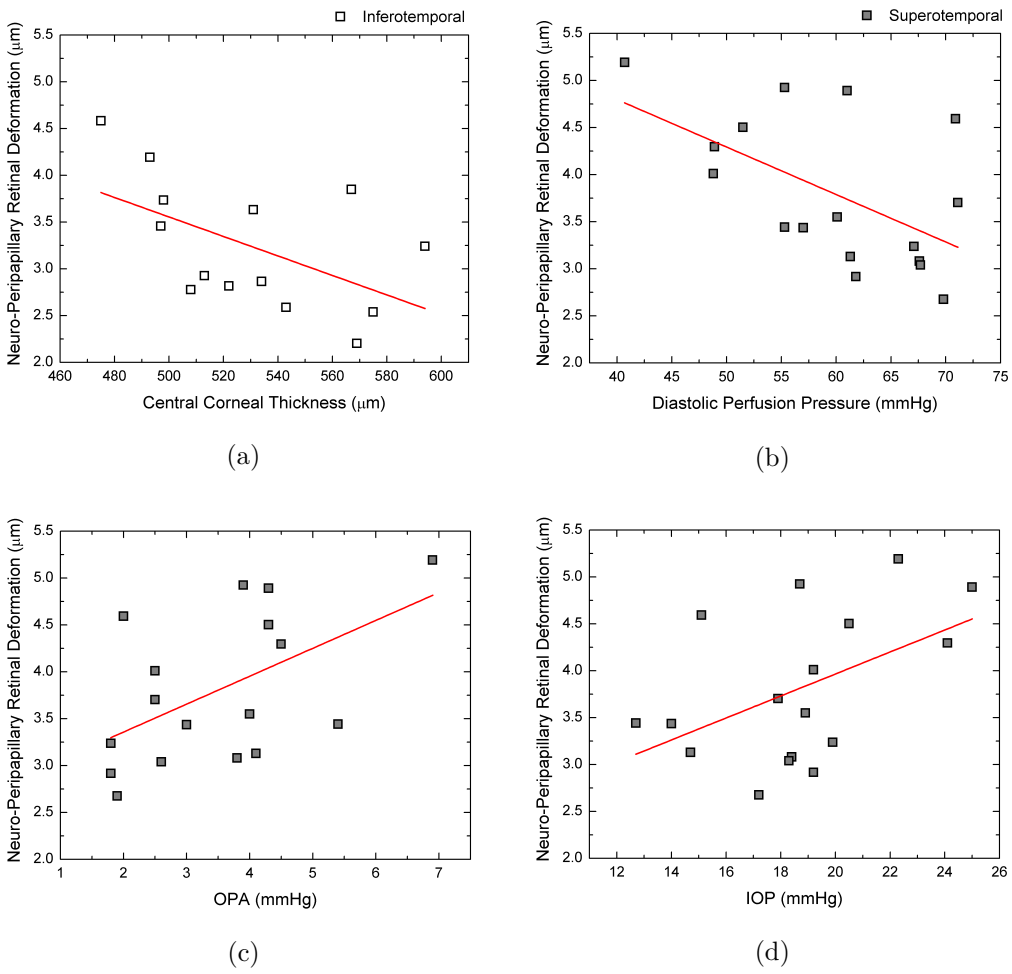


**Figure C.11 – Analyse de régression linéaire pour le groupe EOAG: a) Déformation Inférotemporelle vs CCT ($R^2 = 0,233$); b) Déformation superotemporelle vs DPP ($R^2 = 0,272$); c) Déformation superotemporelle vs amplitude de pulsation oculaire ($R^2 = 0.234$) et d) Déformation superotemporelle vs pression intraoculaire ($R^2 = 0,192$).**

Dans ce cas, l'analyse de régression multiple a abouti à un modèle pour la déformation rétinienne inférotemporal N-PP avec deux prédicteurs. Malgré le fait que la CCT a montré une corrélation significative, seulement le IOP et le PSP avaient des effets partiels significatifs dans le modèle complet:

$$N - PP_{InferoT} = 4.8371 - 0.21339IOP + 0.019232SPP. \tag{C.3}$$

Le modèle a pu expliquer les 76,7% de la variance de la déformation ($p = 0,0007$). La Figure C.12b illustre la relation entre la PIO, SPP et la déformation rétinienne N-PP inférotemporal dans le groupe EOAG.

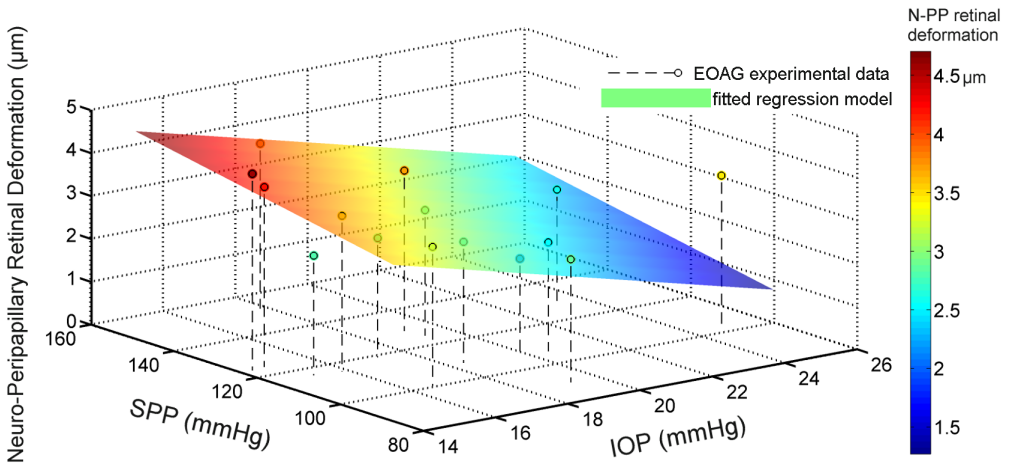


(a)

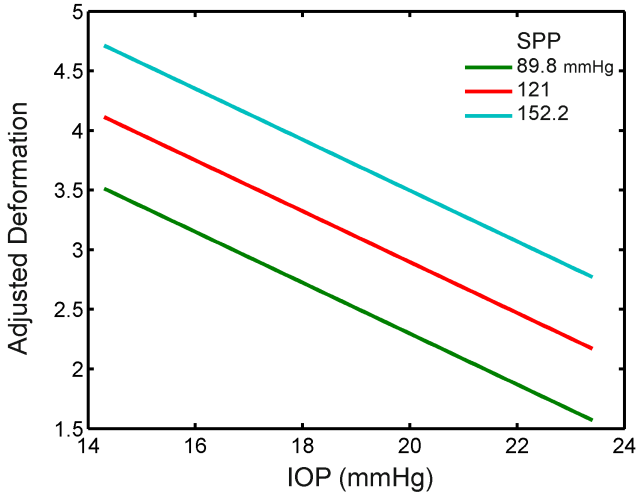


(b)

**Figure C.12 – Modèle linéaire ajusté pour la déformation rétinienne neuro-peripapillaire inférotemporal dans le groupe EOAG avec PIO ($\beta = -0,21339, p = 0,0006$) et SPP ($\beta = 0,019232, p = 0,0194$) comme prédicteurs ($R^2 = 0,767, p < 0,001$). a) Données expérimentales (points colorés) et plan de la régression ajusté correspondant à l'équation (C.3). La barre de couleur indique le mappage des valeurs de déformation comprises entre $1,25\mu m$ (bleu foncé) et 4,75 $\mu m$ (rouge foncé). b) Graphique d'interaction entre PIO, SPP et la déformation rétinienne N-PP selon le modèle. Le graphique montre que la quantité de déformation rétinienne N-PP Inférotemporal diminue à la fois avec un SPP faible et une PIO élevée, deux facteurs de risque majeurs dans le glaucome.**

## C.8 Déformation Pulsatile de la Rétine Périfovéolaire dans le Glaucome

Une des particularités de l'algorithme de segmentation développé dans ce travail est qu'il peut être appliqué directement aux images OCT maculaires pour délimiter l'ILM sans aucune modification. Profitant de cette caractéristique, une étude préliminaire pour étudier la déformation rétinienne autour de la macula a été réalisée en utilisant des séries d'images OCT qui ont été acquises au cours d'une étude pour déterminer la rigidité oculaire [72].

Onze patients atteints de glaucome à angle ouvert, 22 EOAG et 34 volontaires en bonne santé ont été étudiés. Dans ce cas, les scans sont acquis à $8Hz$ (mode haute vitesse) pour $50s$ en utilisant l'imagerie de profondeur améliorée (EDI) et l'angle de scan est choisi pour maximiser la visibilité de la choroïde pour chaque sujet. Chaque série est composée de 401 images (5 B-scans moyennés par image) acquises sur un champ de vision de $30^o$ qui correspond à $\approx 8mm$ (voir la Fig. C.13).

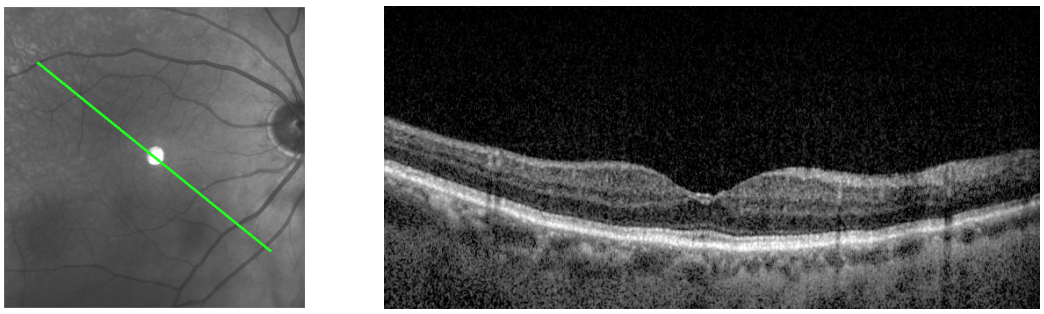

(a) (b)

**Figure C.13 – Paire typique d'images utilisées pour déterminer la rigidité oculaire et la déformation rétinienne autour de la macula. a) Image de fond d'un œil droit montrant la ligne scannée à travers la macula, dans ce cas à $141^o$ par rapport à l'axe fovéa-disque. b) Image de tomographie par cohérence optique correspondante avec cinq images moyennées.**

À cette occasion, au lieu d'utiliser le point le plus profond de l'excavation dans le nerf optique, le centre de l'umbo est utilisé comme référence pour mesurer la distance

axiale. Une région de $600\mu m$ située dans la zone périfovéolaire a été choisie de chaque côté de la fovéa pour mesurer le déplacement rétinien dans le temps (voir la Fig. C.14). Seules les séries d'images avec des résultats de rigidité oculaire ont été analysées.

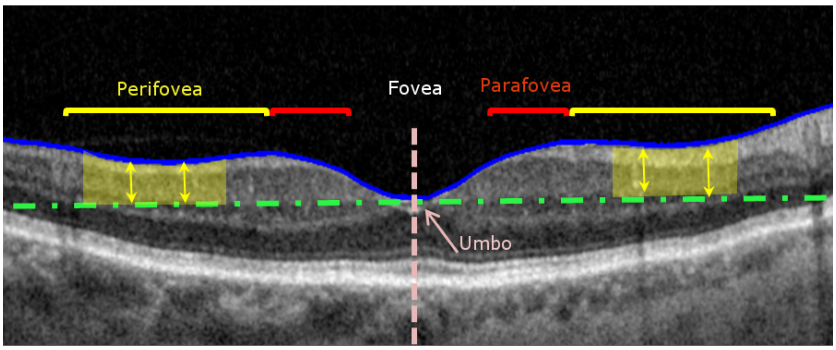


**Figure C.14 – Mesure du déplacement rétinien périfovéolaire: La distance axiale moyenne entre la rétine périfovéolaire et la référence située au centre de l'umbo (ligne verte) est calculée des deux côtés de la fovéa pour déterminer la déformation.**

Puisque le déplacement de la rétine de chaque côté de la fovéa a montré un comportement très similaire et qu'il n'y avait pas de différence entre les deux valeurs de déformation rétinienne périfovéale (PFR), les résultats présentés dans ce qui suit correspondent à la valeur moyenne des deux régions.

### C.8.1 Comparaison de la Déformation PFR

Les résultats obtenus pour les trois groupes étudiés sont présentés dans la Figure C.15 sous forme de boîtes à moustaches. La déformation rétinienne périfovéolaire moyenne s'est avérée plus grande chez les yeux en bonne santé ($2{,}23\pm0,57\mu m$) que chez les yeux avec EOAG ($2{,}00\pm0,28\mu m, p = 0,039$). Aucune différence statistique n'a été trouvée entre le groupe normal et l'OAG ($2,27 \pm 0,39\mu m, p = 0,948$). La Table 7.1 contient les données démographiques ainsi que les valeurs moyennes de la déformation rétinienne périfovéolaire par diagnostic.

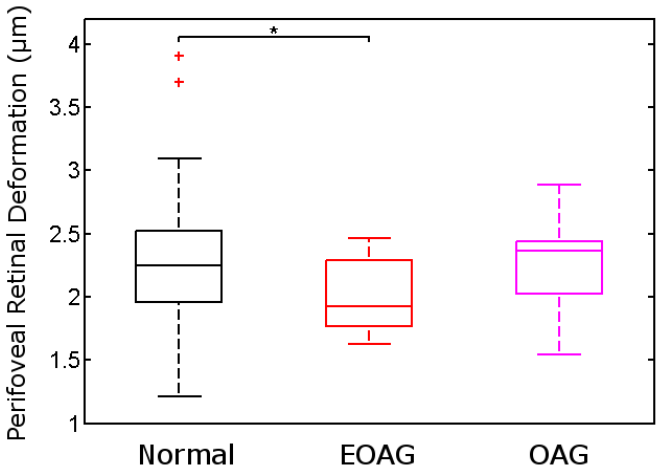


**Figure C.15 – Comparaison des valeurs de la déformation rétinienne périfovéolaire entre les trois groupes étudiés (EOAG: glaucome précoce à angle ouvert, OAG: glaucome à angle ouvert). La seule différence significative a été trouvée entre les yeux normaux et l'EOAG ($p = 0,039$); Normal - OAG ($p = 0,948$), EOAG - OAG ($p = 0,268$).**

## C.8.2 Régression Linéaire

Des yeux normaux avec des changements plus importants du volume oculaire ($r = 0,412, p = 0,016$) et des yeux plus élastiques (OR: $r = -0,409, p = 0,016$) ont présenté une déformation rétinienne périfovéolaire plus importante (Fig. C.16). Aucun autre groupe n'a montré de corrélation significative avec la déformation PFR.

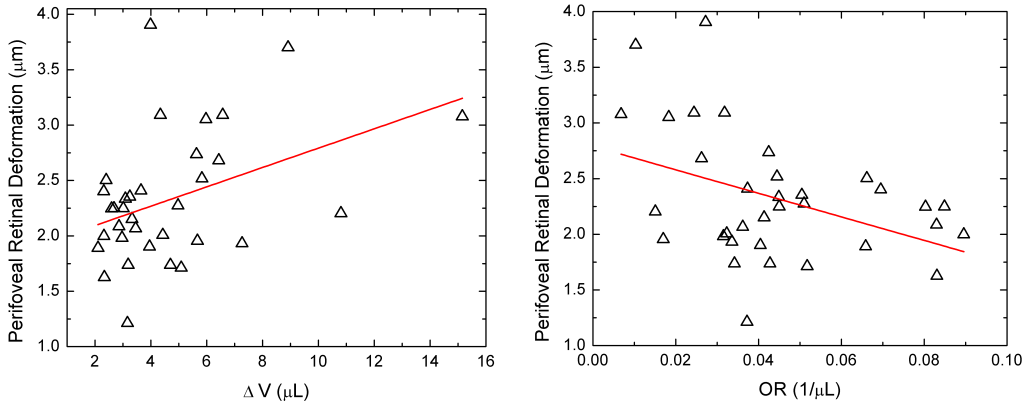


(a) (b)

**Figure C.16 – Analyse de régression linéaire pour le groupe Normal: a) Déformation rétinienne périfovéolaire vs le changement de volume oculaire ($R^2 = 0,144$); b) Déformation PFR vs la rigidité oculaire ($R^2 = 0,209$).**

Dans l'analyse de régression multiple, la rigidité oculaire était le seul paramètre statistiquement significatif à prédire la variance de la déformation PFR chez les yeux sains ($R^2 = 0,209, p = 0,028$):

$$PFR_{healthy} = 2.9556 - 14.346OR. \tag{C.4}$$

## C.9 Conclusions

La biomécanique joue un rôle essentiel dans un nombre important de maladies ophtalmiques comme le glaucome. La principale préoccupation dans la recherche biomécanique oculaire est la capacité de démontrer que les propriétés biomécaniques des tissus oculaires peuvent être mesurées in vivo, et même plus, de manière non invasive. De plus, puisque le but de la biomécanique oculaire est d'élucider la physiologie et la physiopathologie de l'œil, des études dynamiques sont également nécessaires, de préférence non invasives, qui peuvent être transférées à la clinique à un moment donné afin de suivre l'évolution des patients pendant le développement de la maladie. Cependant, la majorité des études trouvées dans la littérature sont statiques, mesurant les déplacements et les déformations de tissus à partir d'un petit ensemble d'images OCT, souvent 2 ou 3, faites de centaines de B-scans moyennés [116] - [119].

Mettant l'accent sur cela, l'objectif principal de ce project de recherche était de concevoir une méthode pour mesurer la déformation rétinienne pulsatile in vivo, de manière non invasive, afin d'étudier sa pertinence en tant que nouveau descripteur biomécanique oculaire et sa relation avec les facteurs de risque potentiels de la neuropathie glaucomateuse.

Afin de quantifier la déformation rétinienne, un algorithme entièrement automatisé pour segmenter la membrane limitante interne dans le NO et pour calculer les

déplacements de tissus péripapillaires à partir d'une série d'images OCT acquises á vidéofréquence a été développé. La méthode de segmentation est basée sur des opérations morphologiques et comprend une technique d'amélioration du contraste en deux étapes, conçue pour éliminer les corps flottants dans le vitré, compenser les inhomogénéités dues aux vaisseaux sanguins rétiniens et affiner les bords. Il a été démontré que l'approche proposée est capable de segmenter précisément l'ILM même lorsque les images montrent une quantité importante de bruit de speckle ou d'ombrage, ce qui est typique des taux d'acquisition élevés, s'est avéré très robuste lorsqu'il s'agit d'images avec un signal faible. En outre, il détecte avec précision la membrane limi-tante interne dans les yeux sains ainsi que dans plusieurs stades de la pathologie glaucomateuse, ce qui est d'une importance vitale dans les applications cliniques, avec les avantages d'une implémentation facile et un temps de calcul réduit.

L'analyse consiste à utiliser les profils ILM segmentés pour mesurer les changements de la distance axiale entre la rétine péripapillaire temporal et le tissu rétrolaminaire en raison de la pulsatilité choroïdienne. La déformation rétinienne neuro-péripapillaire est définie comme l'écart-type des distances mesurées sur les 400 images de la série. Pour s'assurer que la déformation mesurée est principalement provoquée par la pulsatilité du flux sanguin, le spectre des distances rétiniennes dans le temps est calculé et comparé à celui correspondant au signal de l'oxymètre. La reproductibilité de la méthode a été démontrée en obtenant un ICC de 0,86 ($\alpha = 0,05$).

L'application d'une telle méthodologie à quatre groupes cliniques a montré que les yeux atteints d'OAG précoce ($3,2 \pm 0,7\mu m, p < 0,001$), l'OAG-S ($3,8 \pm 0,8\mu m, p = 0,045$) et l'OHT ($3,5 \pm 0,3\mu m, p = 0,015$) ont une déformation N-PP inférotemporal significativement plus petite que celle des yeux sains ($4,8 \pm 1\mu m$). CCT, OPA et DPP se sont avérés être liés à la déformation rétinienne N-PP pour plus d'une cohorte. En ce qui concerne les paramètres qui indiquent l'état du glaucome, les yeux ayant un rapport vertical excavation-disque plus grand, le RNFL péripapillaire plus mince et le

MD du champ visuel plus grand, présentaient une déformation N-PP rétinienne plus petite. L'analyse multivariée a montré que la déformation rétinienne N-PP infero-temporal dans le groupe EOAG peut être décrite par une combinaison linéaire de la pression intraoculaire et de la pression de perfusion systolique, deux prédicteurs majeurs de la progression du glaucome.

Profitant du fait que l'algorithme d'analyse peut être facilement appliqué aux images OCT de la région maculaire, les changements dans la distance axiale entre la rétine périfovéolaire et la position verticale du centre de l'umbo ont été quantifiés pour déterminer la déformation. Les résultats ont montré que malgré l'absence de différence significative entre les groupes dans l'épaisseur choroïdienne, le changement de volume ou le coefficient de rigidité, la déformation rétinienne périfovéolaire était plus petite dans les yeux avec EOAG $(2,00 \pm 0,28 \mu m, p = 0,039)$ comparée aux yeux sains $(2,23 \pm 0,57 \mu m)$, ce qui indique que les propriétés matérielles du tissu rétinien maculaire pourraient être significativement altérées par la maladie. Une corrélation positive entre la déformation PFR et le changement du volume oculaire a été observée pour le groupe Normal, ce qui corrobore le fait que la déformation observée est induite par le flux sanguin pulsatile choroïdien. En outre, le fait que les yeux plus élastiques montrent une déformation PFR plus grande suggère qu'une cornée-sclère élastique pourrait absorber une partie du changement de volume en se dilatant, conduisant à de plus petites variations pulsatiles de PIO et une force pulsatile réduite sur les couches rétiniennes.

Dans un aperçu général, les résultats obtenus suggèrent que la déformation observée (N-PP et PFR) est réellement bénéfique pour le tissu axonal, et que leur diminution fait partie de la physiopathologie du glaucome. Nous pouvons spéculer que la déformation pulsatile contrecarre d'une certaine manière les effets simultanés de la PIO pulsatile , ce qui pourrait être un obstacle à l'écoulement axoplasmique.

Tous ces résultats soutiennent la croyance que la déformation rétinienne a le potentiel d'être utilisé comme un nouveau descripteur biomécanique de l'œil. D'autres études seront nécessaires pour démontrer le rôle des déformations pulsatiles de la macula et du nerf optique dans la pathogenèse du glaucome et si ces paramètres pourraient être utiles pour un diagnostic précoce.